

12-2018

Interfacial Tailoring of Lithium-ion Batteries by Atomic/Molecular Layer Deposition

Qian Sun

University of Arkansas, Fayetteville

Follow this and additional works at: <https://scholarworks.uark.edu/etd>

 Part of the [Electro-Mechanical Systems Commons](#), and the [Energy Systems Commons](#)

Recommended Citation

Sun, Qian, "Interfacial Tailoring of Lithium-ion Batteries by Atomic/Molecular Layer Deposition" (2018). *Theses and Dissertations*. 3040.

<https://scholarworks.uark.edu/etd/3040>

This Thesis is brought to you for free and open access by ScholarWorks@UARK. It has been accepted for inclusion in Theses and Dissertations by an authorized administrator of ScholarWorks@UARK. For more information, please contact scholar@uark.edu, ccmiddle@uark.edu.

Interfacial Tailoring of Lithium-ion Batteries by Atomic/Molecular Layer Deposition

A thesis submitted in partial fulfillment
of the requirements for the degree of
Master of Science in Mechanical Engineering

by

Qian Sun
Shaanxi University of Science and Technology
Bachelor of Engineering in Applied Chemistry, 2013
Northwest University
Master of Engineering in Chemical Engineering, 2016

December 2018
University of Arkansas

This thesis is approved for recommendation to the Graduate Council.

Xiangbo Meng, Ph.D
Thesis Director

Min Zou, Ph.D
Committee Member

Steve Tung, Ph.D
Committee Member

ABSTRACT

Lithium-ion batteries (LIBs) are promising energy storage devices, which play significant roles in addressing problems related to fossil fuels depletion and environmental pollution. Since the 1990s, LIBs have attracted great attention for many applications. Nowadays, LIBs are dominating portable electronics, having several advantages over their forerunners, such as high voltage (3.3~4.2 V) [1,2], low self-discharge (< 5~10 %/month) [3,4], wide operation temperature (-20~60 °C) [5,6], and fast charge/discharge rate [7,8]. However, LIBs deliver an energy density of 100-220 Wh/kg in practice to date, which is far from their theoretical ones, thus hindering their further applications in electric vehicles. Additionally, LIBs have been plagued by other problems, such as intolerance to overcharge/overdischarge, low heat resistance, lithium dendrites growth, large volume change of the silicon anode, large polarization and even safety problems.

Atomic layer deposition (ALD) and molecular layer deposition (MLD) are two important techniques, both proceeding in self-limiting gas-solid reactions and exhibiting excellent capabilities for ultra-thin films, conformal coatings, and controllable growth. They can be employed to address the problems of LIBs mentioned above by surface coatings, electrode designs, and solid-state electrolyte preparations. In this thesis, ALD is utilized to modify the interface between the electrolyte and Si anode in LIBs and to improve the performance of LIBs. ZnO coating deposited by ALD using precursors of diethylzinc (DEZ) and H₂O was found to be effective in accommodating the volume expansion of Si during charging-discharging process and preventing the direct Si-electrolyte contact, thus improving the performance of Li/Si-G battery. Additionally, effects of ALD coatings (Al₂O₃ and ZnO) on stabilizing lithium metal are investigated.

In chapter 1, the background of LIBs is introduced, as well as ALD and MLD. Chapter 2 investigates the growth properties of different coatings (Al_2O_3 , ZnO, TiO_2 , AlGL and ZnGL) using quartz crystal microbalance (QCM) method. Chapter 3 reports the modification of Si-electrolyte interface via ALD coatings and the performance of Li/Si-G (silicon-graphite) batteries. Chapter 4 investigates the stabilization of lithium metal using ALD coatings. Conclusions are shown in chapter 5. Future work and promising developments are given in chapter 6.

ACKNOWLEDGEMENTS

It is a great honor for me to express my deepest and honest appreciation to my thesis advisor, Dr. Xiangbo Meng. He gave me many suggestions and guidance towards my experiments and thesis writing. Dr. Meng's group focuses on smartly controllable nanosynthesis using ALD and MLD, and development of next-generation, high-performance, advanced, battery technologies. I feel grateful to join his group and conduct my research. The experience during my Master studies (January 2017 - December 2018) will be extremely helpful for my future development.

Also, I want to thank the rest of my thesis committee, Dr. Min Zou and Dr. Steve Tung, for their support, encouragement and comments about my experimental skills and independent thinking ability.

Besides my thesis committee, I would like to thank Dr. Darin W. Nutter for his support and the professors who have taught my courses (Dr. Rick J. Couvillion, Dr. Ing Chang Jong, Dr. Jim Leylek, Dr. Ingrid Fritsch, and Dr Lance Edward Miller).

Additionally, I would like to thank my colleague, Mr. Jiyu Cai for his help and advice to my research. Discussion with him always inspired me to move forward in my experiments.

Finally, I want to thank my friends and family. They supported and encouraged me, especially my parents.

TABLE OF CONTENTS

1 INTRODUCTION	1
1.1 Lithium Ion Batteries (LIBs).....	1
1.2 Atomic Layer Deposition (ALD)	9
1.2.1 Introduction of ALD.....	9
1.2.2 Mechanism.....	10
1.3 Molecular Layer Deposition (MLD)	13
1.3.1 Introduction of MLD	13
1.3.2 Mechanism.....	15
1.4 Motivation and Objective.....	19
1.5 References	21
2 GROWTH PROPERTIES OF DIFFERENT COATINGS.....	45
2.1 Materials.....	45
2.2 ALD/MLD Deposition Parameters	45
2.3 ALD Coatings	47
2.3.1 Al ₂ O ₃ film growth.....	47
2.3.2 TiO ₂ film growth	51
2.3.3 ZnO film growth.....	53
2.4 MLD Coatings.....	57
2.4.1 AIGL film growth.....	57
2.4.2 ZnGL film growth	59

2.5 Summary	61
3 MODIFICATION OF SI-ELECTROLYTE INTERFACE	62
3.1 Introduction of Si Electrode	62
3.2 Experimental Materials and Equipment	64
3.2.1 Materials	64
3.2.2 Equipment	65
3.3 Deposition of ZnO on Si-G Electrode	66
3.4 Preparation of Li/Si-G batteries	66
3.5 Results Discussion	67
3.5.1 AFM picture	67
3.5.2 SEM and EDX pictures	68
3.5.3 XRD result	71
3.5.4 Electrochemical behavior of Si-G electrode	72
3.6 Summary	76
3.7 References	77
4 STABILIZATION OF LITHIUM METAL VIA ALD COATINGS	81
4.1 Introduction of Li Metal Anode	81
4.2 Materials	85
4.3 Deposition of Al ₂ O ₃ and ZnO	85
4.4 Preparation of Bare Li/Ni Foam (or Cu), Bare Li/ALD Coated Ni Foam (or ALD Coated Cu), and ALD Coated Li/Ni Foam (or Cu) Batteries	86

4.5 Results Discussion.....	88
4.5.1 SEM pictures	88
4.5.2 Electrochemical behavior	92
4.6 Summary	99
4.7 References	101
5 CONCLUSIONS.....	106
6 FUTURE WORK AND PROMISING DEVELOPMENTS	108
6.1 Future Work and Promising Developments	108
6.2 References	110

LIST OF FIGURES

1 INTRODUCTION

Figure 1. The components of a typical lithium-ion battery and the electrochemical processes in charging and discharging. The typical cathode and anode materials are LiCoO_2 and graphite respectively [71]. Reprinted (adapted) with permission from ref. [71]. Copyright (2009) Royal Society of Chemistry. 3

Figure 2. (a) A model ALD process for depositing Al_2O_3 using TMA and water as precursors: (1) the initial substrate covered by hydroxyl groups, (2) TMA molecules reacting with hydroxyl groups, leading to a new intermediate layer, (3) the substrate covered with a newly created intermediate layer, (4) H_2O molecules reacting with the intermediate layer, leading to new hydroxyl groups, and (5) the substrate again covered by hydroxyl groups [194]. Reprinted (adapted) with permission from ref. [194]. Copyright (2012) John Wiley and Sons; (b) Proposed mechanism for Lewis base catalysis of SiO_2 ALD during the SiCl_4 reaction and the H_2O reaction [223]. Reprinted (adapted) with permission from ref. [223]. Copyright (1997) The American Association for the Advancement of Science; (c) Schematic diagram of hydrogen radical-enhanced ALD using a metal reactant and hydrogen radicals [241]. Reprinted (adapted) with permission from ref. [241]. Copyright (2009) American Chemical Society. 13

Figure 3. (a) Schematic representation of MLD using self-limiting surface chemistry and an AB binary reaction sequence [294]. Reprinted (adapted) with permission from ref. [294]. Copyright (2009) American Chemical Society; (b) Illustration of surface chemistry for two-step alucone MLD using TMA and EG as reactants [270]. Reprinted (adapted) with permission from ref. [270]. Copyright (2008) American Chemical Society; (c)

Illustration of surface chemistry for PPTA MLD using ClCOC₆H₄COCl (TC) and NH₂C₆H₄NH₂ (PD) as reactants [294]. Reprinted (adapted) with permission from ref. [294]. Copyright (2009) American Chemical Society; (d) Illustration of surface chemistry for three-step alucone. MLD with TMA, EA, and MA as reactants [301]. Reprinted (adapted) with permission from ref. [301]. Copyright (2009) American Chemical Society; (e) Suggested growth sequence for the Zn–AP film over a thin seed layer of ZnO on a Si substrate. The surface was left covered with –NH₂ groups [302]. Reprinted (adapted) with permission from ref. [302]. Copyright (2003) Royal Society of Chemistry..... 18

2 GROWTH PROPERTIES OF DIFFERENT COATINGS

Figure 1. ALD/MLD system..... 47

Figure 2. (a) Mass gain of Al₂O₃ deposited at 50 °C using the recipe of (TMA-purge-H₂O-purge, 0.015-15-0.015-15 s); (b) Three consequential cycles of Al₂O₃ deposited at 50 °C using the recipe of (TMA-purge-H₂O-purge, 0.015-15-0.015-15 s); (c) Film thickness of Al₂O₃ deposited at 50 °C using the recipe of (TMA-purge-H₂O-purge, 0.015-15-0.015-15 s); (d) Mass gain of Al₂O₃ deposited at 75 °C using the recipe of (TMA-purge-H₂O-purge, 0.015-10-0.015-10 s); (e) Three consequential cycles of Al₂O₃ deposited at 75 °C using the recipe of (TMA-purge-H₂O-purge, 0.015-10-0.015-10 s); (f) Film thickness of Al₂O₃ deposited at 75 °C using the recipe of (TMA-purge-H₂O-purge, 0.015-10-0.015-10 s); (g) Mass gain of Al₂O₃ deposited at 100 °C using the recipe of (TMA-purge-H₂O-purge, 0.015-5-0.015-5 s); (h) Three consequential cycles of Al₂O₃ deposited at 100 °C using the recipe of (TMA-purge-H₂O-purge, 0.015-5-0.015-5 s); (i) Film thickness of Al₂O₃ deposited at 100 °C using the recipe of (TMA-purge-H₂O-purge, 0.015-5-0.015-5

s); (j) Mass gain of Al₂O₃ deposited at 150 °C using the recipe of (TMA-purge-H₂O-purge, 0.015-5-0.015-5 s); (k) Three consequential cycles of Al₂O₃ deposited at 150 °C using the recipe of (TMA-purge-H₂O-purge, 0.015-5-0.015-5 s); (l) Film thickness of Al₂O₃ deposited at 150 °C using the recipe of (TMA-purge-H₂O-purge, 0.015-5-0.015-5 s); (m) Mass gain of Al₂O₃ deposited at 150 °C using the recipe of (TMA-purge-H₂O-purge, 1-5-1-5 s); (n) Three consequential cycles of Al₂O₃ deposited at 150 °C using the recipe of (TMA-purge-H₂O-purge, 1-5-1-5 s); (o) Film thickness of Al₂O₃ deposited at 150 °C using the recipe of (TMA-purge-H₂O-purge, 1-5-1-5 s). 49

Figure 3. SEM pictures of (a) bare NGS and ALD-Al₂O₃ deposited on N-doped single layer graphene (NGS) at 100 °C using (b) 1x, (c) 3x, and (d) 5x ALD cycles. (e) The recipe of 1x ALD-Al₂O₃ on NGS is as the following: TMA dosing--ten times of (pulse 0.2s-stop valve closed-wait 2s-stop valve open-wait 2s) and H₂O dosing--ten times of (pulse 0.2s-stop valve closed-wait 2s-stop valve open-wait 2s). 51

Figure 4. (a) Mass gain of TiO₂ deposited at 150 °C using the recipe of (TTIP-purge-H₂O-purge, 1-5-1-5 s); (b) Three consequential cycles of TiO₂ deposited at 150 °C using the recipe of (TTIP-purge-H₂O-purge, 1-5-1-5 s); (c) Film thickness of TiO₂ deposited at 150 °C using the recipe of (TTIP-purge-H₂O-purge, 1-5-1-5 s). 52

Figure 5. SEM pictures of (a) bare NGS and ALD-TiO₂ deposited on N-doped single layer graphene (NGS) at 100 °C using (b) 3x, (c) 15x, (d) 30x, and (e) 60x ALD cycles. (f) The recipe of 3x ALD-TiO₂ on NGS is as the following: 1x cycle is composed of TTIP dosing--ten times of (pulse 0.2s-stop valve closed-wait 2s-stop valve open-wait 2s) and H₂O dosing--ten times of (pulse 0.2s-stop valve closed-wait 2s-stop valve open-wait 2s), repeating the 1x cycles three times we get the recipe of 3x ALD-TiO₂ on NGS..... 53

Figure 6. (a) Mass gain of ZnO deposited at 150 °C using the recipe of (DEZ-purge-H₂O-purge, 1-5-1-5 s); (b) Three consequential cycles of ZnO deposited at 150 °C using the recipe of (DEZ-purge-H₂O-purge, 1-5-1-5 s); (c) Film thickness of ZnO deposited at 150 °C using the recipe of (DEZ-purge-H₂O-purge, 1-5-1-5 s). 54

Figure 7. SEM pictures of (a) bare NGS and ALD-ZnO deposited on N-doped single layer graphene (NGS) at 100 °C using (b) 1x, (c) 5x, (d) 10x, and (e) 20x ALD cycles. (f) The recipe of 1x ALD-ZnO on NGS is as the following: DEZ dosing--ten times of (pulse 0.2s-stop valve closed-wait 2s-stop valve open-wait 2s) and H₂O dosing--ten times of (pulse 0.2s-stop valve closed-wait 2s-stop valve open-wait 2s)..... 55

Figure 8. SEM pictures of ZnO deposited on N-doped single layer graphene (NGS) at 250, 200, 150, 100 and 80 °C using 100, 200, 300, 400 ALD cycles. The recipe is (DEZ-purge-H₂O-purge, 0.015-5-0.015-5 s), the growth rate is 0.7-2.5 Å/cycle. (Samples were prepared by Jiyu Cai. SEM pictures were taken by him and me.) 57

Figure 9. (a) Mass gain of AlGL deposited at 50 °C using the recipe of (TMA-purge-GL-purge, 0.015-20-2-60 s); (b) Three consequential cycles of AlGl deposited at 50 °C using the recipe of (TMA-purge-GL-purge, 0.015-20-2-60 s); (c) Mass gain of AlGL deposited at 75 °C using the recipe of (TMA-purge-GL-purge, 0.015-15-2-40 s) and (TMA-purge-GL-purge, 0.015-60-2-60 s); (d) Three consequential cycles of AlGl deposited at 75 °C using the recipe of (TMA-purge-GL-purge, 0.015-15-2-40 s) and (TMA-purge-GL-purge, 0.015-60-2-60 s). 58

Figure 10. (a) Mass gain of ZnGL deposited at 50 °C using the recipe of (DEZ-purge-GL-purge, 0.015-20-2-60 s); (b) Three consequential cycles of ZnGL deposited at 50 °C using the recipe of (DEZ-purge-GL-purge, 0.015-20-2-60 s); (c) Mass gain of ZnGL deposited at

75 °C using the recipe of (DEZ-purge-GL-purge, 0.015-15-2-40 s); (d) Three consequential cycles of ZnGL deposited at 75 °C using the recipe of (DEZ-purge-GL-purge, 0.015-15-2-40 s). 59

Figure 11. SEM pictures of (a) (b) bare NGS and (c) (d) 5x ZnGL coated NGS, (e) (f) 10x ZnGL coated NGS, and (g) (h) 15x ZnGL coated NGS. ZnGL was deposited at 50 °C using a recipe of (DEZ-purge-GL-purge, 0.03-20-4-60s). 60

Figure 12. AFM of ZnGL deposited on Si wafer at 150 °C using 150 cycles of (DEZ-purge-GL-purge, 1 s-60 s-1 s-60 s). 61

3 MODIFICATION OF SI-ELECTROLYTE INTERFACE

Figure 1. Failure mechanisms of a Si anode: (a) material pulverization and volume change of the Si electrodes, (b) morphology change of Si electrodes, and (c) SEI formation [1]. Reprinted (adapted) with permission from ref. [1]. Copyright (2015) John Wiley and Sons. 64

Figure 2. An Integrated System Combining Atomic/Molecular Layer Deposition with Glove Box; (b) (c) Battery Cycler 1; (d) Battery Cycler 2; (e) Coin Cell Crimper; (f) SP-200 BioLogic Science Instrument; (g) FEI Nova Nanolab 200 Dual-Beam Workstation.. 65

Figure 3. (a) Schematic illustration of Li/Si-G cell; (b) CR2032 coin cell; (c) Li metal; (d) Separator (polypropylene, polyethylene materials and additives). 67

Figure 4. AFM picture of ALD-ZnO deposited on Si wafer at 150 °C using 150 ALD cycles of (DEZ-purge-H₂O-purge, 0.015-5-0.015-5 s). 68

Figure 5. SEM pictures of bare Si-G electrode with magnifications of (a) (x200000), (b) (x99974), and (c) (x50000) before battery cycling; EDX results of (d) C, (e) Si, and (f) O distribution for (c). 69

Figure 6. SEM pictures of 6 nm ALD-ZnO (deposited at 150 °C) coated Si-G electrode with magnifications of (a) (x200000), (b) (x99977), and (c) (x50000) before battery cycling; EDX results of (d) C, (e) Si, (f) O, and (g) Zn distribution for (c). 69

Figure 7. EDX mapping results of (a) bare Si-G, (b) 2nm ZnO coated Si-G, (c) 4nm ZnO coated Si-G, (d) 6nm ZnO coated Si-G, (e) 8nm ZnO coated Si-G, and (f) 10nm ZnO coated Si-G before battery cycling, which correspond to their SEM pictures with magnification of (x50000)..... 70

Figure 8. SEM pictures of (a) (e) bare Si-G electrode and (b) (f) 6 nm, (c) (g) 8 nm, (d) (h) 10 nm ZnO (deposited at 150 °C) coated Si-G electrodes before and after 100 discharge-charge cycles. Recipe of ALD-ZnO is (DEZ-purge-H₂O-purge, 0.015-5-0.015-5 s), the growth rate is 1.0 Å/cycle. 71

Figure 9. XRD of Si-G electrode and 6 nm ALD-ZnO (deposited at 150 °C) coated Si-G anode. 71

Figure 10. Discharge capacity of bare Li/Si-G and Li/ZnO coated Si-G batteries with (a) 10 μL electrolyte and (d) saturated electrolyte; Capacity retention of bare Li/Si-G and Li/ZnO coated Si-G batteries with (b) 10 μL electrolyte and (e) saturated electrolyte; Voltage-capacity profile for first two cycles of (c) bare Li/Si-G and Li/6 nm ZnO coated Si-G batteries with 10 μL electrolyte and (f) that of Li/6 nm ZnO coated Si-G batteries with saturated electrolyte..... 73

Figure 11. EIS results of (a) bare Li/Si-G and Li/ZnO coated Si-G battery using 10 μL electrolyte (G2/FEC, 9:1, wt:wt) after 100 charge-discharge cycles; (b) bare Li/Si-G battery using 20 μL electrolyte (G2/FEC, 9:1, wt:wt) after 8, 15 and 20 charge-discharge cycles; (c) Li/6 nm ZnO coated Si-G battery using 20 μL electrolyte (G2/FEC, 9:1, wt:wt) after

11, 21 and 27 charge-discharge cycles; (d) Li/6 nm ZnO coated Si-G battery using saturated electrolyte after 0, 7, 14, 21 and 28 charge-discharge cycles. 75

4 STABILIZATION OF LITHIUM METAL VIA ALD COATINGS

Figure 1. Schematic representations of (a) Li-ion [58]. Reprinted (adapted) with permission from ref. [58]. Copyright (2014) American Chemical Society. (b) Li-S [10]. Reprinted (adapted) with permission from ref. 13. Copyright (2015) American Chemical Society. (c) Li-O₂ cells [15]. Reprinted (adapted) with permission from ref. 18. Copyright (2012) American Chemical Society. 81

Figure 2. Scheme of dilemma for Li metal anode in rechargeable batteries [21]. Reprinted (adapted) with permission from ref. 68. Copyright (2017) American Chemical Society. 83

Figure 3. (a) Schematic illustration of bare Li/Cu or bare Li/Ni foam cell; (b) Cu; (c) Ni foam; (d) CR2032 coin cell; (e) Separator; (f) Li metal. 87

Figure 4. SEM pictures of (a) (b) bare Li, (c) (d) Li electrode in Li/Cu cell after Li deposition at 0.5 mA/cm² for 2000 s, (e) (f) Li electrode in Li/Ni foam cell after Li deposition at 0.5 mA/cm² for 2000 s, (g) (h) Li positive electrode in Li/Li cell after Li deposition at 0.5 mA/cm² for 2000 s, (i) (j) Li negative electrode in Li/Li cell after Li deposition at 0.5 mA/cm² for 2000 s, (k) (l) Li electrode in bare Si-G/Li cell after 100 discharge-charge cycles (first 3 cycles at 1/20 C, last 97 cycles at 1/3 C, 1C = 808 mA/g)..... 90

Figure 5. (a) (b) bare Cu, (c) (d) Cu in Li/Cu cell after Li deposition at 0.5 mA/cm² for 2000 s, (e) (f) Cu in Li/Cu cell after Li deposition at 1 mA/cm² for 4000 s, (g) (h) bare Ni foam, (i) (j) Ni foam in Li/Ni foam cell after Li deposition at 0.5 mA/cm² for 2000 s, (k) (l) Ni foam in Li/Ni foam cell after Li deposition at 1 mA/cm² for 4000 s. 91

Figure 6. (a) Coulombic efficiency of bare Li/Cu, bare Li/Ni foam, Li/Cu + 10 nm Al₂O₃, Li/Ni foam + 10 nm Al₂O₃ (30 μL 1M LITFSI in DOL/DME, 1:1, V:V); (b) Coulombic efficiency of bare Li/Cu, bare Li/Ni foam, Li/Cu + 10 nm Al₂O₃, Li/Ni foam + 10 nm Al₂O₃ (30 μL 4M LITFSI in DME); (c) Coulombic efficiency of bare Li/Cu (30 μL 1M LITFSI in DOL/DME, 1:1, v:v), and bare Li/Cu (30 μL 4M LITFSI in DME); (d) Coulombic efficiency of Li/Cu + 10 nm Al₂O₃ (30 μL 1M LITFSI in DOL/DME, 1:1, v:v), and Li/Cu + 10 nm Al₂O₃ (30 μL 4M LITFSI in DME); (e) Coulombic efficiency of bare Li/Ni foam (30 μL 1M LITFSI in DOL/DME, 1:1, v:v), and bare Li/Ni foam (30 μL 4M LITFSI in DME); (f) Coulombic efficiency of Li/Ni foam + 10 nm Al₂O₃ (30 μL 1M LITFSI in DOL/DME, 1:1, v:v), and Li/Ni foam + 10 nm Al₂O₃ (30 μL 4M LITFSI in DME); (g) Coulombic efficiency of bare Li/Ni foam, xnm Al₂O₃ coated Li/Ni foam (x=2, 4, 6, 8, 10nm) (30 μL 1M LITFSI in DOL/DME, 1:1, v:v); (h) Coulombic efficiency of bare Li/Cu or Ni foam, x nm Al₂O₃ coated Li/Cu or Ni foam (x=2, 4, 6, 8, 10nm) (30 μL 1M LITFSI in DOL/DME, 1:1, v:v); (i) Coulombic efficiency of bare Li/Ni foam, bare Li/Cu, 4nm Al₂O₃ coated Li/Ni foam, 4nm Al₂O₃ coated Li/10nm Al₂O₃ coated Li Ni foam, 4nm Al₂O₃ coated Li/10 nm ZnO coated Li Ni foam (30 μL 1M LITFSI in DOL/DME, 1:1, v:v). Above batteries were tested with Li deposition at 0.5 mA/cm² for 2000 s and Li stripping up to 1V.. 94

Figure 7. Voltage profiles of Li/Cu, Li/Cu +10 nm Al₂O₃, Li/Ni foam, Li/Ni foam +10 nm Al₂O₃, Li/Ni foam batteries with (a) 1M LITFSI and (b) 4M LITFSI electrolyte; (c) ALD Al₂O₃ coated Li/Ni foam and bare Li/Ni foam; (d) ALD Al₂O₃ coated Li/Cu and bare Li/Cu. All batteries were tested with Li deposition at 0.5 mA/cm² for 2000 s and Li stripping up to 1 V. 96

Figure 8. EIS results of (a) Li/Li symmetric cell before and after 20 cycles; (b) Li/Cu and 4 nm Al_2O_3 coated Li/Cu after 20 cycles; (c) Li/Ni foam and 4 nm Al_2O_3 coated Li/Ni foam after 20 cycles. Electrolyte: 30 μL 1M LITFSI in DOL/DME (1:1, v:v). 99

LIST OF TABLES

1 INTRODUCTION

Table 1. Growth mechanism of different ALD processes	12
Table 2. Growth mechanism of different MLD processes.....	17

2 GROWTH PROPERTIES OF DIFFERENT COATINGS

Table 1 Summary of needed chemicals (1).....	45
Table 2. Deposition parameters of different coatings.....	46
Table 3. Summary of percentage of ALD- Al_2O_3 in total mass of Al_2O_3 +NGS	51
Table 4. Summary of percentage of ALD- TiO_2 in total mass of TiO_2 +NGS.....	53
Table 5. Summary of thickness of ALD-ZnO film.....	55
Table 6 Summary of percentage of ALD-ZnO in total mass of ZnO+NGS.....	56

3 MODIFICATION OF SI-ELECTROLYTE INTERFACE

Table 1. Summary of assembled batteries (1).....	67
Table 2. Discharge capacities for first 3 cycles of batteries	73
Table 3. Simulated EIS results of bare Li/Si-G and Li/ZnO coated Si-G batteries using 10 μL electrolyte (G2/FEC, 9:1, wt:wt)	76

4 STABILIZATION OF LITHIUM METAL VIA ALD COATINGS

Table 1. Summary of needed chemicals (2).....	85
Table 2. Summary of assembled batteries (2).....	88
Table 3. Calculated nucleation overpotential of batteries.....	97
Table 4. Summary of overpotential of batteries for first Li deposition/stripping cycle	98

LIST OF PUBLISHED PAPERS

1. Q. Sun, X. Meng*. Inhibiting lithium dendrite growth for lithium batteries: Challenges and Strategies, Nova Sciences, 2018, ISBN: 978-1-53613-498-8.
2. Q. Sun, K. C. Lau, D. Geng, X. Meng*. Atomic and molecular layer deposition for superior lithium-sulfur batteries: strategies, performance, and mechanisms, Batteries & Supercaps, 2018, 1:41-68.
3. J. Cai, Q. Sun, and X. Meng*, Nanostructured materials by atomic and molecular layer deposition, AIMS Materials Science, 2018, 5(5): 957-999.

LIST OF UNPUBLISHED PAPERS

1. J. G. Steck, M. A. Mohajer, Q. Sun, X. Meng, and M. Zou*. Deformation-resistant Nano-textured surfaces fabricated using two-photon lithography and atomic layer deposition, Tribology International, 2018, submitted.

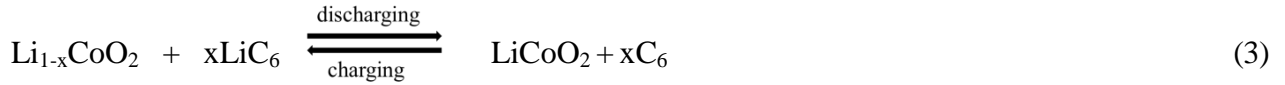
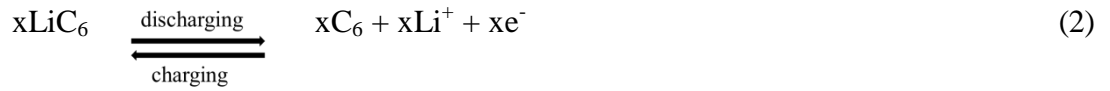
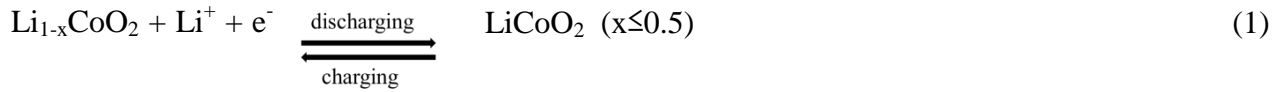
1 INTRODUCTION

1.1 Lithium Ion Batteries (LIBs)

Modern societies are experiencing several issues with the escalating energy demands, including limited fossil fuels [9-13], environmental problems [14-18], and global warming [19-23]. In this regard, renewable clean energies [24-28] such as wind and solar powers are highly regarded for addressing these challenges. However, they operate intermittently for generating electricity, due to their dependence to daily weather conditions. To achieve continuous energy supply, many kinds of electrical energy storage (EES) devices have been studied and practiced, such as primary batteries (Daniell cell [29,30], Leclanché cell [31-33], and Alkaline batteries [34-37]), specialty batteries (for military/medical [38,39]), and rechargeable batteries or secondary batteries (Lead-acid batteries [40-43], Ni-Cd batteries [44-46], Ni-MH batteries [47-50], LIBs [38,51-55]). Among them, LIBs are very promising and represent the highest level of rechargeable batteries to date [56].

In 1991, LIBs were firstly commercialized by Sony Corporation [57]. Since then, LIBs have been widely applied in many fields, including portable electronics (smartphones, laptops, cameras, flashlights and electronic cigarettes), electric vehicles (hybrid vehicles, electric cars, and electric bicycles), smart grids, and autonomous devices (M/NEMS, sensors, actuators). For lithium ion batteries, there are mainly three kinds of anode materials, including conversion anode (metal oxides, metal sulfides, metal nitrides, metal phosphides and metal fluorides) [58-62], intercalation/de-intercalation anode (graphite, TiO_2 , $\text{Li}_4\text{Ti}_5\text{O}_{12}$) [63-65] and alloy/de-alloy anode (Si, Ge, Sn, SiO_2 , SnO_2) [66-68]. The metal oxide cathode materials of LIBs such as LiCoO_2 , LiFePO_4 , and LiMn_2O_4 [69] are commonly used. Besides the electrode materials, an electrically insulating polymeric separator and a non-aqueous electrolyte are needed to assemble a LIB. A

typical electrolyte [70] is prepared by dissolving a lithium salt (such as lithium bis(trifluoromethanesulfonyl)imide (LiTFSI), lithium hexafluorophosphate (LiPF₆), and LiClO₄) in a carbonate-based solvent (ethylene carbonate (EC), diethyl carbonate (DEC), propylene carbonate (PC), dimethyl carbonate (DMC)) or an ether-based solvent (dimethoxyethane (DME)). The electrolyte provides an ionically conductive medium for Li⁺ to move from anode to the cathode during discharging and back during charging. And the electrode materials undergo electrochemical reactions in the operation process of a LIB. For example, in a LiCoO₂/LiC₆ battery as shown in Figure 1 [71-74], the cathode half-reaction, anode half reaction and full reaction are given in Equations (1), (2), (3) as following:



However, the full reaction has limits. Once over-discharged, the battery will produce Li₂O irreversibly as shown in the following Equation (4) [75]. Over-discharging to 5.2 V results in the production of CoO₂ as given in Equation (5), which is confirmed by x-ray diffraction [74].



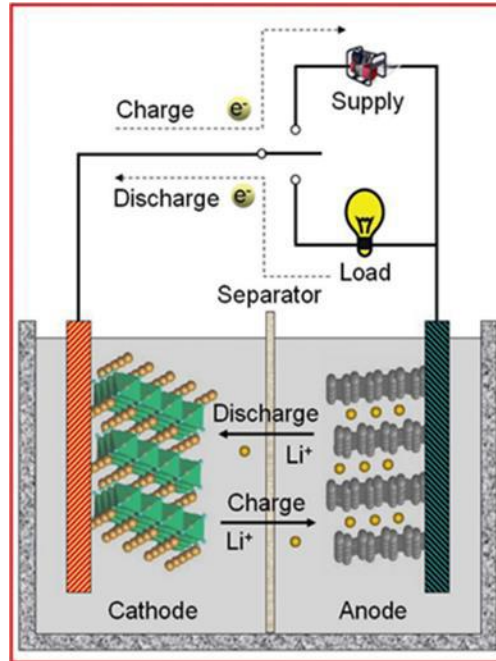


Figure 1. The components of a typical lithium-ion battery and the electrochemical processes in charging and discharging. The typical cathode and anode materials are LiCoO_2 and graphite respectively [71]. Reprinted (adapted) with permission from ref. [71]. Copyright (2009) Royal Society of Chemistry.

Besides the insertion reaction mechanism of anodes as discussed above, two other mechanisms (Li-alloy reaction mechanism and conversion reaction mechanism) can be described as Equations (6) and (7), respectively.

Li-alloy mechanism:



Conversion mechanism:



The performance of LIBs is affected by the applied electrodes, electrolyte, and the electrolyte-anode or electrolyte-cathode interfaces. LIBs can exhibit a volumetric energy density of 250-620 Wh/L ($900\text{-}2230 \text{ J/cm}^3$) [76] and an energy density of 100-220 Wh/kg [55,77], far from their theoretical ones.

LIBs are plagued by several challenges as follows:

(I) Formation of unstable solid electrolyte interphase (SEI) on anode [52] will increase impedance, consume electrolyte and consume lithium. For example, during lithiation, SEI at the Si anode-liquid electrolyte can be broken, which leads to the re-exposure of fresh Si to electrolyte and continuous growth of SEI [78]. While SEI on cathode ($\text{LiNi}_{0.8}\text{Co}_{0.2}\text{O}_2$) [79] forms because of oxidation of carbonate electrolyte [80,81], leading to increases in resistance.

(II) The Si/G anode used in LIBs exhibit huge volume expansion (graphite 100%, silicon 400%) during charging-discharging of batteries. For Si anode, the volume change during lithiation/delithiation will lead to electrode peel-off and failure [78]; The stresses induced by the volume change result in Si cracking and pulverization, thereby losing electrical contact and leading to capacity fading eventually [78].

(III) Sn-based anodes exhibit poor cycling performance because of pulverization [82]. Besides, conversion anodes suffer from the issues of large volume change and low electrical conductivity [62]. This can be solved by using carbon materials based materials such as graphene.

(IV) The cell capacity of LIBs is restricted by the low capacity of cathodes materials. LiMn_2O_4 , LiFePO_4 and LiCoO_2 exhibit low specific capacities of 148 (120), 170 (160) and 272 (140) mAh/g. Future cathodes with high capacity should avoid expensive and toxic elements such as Co and Ni, in this case, Mn- and Fe- based cathodes should be considered [82].

(V) LIBs are easy to exhibit safety issues because of heat and gas generation. Heat is generated when Li^+ transfer from cathode to anode during charging and back during discharging. For

example, cobalt oxide used in LIBs is easy to appear “thermal runaway”. Once heated up, cobalt oxide will self-heat and produce CO₂ and O₂ [83,84], resulting in fire and explosion.

(VI) LIBs cannot stand over-discharge or over-charge. When over-discharged (< 3.0 V), the excessive embedded Li⁺ will be fixed in the crystal lattice and cannot be released again, resulting in shortened life. Deep discharge is more likely to damage the battery. When overcharged, too many Li⁺ are embedded in the electrode without being replenished in time, which can lead to lattice collapse and irreversibly reduce the power storage.

Additionally, other problems such as cost, durability and uniformity restrict further application of LIBs in electric vehicles. Besides, temperature and voltage windows of electrode materials pose limitations on LIBs. For example, most automotive LIBs (graphite/LiMn₂O₄, C/LiCo_xNi_yMn_zO₂, C/LiFePO₄, C/LiNi_{0.8}Co_{0.15}Al_{0.05}O₂) exhibit fast-charging within 0-45 °C and discharging at -20-55 °C. Li₄Ti₅O₁₂ anode allows a low charge temperature of -30 °C. Normally, most LIBs display an operating voltage of 1.5-4.2 V [85].

To address these challenges and achieve high-performance LIBs, several strategies play significant roles.

(I) Developing nanostructured electrodes for LIBs [86,87]. Firstly, nanostructured materials exhibit large surface areas and many active sites, providing large spaces and active sites for Li intercalation/deintercalation reactions, which can be employed to enhance the anode capacity and energy densities of the batteries. With stable SEI layer and large contact areas between electrode and electrolyte, nanostructured electrodes provide effective Li⁺ and e⁻ pathways, thereby leading to increased electrochemical charging/discharging rates and power densities. With flexible structures, nanomaterials can accommodate huge volume expansion/contraction during charge-

discharging process, improving cycling performance of batteries. Moreover, nanostructured anodes involving conductive matrices (carbon components) are effective in lowering the interface resistances, thereby obtaining higher specific capacities at high charge/discharge rates [88-91]. For example, nanocarbons (carbon nanotube (CNT) [92-94], carbon nanofibers (CNFs) [95-97], graphene [98-100], porous carbon [101-103]), atomic layer deposition (ALD)-SnO₂ coated aluminum oxide (AAO) [104], ALD-TiO₂ on GNS [105], TiO₂ nanoribbons by ALD [106], ALD TiO₂-(Ni-TMV) core-shell structure [107] have been explored to improve the LIBs' performance in terms of Coulombic efficiency, cycling stability and rate capability. Nanostructured cathodes [108] including LiNi_{0.5}Mn_{1.5}O₄ [109,110], V₂O₅ [111,112], and MnO₂ [113,114] have been synthesized to develop LIBs with high energy density and electrochemical performance.

(II) Applying solid-state electrolytes. Liquid electrolytes used in rechargeable LIBs suffer from issues of leakage, poor electrochemical stability, and flammability. Solid-state electrolytes are found to be effective in avoiding these problems [115-119]. Because solid-state electrolytes are highly Li⁺ conductive at ambient temperature, mechanically and electrochemically stable, and exhibit low interfacial resistance and good adhesion to electrodes. Generally, there are two kinds of solid-state electrolytes for LIBs, inorganic ceramics [120] and organic polymers [120-122]. Ceramics are used for designing rigid batteries (thin-film devices) because of their high elastic moduli and can work at high temperature. Commonly used ceramics are sulfides (Li₂S-P₂S₅ glass [123], Li₃PO₄-Li₂S-SiS₂ [124], Li₂S-Ga₂S₃-GeS₂ [125], Li₂S-Sb₂S₃-GeS₂ [126], Li₂S-GeS₂-P₂S₅ [127], Li_{2.2}Zn_{0.1}Zr_{1.9}S₃ [128]), oxides (LiTaO₃ [129], Li₅La₃Ta₂O₁₂ [130], Li_{5+x} Ba_xLa_{3-x}Ta₂O₁₂ [131], Li₆La₂CaTa₂O₁₂ [132], Li₆La₂ANb₂O₁₂ (A=Ca, Sr) [133], Li₂Nd₃TeSbO₁₂ [134], Li₃BO_{2.5}N_{0.5} [135], Li_{2-2x}Mg_{2x}TiO_{3+x} [136], Li_{2x}Zn_{2-3x}Ti_{1+x}O₄ [137]), and phosphates

($\text{Li}_{1+x}\text{Al}_x\text{Ge}_{2-x}(\text{PO}_4)_3$ (LAGP) [138], $\text{Li}_{1+x}\text{Ti}_{2-x}\text{Al}_x(\text{PO}_4)_3$ (LTAP) [139], $\text{Li}_x\text{AlZr}(\text{PO}_4)_3$ [140], $\text{Li}_3\text{Fe}_2(\text{PO}_4)_3$ [141], LiPON [142]). Different from ceramics, polymer electrolytes usually exhibit low elastic moduli and can be used for developing flexible batteries. Some polymeric electrolytes are polymers (poly(ethylene oxide) (PEO) [143,144], poly(ethylene oxide) methyl ether methacrylate (PEOMA) [145], poly(acetyl-oligo(ethylene oxide) acrylate) (PAEOA) [120], polyester diacrylate(PEDA)-PEG copolymers [146], poly(ethylene glycol) dimethacrylate (PDE) [147], poly(ethylene glycol) methacrylate (PME) [147], poly(ethylene glycol) methyl ether methacrylate (PEGMA) [148]), polymer gel electrolytes (poly(vinylidene fluoride)-hexafluoropropylene (PVdF-HFP) [149], poly(acrylonitrile)-poly(methylmethacrylate (PAN-PMMA) [150]).

(III) Functionalizing separators of LIBs. Separators physically separate cathode and anodes while enabling free Li^+ flow [151]. Separators should have chemical and electrochemical stability against electrolyte and electrode, strong mechanical ability to strive against large tension from battery assemble, and appropriate porosity to absorb liquid electrolyte for the ionic conductivity [152]. Normally, microporous polymer membrane (polypropylene(PP) [153,154], polyethylene (PE) [155,156], polystyrene (PS)-PP [157]), non-woven mats (celluloses [158], polyester non-woven [159], poly(vinyl acetate) (PVAc) coated PVDF [160]) and inorganic composite membranes ($\text{TiO}_2/\text{PVDF-HFP}$ [161], $\text{Al}_2\text{O}_3/\text{PVDF}$ [162], Boehmite sol/polyvinyl alcohol/poly(ethylene terephthalate) (PET) composite separator [163]) are used as separators in LIBs. Modifying separators is effective in improving battery performance. Surface modification of polyolefin separators (ethylene carbonate (EC), propylene carbonate (PC) and γ -butyrolactone (GBL)) can be performed using wetting agents (surfactants) [164] to improve wettability or using hydrophilic functional groups (hydroxyl, carbonyl, carboxyl, amino, imino, sulfonyl)

[165,166] to increase electrolyte retention. Besides, coating polymer on separator surface is effective in improving the interfacial contact of separator and electrodes. This is also favorable to achieve even current distribution and suppress Li dendrites generation on negative electrode. For example, gellable acrylonitrile-methyl methacrylate copolymer was coated on both sides of PE separator. With the obtained separator (14 μm), lithium-ion polymer cell (mesocarbon microbead (MCMB)/LiCoO₂) exhibited good capacity retention and excellent rate performance [167]. Additionally, modifying separators using ALD attracts many interests. For example, ALD-Al₂O₃ (10 nm) [168] and TiO₂ [169] coatings on porous polypropylene (PP) separators could significantly improve thermal stability and safety of the batteries.

(IV) Improving SEI properties for LIBs. The anode surface should be covered entirely by SEI to prevent electrolytes from unwanted degradation that consumes Li⁺. Li⁺ loss from cathode and electrolyte salts affects the first-cycle irreversible capacity and power density of batteries, respectively [70,170]. Continuous SEI growth on anodes will result in increases in cell resistance and anode potential, which further induces increased cathode potential and affects negatively the stability of cathode crystal structure. Thus, building stable SEI layers on electrode surface is necessary. Optimized SEI layers should have high selectivity and permeability of Li⁺, good electrolyte diffusion resistance, and neglected electrical conductivity [171]. Introduction of additives (vinyl carbonate (VC) [172], diphenyloctyl phosphate [173], acetyl caprolactam, 3-fluoro-1,3-propane sultone [174], prop-1-ene-1,3-sultone [175]) into electrolyte is favorable to form stable SEI. Moreover, surface coatings (ALD-Al₂O₃ [176-178], ALD-TiN [179], ALD-TiO₂ [180]) over anode active materials (Si anode [178], graphene [177,180], Li₄Ti₅O₁₂ powder [179], LiCoO₂ powders [176]) are confirmed to protect anode effectively. Additionally, chemical modification for carbon surface (Li₂CO₃ pretreated graphite [181], n - butyl lithium treated

carbon black electrodes [182], HNO_3 and $(\text{NH}_4)_2\text{S}_2\text{O}_8$ oxidized graphite [183], aryl functional groups modified graphite [184,185]) is feasible in building stable SEI. Finally, high first charging rate (0.05 C-0.2 C) is normally beneficial for porous and highly resistive SEI layers [186,187].

1.2 Atomic Layer Deposition (ALD)

As a thin film technique, ALD can grow films on a substrate by alternatively exposing its surface to gas-phase precursors. Different from chemical vapor deposition (CVD), where the precursors are mixed in the chamber to react continuously to grow films, the precursors in ALD are introduced by a series of iterated sequential, non-overlapping self-saturating deposition cycles [188]. ALD can prepare uniform films without inferior discontinuities because of nucleation [189]. Therefore, ALD films are pinhole-free and stress-free. However, CVD and physical vapor deposition (PVD) initiate films by nucleation. This is followed by grain growth, finally influencing the film thickness [190,191] by CVD and PVD. Those films exhibit properties of pinholes and compressive stress. ALD exhibit great potential for preparing ultrathin films with precise control over film quality and thickness at atomic scale, based on a self-limiting growth mechanism [177,192-196]. More detailed explanation will be given in the following parts.

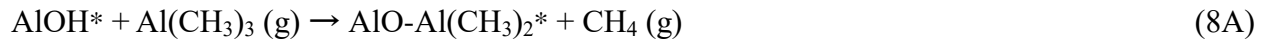
1.2.1 Introduction of ALD

ALD was developed independently by two groups in Finland (named atomic layer epitaxy (ALE), 1974) and Soviet Union (named molecular layering (ML), 1960s) [197]. In the 1970s, ALD was initiated by Suntola et al for developing thin-film electroluminescent displays (TFEL) [198,199]. The first successful practice was for depositing ZnS using elements Zn and S [198,200]. Now, ALD has been utilized for many more applications, including renewable clean energies (e.g., batteries, solar cells, supercapacitors, high permittivity memory capacitor

dielectrics water splitting) [194,196,201-204], surface engineering [205], catalysis [206], biomedical [207], and many others [208-210]. All these applications are attributed to ALD's abilities to prepare films on complex substrates with accurate control over film thickness and quality at the atomic level. Additionally, ALD has many other capabilities: (1) ALD can be employed to deposit various inorganic materials, including metal nitrides [211], metal fluorides [212,213], metal sulfides [214], elements [211,215,216], complex compounds [217-219] and metal oxides [220,221]; (2) The growth rate of ALD multilayer films is straightforward; (3) ALD exhibits low growth temperature (≤ 400 °C, even down to room temperature) [222-225], which is much lower than that of CVD (600-1000 °C); and (4) ALD can be used to tune the compositions of deposition films. Researchers have prepared stoichiometric deposition of metal oxides such as Al_2O_3 [226], Gd_2O_3 [227] and HfO_2 [228].

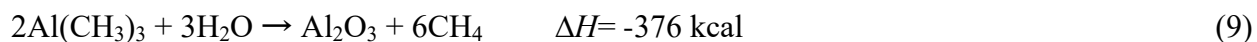
1.2.2 Mechanism

Typically, an ALD cycle of binary compounds consists of two half self-limiting gas phase reactions and two purge steps. Taking the deposition of Al_2O_3 (precursors: TMA + H_2O) for example, there are four repetitive steps [192-196,229]. Firstly, as shown in Figure 2(a2) [194] and Equation (8A) [230-233], introducing TMA to react with a substrate surface on which has reactive sites such as -OH (Figure 2(a1)). Secondly, performing a purging step to evacuate excessive TMA and the byproduct CH_4 (Figure 2(a2)(a3) generate the byproduct of CH_4). Then, introducing H_2O to react with reactive groups - CH_3 (Figure 2(a4) [194], Equation (8B) [230-233]). In this procedure, Al_2O_3 and new reactive sites -OH are produced (Figure 2(a5) [194]). Finally, conducting another purging step to remove excessive H_2O and the byproduct CH_4 .



Where “*” stands for the surface species. “g” demonstrates the gaseous phase of precursors or byproducts.

These two surface reactions are very self-limiting and efficient driven by the formation of Al-O bond. The overall reaction for ALD- Al_2O_3 is given by Equation (9).



This reaction has the highest reaction enthalpy of -376 kcal encountered for any ALD reaction [234].

Repeating these four steps can deposit Al_2O_3 in a layer by layer mode, Al_2O_3 growth exhibited a linear relationship with the number of ALD cycles. QCM indicated that the growth rate of ALD Al_2O_3 was 1.1-1.2 Å/cycle [235].

Besides the growth mechanism of model ALD Al_2O_3 , there are also many other literatures devoted to the growth mechanism of different ALD processes as given in Table 1 [223,236-247].

Table 1. Growth mechanism of different ALD processes

	Surface reactions	Overall reaction	References
Catalytic SiO ₂ (Figure 2(b))	SiOH* + SiCl ₄ → SiOSiCl ₃ * + HCl SiCl* + H ₂ O → SiOH* + HCl	SiCl ₄ + 2H ₂ O → SiO ₂ + 4HCl	[223,234,247]
¹ ALD W	WSiF ₂ H* + WF ₆ → WWF ₅ * + SiF ₃ H WF ₅ * + Si ₂ H ₆ → WSiF ₂ H* + SiF ₃ H + 2H ₂	WF ₆ + Si ₂ H ₆ → W + SiF ₃ H + 2H ₂	[234,245,246]
¹ ALD Ru	(A) RuO _x * + Ru(Cp) ₂ → RuRu(Cp) * + 5CO ₂ + 5/2H ₂ O (B) RuCp* + yO ₂ → RuO _x * + 5CO ₂ + 5/2H ₂ O	Ru(Cp) ₂ + 25/2O ₂ → Ru + 10CO ₂ + 5H ₂ O	[244]
² ALD Ti (Figure 2(c))	(A) Ta* + TaCl ₅ → TaTaCl ₅ * (B) TaCl ₅ * + 5H· → Ta* + 5HCl	TaCl ₅ + 5H· → Ta + 5HCl	[241-243]
² ALD Si	(A) Si* + SiH ₂ Cl ₂ → SiSiCl ₂ * + H ₂ (B) SiCl ₂ * + 2H → Si* + 2HCl	SiH ₂ Cl ₂ + 2H → Si + 2HCl + H ₂	[238-240]
³ ALD ZnO	(A) Zn(C ₂ H ₅) ₂ + *OH → *O-Zn(C ₂ H ₅) + C ₂ H ₆ (B) *O-Zn(C ₂ H ₅) + H ₂ O → *O-Zn(OH) + C ₂ H ₆	Zn(C ₂ H ₅) ₂ + H ₂ O → ZnO + 2C ₂ H ₆	[237]
³ ALD HfO ₂	(A) -OH* + (C ₂ H ₆ N) ₄ Hf(g) → *-O-Hf- (C ₂ H ₆ N) ₃ + CH ₃ NHCH ₃ (g) (B) *-O-Hf-(C ₂ H ₆ N) ₃ + 3H ₂ O(g) → *-O- Hf-(OH) ₃ + 3CH ₃ NHCH ₃ (g)	(C ₂ H ₆ N) ₄ Hf(g) + 3H ₂ O(g) → HfO ₂ + 4CH ₃ NHCH ₃ (g)	[248]
³ ALD TiO ₂	(A) *2(-OH) (s) + TiCl ₄ (g) → *(-O-) ₂ TiCl ₂ (s) + 2HCl (g) (B) *(-O-) ₂ TiCl ₂ (s) + 2H ₂ O → *(-O-) ₂ Ti(OH) ₂ (s) + 2HCl (g)	TiCl ₄ + 2H ₂ O → TiO ₂ + 4HCl	[236]

Note: ¹ Metal ALD; ² Hydrogen radical-enhanced or plasma ALD; ³ Thermal ALD.

We should know that ALD film growth is denoted by three parameters of substrate, temperature, and precursor. Wisely choosing these parameters is crucial to optimize the growth of deposited materials [241,249-253]. As a surface-controlled vapor-phase process, ALD outperforms CVD (semi-surface controlled gas-phase process) [254] and PVD (source controlled gas-phase process) [254] in terms of depositing films, displaying excellent uniformity, conformality, and precise thickness controllability at atomic scale.

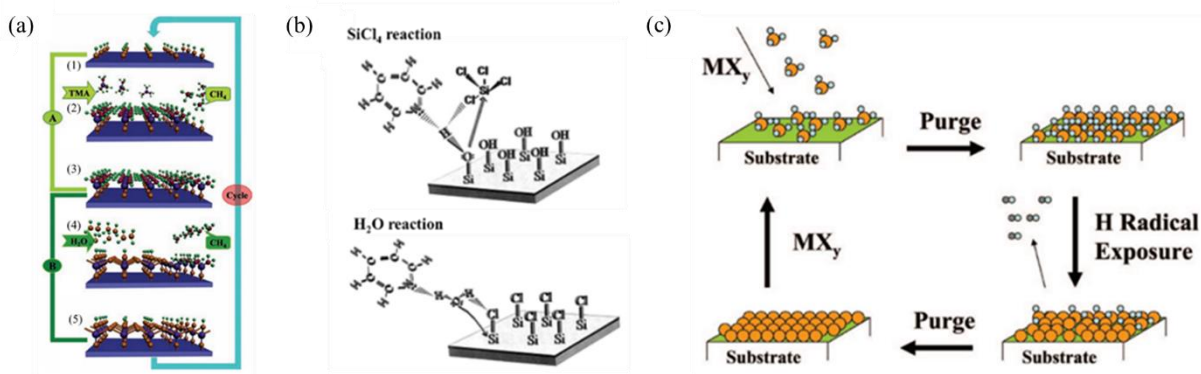


Figure 2. (a) A model ALD process for depositing Al₂O₃ using TMA and water as precursors: (1) the initial substrate covered by hydroxyl groups, (2) TMA molecules reacting with hydroxyl groups, leading to a new intermediate layer, (3) the substrate covered with a newly created intermediate layer, (4) H₂O molecules reacting with the intermediate layer, leading to new hydroxyl groups, and (5) the substrate again covered by hydroxyl groups [194]. Reprinted (adapted) with permission from ref. [194]. Copyright (2012) John Wiley and Sons; (b) Proposed mechanism for Lewis base catalysis of SiO₂ ALD during the SiCl₄ reaction and the H₂O reaction [223]. Reprinted (adapted) with permission from ref. [223]. Copyright (1997) The American Association for the Advancement of Science; (c) Schematic diagram of hydrogen radical-enhanced ALD using a metal reactant and hydrogen radicals [241]. Reprinted (adapted) with permission from ref. [241]. Copyright (2009) American Chemical Society.

1.3 Molecular Layer Deposition (MLD)

1.3.1 Introduction of MLD

As the sister technique of ALD, MLD was initiated in 1991 by Yoshimura et al for preparing organic or inorganic-organic hybrid materials [255,256]. To date, MLD has exhibited excellent

capabilities of producing polymer materials (polyimide-polyamides, polyamide, polythiourea, polyurethane, polyazomethine, polyethylene terephthalate, polyester, poly(3,4-ethylenedioxythiophene), polyurea) [257-268], hybrid materials including metalcones (hafnicones, alucones, titanicones, zincones, zircons, mangancones, vanadicones) [269-275], metal tetracyanoethylenes [276,277], and metal quinolones [278,279], metal-organic frameworks (MOFs) [280-282], and lithium terephthalates [283]. MLD can be widely applied in catalysis [284], microelectronics [285], batteries [286,287], organic magnets [285], surface engineering [288,289], luminescent devices [290], and many others [290,291]. MLD exhibits many advantages because of the organic part in films. Firstly, MLD films have high flexibility against straining that can be tuned by changing the length of carbon chain in the organic parts [275,292]. Secondly, MLD films exhibit less density than ALD metal oxides [293,294]. Thirdly, metalcone alloy materials by MLD have excellent mechanical properties (density, elastic modulus, hardness) that can be optimized by changing the contents of organic parts [295], good electrical conductivity and high dielectric constants [295-297]. Fourthly, heat treatment or chemical process for the metalcones can be employed to prepare highly porous metal oxides [298,299]. Besides these advantages, MLD also has some shortcomings. (1) Organic precursors used in MLD process are restricted by their low vapor pressure and limited thermal stability [300], thereby requiring a long pulsing time to realize saturated growth. (2) Most EG-based metalcones don't have satisfactory stabilities against water and oxygen [273,290]. (3) Gas-phase reactants could diffuse into the polymer attributed to the porosity of MLD films [294]. (4) Precursors employed in MLD process using a fluidized bed reactor are easy to agglomerate [300].

1.3.2 Mechanism

Analogous to ALD, MLD also belongs to a surface-controlled vapor-phase process. ALD is employed for growing inorganic films, while MLD exhibits capabilities of preparing purely organic or inorganic-organic hybrid materials. Similar to the ALD process, a MLD cycle of binary compounds is also composed of two half self-limiting gas phase reactions and two purge steps, as illustrated in Figure 3(a) [294]. A specific example of depositing alucone AIEG with TMA and ethylene glycol (EG, HOCH₂CH₂OH) as precursors is described in Equations (10A) and (10B) (Figure 3(b) [230,270]).



where “*” demonstrates the surface species. “g” stands for the gaseous phase of precursors or byproducts. Comparing with the atomic part of –O– in the ALD-Al₂O₃, the molecular fragment of –OCH₂CH₂O– in alucone is much larger, making a much faster growth of alucone AIEG than ALD Al₂O₃.

Besides the two-step AB MLD process, researchers also investigated the growth mechanism of three-step ABC MLD process and combined ALD-MLD process. Some MLD processes and their growth mechanisms are summarized in Table 2 [230,258,259,270,293,294,301].

Byunghoon et al [301] deposited inorganic-organic alucone polymer using precursors of TMA, ethanolamine (EA), and maleic anhydride (MA) (Figure 3(d)). The surface reactions in this process can be described as Equations (11A), (11B) and (11C).





Where, “S” indicates the substrate.

Anjali et al [302] employed a combined ALD-MLD method to prepare inorganic-organic hybrid films (-Zn-O-C₆H₄-NH-) by sequentially introducing DEZ and 4-aminophenol (AP) as precursors. Prior to the hybrid film deposition, inorganic ALD-ZnO (precursors: DEZ + H₂O) was deposited on Si(100) firstly as a seed layer to keep uniform and homogeneous film thickness. The reaction for the whole process was shown in Figure 3 (e).

Table 2. Growth mechanism of different MLD processes

	Surface reactions	References
¹ poly(p-phenylene terephthalamide) (PPTA) (Figure 3(c))	(A) $\text{SNH}_2^* + \text{ClCOC}_6\text{H}_4\text{COCl} \rightarrow \text{SNHCOC}_6\text{H}_4\text{COCl}^* + \text{HCl}$ (B) $\text{SNHCO}(\text{CH}_2)_4\text{COCl}^* + \text{H}_2\text{NC}_6\text{H}_4\text{NH}_2 \rightarrow \text{SNHCOC}_6\text{H}_4\text{CONH}(\text{CH}_2)_6\text{NH}_2^* + \text{HCl}$	[258]
¹ nylon 66	(A) $\text{SNH}_2^* + \text{ClCO}(\text{CH}_2)_4\text{COCl} \rightarrow \text{SNH-CO}(\text{CH}_2)_4\text{COCl}^* + \text{HCl}$ (B) $\text{SNHCO}(\text{CH}_2)_4\text{COCl}^* + \text{H}_2\text{N}(\text{CH}_2)_6\text{NH}_2 \rightarrow \text{SNHCO}(\text{CH}_2)_4\text{CO-NH}(\text{CH}_2)_6\text{NH}_2^* + \text{HCl}$	[259]
¹ general two-step AB cycles using homo-bifunctional precursors	(A) $\text{SR}'\text{Y}^* + \text{XRX} \rightarrow \text{SR}'\text{-RX}^* + \text{XY}$ (B) $\text{SRX}^* \rightarrow \text{YR}'\text{Y} \text{ f } \text{SR-R}'\text{Y}^* + \text{XY}$	[294]
alucone	(A) $\text{SOAl-OH}^* + \text{Al}(\text{CH}_3)_3 \rightarrow \text{SOAlO-Al}(\text{CH}_3)_2^* + \text{CH}_4$ (B) $\text{SOAlO-Al}(\text{CH}_3)_2^* + \text{HOC}_6\text{H}_4\text{OH} \rightarrow \text{SOAlOAl-OC}_6\text{H}_4\text{OH}^* + 2\text{CH}_4$	[230,293]
² general two-step interaction between metal alkyls and diols	(A) $\text{SR}'\text{OH}^* + \text{MR}_x \rightarrow \text{SR}'\text{O-MR}_{x-1}^* + \text{RH}$ (g) (B) $\text{SMR}^* + \text{HOR}'\text{OH} \rightarrow \text{SM-OR}'\text{OH}^* + \text{RH (g)}$	[230,270]
³ general two-step AB cycles using hetero-bifunctional precursors	(A) $\text{SR}'\text{Z}^* + \text{WRX} \rightarrow \text{SR}'\text{-RX}^* + \text{ZW}$ (B) $\text{SRX}^* + \text{YR}'\text{Z} \rightarrow \text{SR-R}'\text{Z}^* + \text{XY}$	[294]
¹ general three-step ABC cycles using hetero-bifunctional precursors	(A) $\text{SR}''\text{Z}^* + \text{TRV} \rightarrow \text{SR}''\text{-RV}^* + \text{ZT}$ (B) $\text{SRV}^* + \text{WR}'\text{X} \rightarrow \text{SR-R}'\text{X}^* + \text{VW}$ (C) $\text{SR}'\text{X}^* + \text{YR}''\text{Z} \rightarrow \text{SR}'\text{-R}''\text{Z}^* + \text{XY}$	[294,301]

Note: ¹ Organic polymer; ² Inorganic-organic hybrid polymer; ³ Organic or inorganic-organic hybrid polymers.

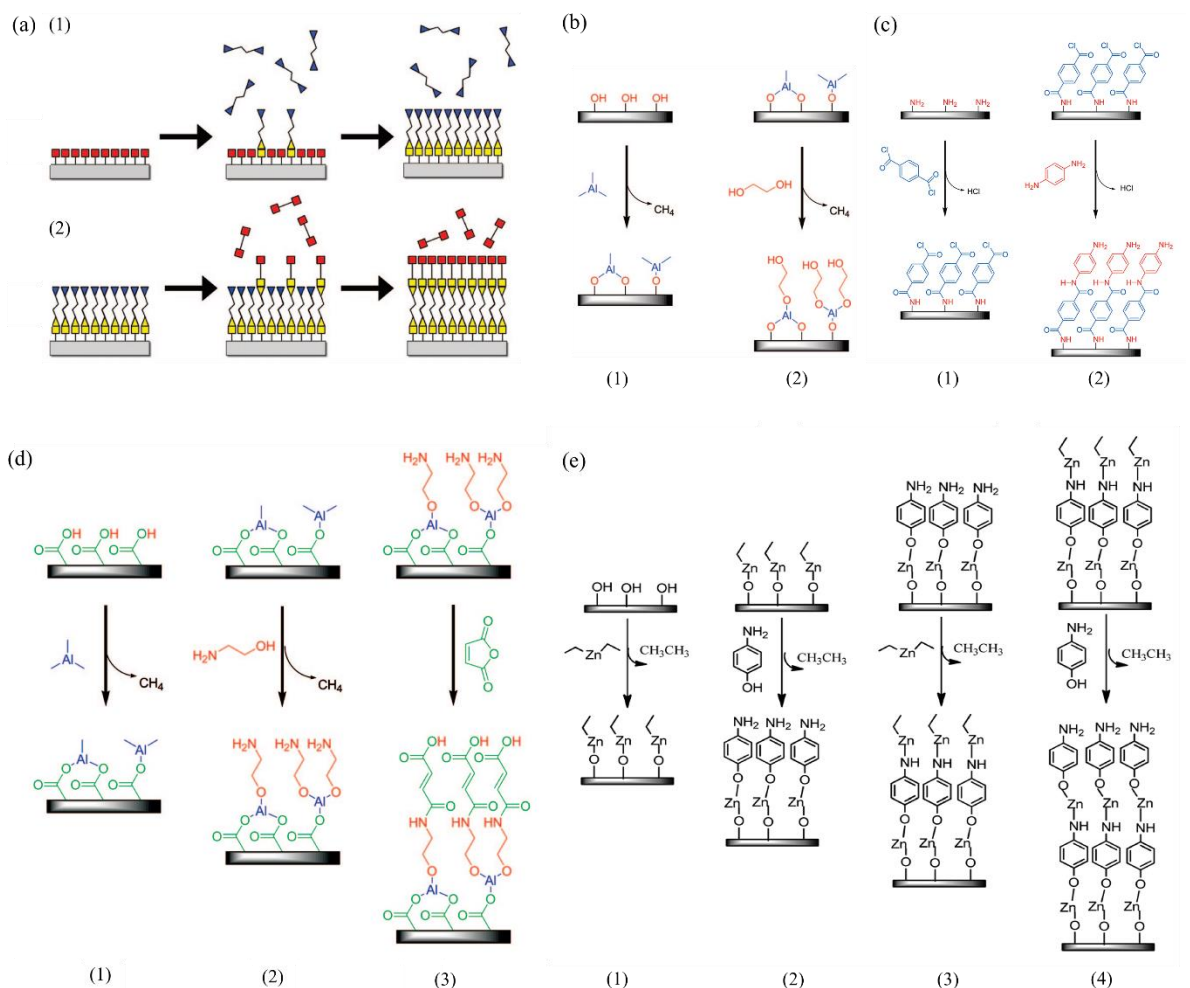


Figure 3. (a) Schematic representation of MLD using self-limiting surface chemistry and an AB binary reaction sequence [294]. Reprinted (adapted) with permission from ref. [294]. Copyright (2009) American Chemical Society; (b) Illustration of surface chemistry for two-step alucone MLD using TMA and EG as reactants [270]. Reprinted (adapted) with permission from ref. [270]. Copyright (2008) American Chemical Society; (c) Illustration of surface chemistry for PPTA MLD using ClCOC₆H₄COCl (TC) and NH₂C₆H₄NH₂ (PD) as reactants [294]. Reprinted (adapted) with permission from ref. [294]. Copyright (2009) American Chemical Society; (d) Illustration of surface chemistry for three-step alucone MLD with TMA, EA, and MA as reactants [301]. Reprinted (adapted) with permission from ref. [301]. Copyright (2009) American Chemical Society; (e) Suggested growth sequence for the Zn-AP film over a thin seed layer of ZnO on a Si substrate. The surface was left covered with -NH₂ groups [302]. Reprinted (adapted) with permission from ref. [302]. Copyright (2003) Royal Society of Chemistry.

Many ALD/MLD reviews [194,230,285,286,291,303] indicated that both ALD and MLD realize precise control over film quality (uniformity, conformality) and thickness. They are effective in

improving the performance of different battery systems (lithium ion batteries, sodium-ion batteries, Li-S batteries) by protecting electrode surface, designing novel electrodes, preparing solid-state electrolytes, modifying separators and building stable SEI layers.

1.4 Motivation and Objective

Currently, in modern societies, demanding energy requirements and environmental problems attributed to fossil fuels combustion drive the battery development. In this case, the whole society is prone to use cleaner and more renewable energy sources, which can be realized by energy technology conversation through energy storage devices. Therefore, batteries are significantly important. Lithium-ion batteries are considered as promising technology. They are widely applied in our daily life, such as telephones, clock-radios, security alarms, smoke detectors, portable fluorescent, portable tools, portable test meters, hedge trimmers, lawnmowers, portable radios, TVs, toothbrushes, hearing aids, watches and cameras. High performance lithium ion batteries are effective in providing stable energy supply, which can solve the problem of limited energy. ALD and MLD can be employed to develop high performance LIBs by surface coating, electrode design, solid state electrolyte preparation and separator modification.

In this thesis, I will work on three parts as the following: (1) Investigating the growth properties of different ALD/MLD films (Al_2O_3 , ZnO, TiO_2 , AlGL and ZnGL) using quartz crystal microbalance QCM. SEM was employed to characterize the morphology of deposited films; (2) Modifying the Si anode-electrolyte interface in LIBs using ALD-ZnO; and (3) Studying the effects of ALD coatings (Al_2O_3 , ZnO) on stabilizing lithium metal. Different types of batteries (bare Li/Cu, bare Li/Ni foam, Al_2O_3 coated Li/Cu, Al_2O_3 coated Li/Ni foam, ZnO coated Li/Cu, ZnO coated Li/Ni foam) were assembled and their electrochemical behavior were studied. 4nm Al_2O_3 could effectively stabilize lithium metal. And 4nm Al_2O_3 coated Li/Ni foam achieved the

highest Coulombic efficiency. In this section, SEM and EDX were used to characterize the morphology of Li metal before and after battery cycling. These three parts will be respectively discussed in Chapter 2, 3, and 4.

1.5 References

- [1] M. Winter, R.J. Brodd, What are batteries, fuel cells, and supercapacitors? *Chem. Rev* 104 (2004) 4245-4270.
- [2] Gold Peak Industries Ltd, Lithium ion technical handbook, (2007).
- [3] Sanyo: Harding energy specification, Archived 27 December 2015 at the Wayback Machine, listing self-discharge rate of 0.3%/mo.
- [4] Sanyo: Overview of lithium ion batteries, Archived 3 March 2016 at the Wayback Machine, listing self-discharge rate of 2%/mo.
- [5] Lithium-ion battery charging basics, PowerStream Technologies. Retrieved 4 December 2010.
- [6] BU-502: Discharging at high and low temperatures, https://batteryuniversity.com/learn/article/discharging_at_high_and_low_temperatures.
- [7] BU-501a: Discharge characteristics of Li-ion, https://batteryuniversity.com/learn/article/discharge_characteristics_li.
- [8] BU-401a: Fast and ultra-fast Chargers, https://batteryuniversity.com/learn/article/ultra_fast_chargers.
- [9] A. Avni, M.A. Blázquez, Can plant biotechnology help in solving our food and energy shortage in the future? *Curr. Opin. Biotechnol.* 22 (2011) 220-223.
- [10] P. Papon, Énergie: science et technique, remparts contre la pénurie? *Futuribles* 346 (2008) 39-54.
- [11] G.O.d. Rocha, J.B.d. Andrade, A.L.N. Guarieiro, L.L.N. Guarieiro, L.P. Ramos, Chemistry without borders: the energy challenges, *Química Nova* 36 (2013) 1540-1551.
- [12] N. Armaroli, V. Balzani, The future of energy supply: challenges and opportunities, *Angewandte Chemie International Edition* 46 (2007) 52-66.
- [13] T.R. Cook, D.K. Dogutan, S.Y. Reece, Y. Surendranath, T.S. Teets, D.G. Nocera, Solar energy supply and storage for the legacy and nonlegacy worlds, *Chem. Rev.* 110 (2010) 6474-6502.
- [14] Q. Wu, G. Han, Sulfur isotope and chemical composition of the rainwater at the Three Gorges Reservoir, *Atmos. Res.* 155 (2015) 130-140.

- [15] G. Nicoletti, N. Arcuri, G. Nicoletti, R. Bruno, A technical and environmental comparison between hydrogen and some fossil fuels, *Energy Conversion and Management* 89 (2015) 205-213.
- [16] G. Cao, X. Zhang, S. Gong, X. An, Y. Wang, Emission inventories of primary particles and pollutant gases for China, *Chinese Science Bulletin* 56 (2011) 781-788.
- [17] F. Petrakopoulou, D. Iribarren, J. Dufour, Life-cycle performance of natural gas power plants with pre-combustion CO₂ capture, *Greenhouse Gases: Science and Technology* 5 (2015) 268-276.
- [18] I.S. Modahl, C. Askham, K. Lyng, A. Brekke, Weighting of environmental trade-offs in CCS-an LCA case study of electricity from a fossil gas power plant with post-combustion CO₂ capture, transport and storage, *The International Journal of Life Cycle Assessment* 17 (2012) 932-943.
- [19] C. Körner, D. Basler, Phenology under global warming, *Science* 327 (2010) 1461-1462.
- [20] A. Dai, Drought under global warming: a review, *Wiley Interdisciplinary Reviews: Climate Change* 2 (2011) 45-65.
- [21] C.D. Koven, B. Ringeval, P. Friedlingstein, P. Ciais, P. Cadule, D. Khvorostyanov, et al., Permafrost carbon-climate feedbacks accelerate global warming, *Proc. Natl. Acad. Sci. U. S. A.* 108 (2011) 14769-14774.
- [22] P.M. Cox, R.A. Betts, C.D. Jones, S.A. Spall, I.J. Totterdell, Acceleration of global warming due to carbon-cycle feedbacks in a coupled climate model, *Nature* 408 (2000) 184-187.
- [23] T.L. Root, J.T. Price, K.R. Hall, S.H. Schneider, C. Rosenzweig, J.A. Pounds, Fingerprints of global warming on wild animals and plants, *Nature* 421 (2003) 57-60.
- [24] S. Bilgen, K. Kaygusuz, A. Sari, Renewable energy for a clean and sustainable future, *Energy Sources* 26 (2004) 1119-1129.
- [25] G. Boyle, Renewable energy, *Renewable Energy*, by Edited by Godfrey Boyle, pp.456. Oxford University Press, May 2004. ISBN-10: 0199261784. ISBN-13: 9780199261789 (2004) 456.
- [26] S.R. Bull, Renewable energy today and tomorrow, *Proc IEEE* 89 (2001) 1216-1226.
- [27] O. Ellabban, H. Abu-Rub, F. Blaabjerg, Renewable energy resources: Current status, future prospects and their enabling technology, *Renewable and Sustainable Energy Reviews* 39 (2014) 748-764.

- [28] N. Panwar, S. Kaushik, S. Kothari, Role of renewable energy sources in environmental protection: a review, *Renewable and Sustainable Energy Reviews* 15 (2011) 1513-1524.
- [29] I. Eilks, T. Witteck, V. Pietzner, A critical discussion of the efficacy of using visual learning aids from the internet to promote understanding, illustrated with examples explaining the Daniell voltaic cell. *Eurasia Journal of Mathematics, Science & Technology Education* 5 (2009) 145-152.
- [30] A. Boulabiar, K. Bouraoui, M. Chastrette, M. Abderrabba, A historical analysis of the Daniell cell and electrochemistry teaching in French and Tunisian textbooks, *J. Chem. Educ.* 81 (2004) 754-757.
- [31] Z. Rogulski, A. Czerwiński, Cathode modification in the Leclanché cell, *Journal of Solid State Electrochemistry* 7 (2003) 118-121.
- [32] S. Karunathilaka, N. Hampson, R. Leek, T. Sinclair, The impedance of the Leclanché cell. II. The impedance of the individual cell components, *J. Appl. Electrochem.* 10 (1980) 603-609.
- [33] S. Karunathilaka, N. Hampson, R. Leek, T. Sinclair, The impedance of the Leclanché cell. III. The impedance of the cell at different stages of discharge and state-of-charge indication by the impedance method, *J. Appl. Electrochem.* 10 (1980) 799-806.
- [34] Y. Paik, W. Bowden, T. Richards, R. Sirotina, C.P. Grey, ^2H MAS NMR and SPECS Studies of $\gamma\text{-MnO}_2$ Reduction in Zinc Alkaline Primary Batteries, *J. Electrochem. Soc.* 151 (2004) A998-A1011.
- [35] S.U. Falk, A.J. Salkind, *Alkaline storage batteries*, (1969).
- [36] S. Zaromb, The use and behavior of aluminum anodes in alkaline primary batteries, *J. Electrochem. Soc.* 109 (1962) 1125-1130.
- [37] A. Urfer, G. Lawrance, D. Swinkels, The role of particle size in cathode optimization in alkaline primary batteries, *J. Appl. Electrochem.* 31 (2001) 341-347.
- [38] G. Nazri, G. Pistoia, *Lithium batteries: science and technology*, Springer Science & Business Media (2008).
- [39] W. Yalen, M. Gulbinska, F. Puglia, R. Gitzendanner, Yardney lithium-ion aerospace batteries: Recent experience and critical path forward, 6th International Energy Conversion Engineering Conference, (2008) 5692.
- [40] H. Bode, *Lead-acid batteries*, (1977).
- [41] K.R. Bullock, *Lead/acid batteries*, *J. Power Sources* 51 (1994) 1-17.
- [42] J.J. Rowlette, *Lead-acid battery*, U.S. Patent No. 4,405,697. (1983).

- [43] D.B. Edwards, W.E. Rippel, Lead-acid battery, U.S. Patent No. 4,603,093. (1986).
- [44] C. Nogueira, F. Delmas, New flowsheet for the recovery of cadmium, cobalt and nickel from spent Ni-Cd batteries by solvent extraction, *Hydrometallurgy* 52 (1999) 267-287.
- [45] B.R. Reddy, D.N. Priya, S.V. Rao, P. Radhika, Solvent extraction and separation of Cd (II), Ni (II) and Co (II) from chloride leach liquors of spent Ni-Cd batteries using commercial organo-phosphorus extractants, *Hydrometallurgy* 77 (2005) 253-261.
- [46] B.R. Reddy, D.N. Priya, K.H. Park, Separation and recovery of cadmium (II), cobalt (II) and nickel (II) from sulphate leach liquors of spent Ni-Cd batteries using phosphorus based extractants, *Separation and Purification Technology* 50 (2006) 161-166.
- [47] L. Serrao, Z. Chehab, Y. Guezennee, G. Rizzoni, An aging model of Ni-MH batteries for hybrid electric vehicles, *Vehicle power and propulsion, 2005 IEEE conference.* (2005) 78-85.
- [48] C. Rongeat, M. Grosjean, S. Ruggeri, M. Dehmas, S. Bourlot, S. Marcotte, et al., Evaluation of different approaches for improving the cycle life of MgNi-based electrodes for Ni-MH batteries, *J. Power Sources* 158 (2006) 747-753.
- [49] Y. Liu, Y. Cao, L. Huang, M. Gao, H. Pan, Rare earth-Mg-Ni-based hydrogen storage alloys as negative electrode materials for Ni/MH batteries, *J. Alloys Compounds* 509 (2011) 675-686.
- [50] T. Sakai, I. Uehara, H. Ishikawa, R&D on metal hydride materials and Ni-MH batteries in Japan, *J. Alloys Compounds* 293 (1999) 762-769.
- [51] B. Zhu, N. Liu, M. McDowell, Y. Jin, Y. Cui, J. Zhu, Interfacial stabilizing effect of ZnO on Si anodes for lithium ion battery, *Nano Energy* 13 (2015) 620-625.
- [52] E.M. Erickson, C. Ghanty, D. Aurbach, New horizons for conventional lithium ion battery technology, *The journal of physical chemistry letters* 5 (2014) 3313-3324.
- [53] B. Scrosati, Recent advances in lithium ion battery materials, *Electrochim. Acta* 45 (2000) 2461-2466.
- [54] B. Boukamp, R. Huggins, Lithium ion conductivity in lithium nitride, *Physics Letters A* 58 (1976) 231-233.
- [55] M.S. Whittingham, Lithium batteries and cathode materials, *Chem. Rev.* 104 (2004) 4271-4302.
- [56] J. Tarascon, M. Armand, *Materials for sustainable energy: A collection of peer-reviewed research and review articles from nature publishing group*, World Scientific, (2011).
- [57] Keywords to understanding Sony Energy Devices, (1991). <https://archive.is/jo8XI>

- [58] Y. Liu, Y. Qiao, W. Zhang, Z. Li, X. Hu, L. Yuan, et al., Coral-like α -MnS composites with N-doped carbon as anode materials for high-performance lithium-ion batteries, *Journal of Materials Chemistry* 22 (2012) 24026-24033.
- [59] D. Zhang, Y. Mai, J. Xiang, X. Xia, Y. Qiao, J. Tu, FeS₂/C composite as an anode for lithium ion batteries with enhanced reversible capacity, *J. Power Sources* 217 (2012) 229-235.
- [60] J. Yan, H. Huang, J. Zhang, Z. Liu, Y. Yang, A study of novel anode material CoS₂ for lithium ion battery, *J. Power Sources* 146 (2005) 264-269.
- [61] Y. Wang, H. Xia, L. Lu, J. Lin, Excellent performance in lithium-ion battery anodes: rational synthesis of Co(CO₃)_{0.5}(OH)_{0.11}H₂O nanobelt array and its conversion into mesoporous and single-crystal Co₃O₄, *ACS nano* 4 (2010) 1425-1432.
- [62] J. Cabana, L. Monconduit, D. Larcher, M.R. Palacin, Beyond intercalation-based Li-ion batteries: the state of the art and challenges of electrode materials reacting through conversion reactions, *Adv Mater* 22 (2010) E170-E192.
- [63] S. Chou, J. Wang, H. Liu, S. Dou, Rapid synthesis of Li₄Ti₅O₁₂ microspheres as anode materials and its binder effect for lithium-ion battery, *The Journal of Physical Chemistry C* 115 (2011) 16220-16227.
- [64] A.R. Armstrong, G. Armstrong, J. Canales, R. García, P.G. Bruce, Lithium-ion intercalation into TiO₂-B nanowires, *Adv Mater* 17 (2005) 862-865.
- [65] Y. Ein-Eli, A new perspective on the formation and structure of the solid electrolyte interface at the graphite anode of Li-ion cells, *Electrochemical and solid-state letters* 2 (1999) 212-214.
- [66] W. Zhang, A review of the electrochemical performance of alloy anodes for lithium-ion batteries, *J. Power Sources* 196 (2011) 13-24.
- [67] N. Liu, H. Wu, M.T. McDowell, Y. Yao, C. Wang, Y. Cui, A yolk-shell design for stabilized and scalable Li-ion battery alloy anodes, *Nano letters* 12 (2012) 3315-3321.
- [68] C. Park, J. Kim, H. Kim, H. Sohn, Li-alloy based anode materials for Li secondary batteries, *Chem. Soc. Rev.* 39 (2010) 3115-3141.
- [69] M. Yu, W. Yuan, C. Li, J. Hong, G. Shi, Performance enhancement of a graphene-sulfur composite as a lithium-sulfur battery electrode by coating with an ultrathin Al₂O₃ film via atomic layer deposition, *Journal of Materials Chemistry A* 2 (2014) 7360-7366.
- [70] K. Xu, Nonaqueous liquid electrolytes for lithium-based rechargeable batteries, *Chem. Rev.* 104 (2004) 4303-4418.

- [71] D. Deng, M.G. Kim, J.Y. Lee, J. Cho, Green energy storage materials: Nanostructured TiO₂ and Sn-based anodes for lithium-ion batteries, *Energy & Environmental Science* 2 (2009) 818-837.
- [72] P. Notten, H. Bergveld, W. Kruijt, Battery management systems: design by modeling, Kluwer Academic Publisher 1 (2002) 9-30.
- [73] S. Dhameja, Electric vehicle battery systems, Elsevier (2001).
- [74] G. Amatucci, J. Tarascon, L. Klein, CoO₂, the end member of the Li_xCoO₂ solid solution, *J. Electrochem. Soc.* 143 (1996) 1114-1123.
- [75] H.C. Choi, Y.M. Jung, I. Noda, S.B. Kim, A study of the mechanism of the electrochemical reaction of lithium with CoO by two-dimensional soft X-ray absorption spectroscopy (2D XAS), 2D Raman, and 2D heterospectral XAS-Raman correlation analysis, *The Journal of Physical Chemistry B* 107 (2003) 5806-5811.
- [76] G.C. Congress, Panasonic develops new higher-capacity 18650 Li-Ion cells, Application of Silicon-based Alloy in Anode <http://www.greencarcongress.com/2009/12/panasonic-20091225.html> (2014-04-13) (2009)
- [77] N. Choi, Z. Chen, S.A. Freunberger, X. Ji, Y. Sun, K. Amine, et al., Challenges facing lithium batteries and electrical double-layer capacitors, *Angewandte Chemie International Edition* 51 (2012) 9994-10024.
- [78] H. Wu, Y. Cui, Designing nanostructured Si anodes for high energy lithium ion batteries, *Nano Today* 7 (2012) 414-429.
- [79] P. Parpot, A. Bettencourt, G. Chamoulaud, K. Kokoh, E. Belgsir, Electrochemical investigations of the oxidation-reduction of furfural in aqueous medium: Application to electrosynthesis, *Electrochim. Acta* 49 (2004) 397-403.
- [80] J. Vetter, P. Novák, M.R. Wagner, C. Veit, K. Möller, J. Besenhard, et al., Ageing mechanisms in lithium-ion batteries, *J. Power Sources* 147 (2005) 269-281.
- [81] M. Wohlfahrt-Mehrens, C. Vogler, J. Garche, Aging mechanisms of lithium cathode materials, *J. Power Sources* 127 (2004) 58-64.
- [82] D. Deng, Li-ion batteries: basics, progress, and challenges, *Energy Science & Engineering* 3 (2015) 385-418.
- [83] D. MacNeil, J.R. Dahn, The reactions of Li_{0.5}CoO₂ with nonaqueous solvents at elevated temperatures, *J. Electrochem. Soc.* 149 (2002) A912-A919.
- [84] D. MacNeil, J. Dahn, The reaction of charged cathodes with nonaqueous solvents and electrolytes: I. Li_{0.5}CoO₂, *J. Electrochem. Soc.* 148 (2001) A1205-A1210.

- [85] L. Lu, X. Han, J. Li, J. Hua, M. Ouyang, A review on the key issues for lithium-ion battery management in electric vehicles, *J. Power Sources* 226 (2013) 272-288.
- [86] L. Ji, Z. Lin, M. Alcoutlabi, X. Zhang, Recent developments in nanostructured anode materials for rechargeable lithium-ion batteries, *Energy & Environmental Science* 4 (2011) 2682-2699.
- [87] A.S. Arico, P. Bruce, B. Scrosati, J. Tarascon, W. Van Schalkwijk, Nanostructured materials for advanced energy conversion and storage devices, *Nature materials* 4 (2005) 366.
- [88] M.S. Whittingham, Inorganic nanomaterials for batteries, *Dalton Transactions* (2008) 5424-5431.
- [89] B. Ellis, P.S. Herle, Y. Rho, L. Nazar, R. Dunlap, L.K. Perry, et al., Nanostructured materials for lithium-ion batteries: Surface conductivity vs. bulk ion/electron transport, *Faraday Discuss.* 134 (2007) 119-141.
- [90] M. Park, G. Wang, Y. Kang, D. Wexler, S. Dou, H. Liu, Preparation and electrochemical properties of SnO₂ nanowires for application in lithium-ion batteries, *Angewandte Chemie International Edition* 46 (2007) 750-753.
- [91] A. Shukla, T.P. Kumar, Materials for next-generation lithium batteries, *Curr. Sci.* 94 (2008) 314-331.
- [92] S. Iijima, Helical microtubules of graphitic carbon, *Nature (London)* 354 (1991) 56-58.
- [93] J. Zhou, H. Song, B. Fu, B. Wu, X. Chen, Synthesis and high-rate capability of quadrangular carbon nanotubes with one open end as anode materials for lithium-ion batteries, *Journal of Materials Chemistry* 20 (2010) 2794-2800.
- [94] R. Lv, L. Zou, X. Gui, F. Kang, Y. Zhu, H. Zhu, et al., High-yield bamboo-shaped carbon nanotubes from cresol for electrochemical application, *Chemical Communications* 17 (2008) 2046-2048.
- [95] L. Ji, Z. Lin, A.J. Medford, X. Zhang, In-situ encapsulation of nickel particles in electrospun carbon nanofibers and the resultant electrochemical performance, *Chemistry-A European Journal* 15 (2009) 10718-10722.
- [96] V. Subramanian, H. Zhu, B. Wei, High rate reversibility anode materials of lithium batteries from vapor-grown carbon nanofibers, *The Journal of Physical Chemistry B* 110 (2006) 7178-7183.
- [97] C. Li, X. Yin, L. Chen, Q. Li, T. Wang, Porous carbon nanofibers derived from conducting polymer: synthesis and application in lithium-ion batteries with high-rate capability, *The Journal of Physical Chemistry C* 113 (2009) 13438-13442.

- [98] A.V. Murugan, T. Muraliganth, A. Manthiram, Comparison of microwave assisted solvothermal and hydrothermal syntheses of LiFePO_4/C nanocomposite cathodes for lithium ion batteries, *The Journal of Physical Chemistry C* 112 (2008) 14665-14671.
- [99] T. Bhardwaj, A. Antic, B. Pavan, V. Barone, B.D. Fahlman, Enhanced electrochemical lithium storage by graphene nanoribbons, *J. Am. Chem. Soc.* 132 (2010) 12556-12558.
- [100] P. Guo, H. Song, X. Chen, Electrochemical performance of graphene nanosheets as anode material for lithium-ion batteries, *Electrochemistry Communications* 11 (2009) 1320-1324.
- [101] T. Wang, X. Liu, D. Zhao, Z. Jiang, The unusual electrochemical characteristics of a novel three-dimensional ordered bicontinuous mesoporous carbon, *Chemical physics letters* 389 (2004) 327-331.
- [102] C.J. Meyers, S.D. Shah, S.C. Patel, R.M. Sneeringer, C.A. Bessel, N.R. Dollahon, et al., Templated synthesis of carbon materials from zeolites (Y, beta, and ZSM-5) and a montmorillonite clay (K10): Physical and electrochemical characterization, *The Journal of Physical Chemistry B* 105 (2001) 2143-2152.
- [103] F. Cheng, Z. Tao, J. Liang, J. Chen, Template-directed materials for rechargeable lithium-ion batteries, *Chemistry of Materials* 20 (2007) 667-681.
- [104] X. Meng, Y. Zhang, S. Sun, R. Li, X. Sun, Three growth modes and mechanisms for highly structure-tunable SnO_2 nanotube arrays of template-directed atomic layer deposition, *Journal of Materials Chemistry* 21 (2011) 12321-12330.
- [105] J.T. Korhonen, P. Hiekkataipale, J. Malm, M. Karppinen, O. Ikkala, R.H. Ras, Inorganic hollow nanotube aerogels by atomic layer deposition onto native nanocellulose templates, *ACS nano* 5 (2011) 1967-1974.
- [106] S. Kim, T.H. Han, J. Kim, H. Gwon, H. Moon, S. Kang, et al., Fabrication and electrochemical characterization of TiO_2 three-dimensional nanonetwork based on peptide assembly, *Acs Nano* 3 (2009) 1085-1090.
- [107] K. Gerasopoulos, X. Chen, J. Culver, C. Wang, R. Ghodssi, Self-assembled Ni/TiO_2 nanocomposite anodes synthesized via electroless plating and atomic layer deposition on biological scaffolds, *Chemical Communications* 46 (2010) 7349-7351.
- [108] Y. Wang, G. Cao, Developments in nanostructured cathode materials for high-performance lithium-ion batteries, *Adv Mater* 20 (2008) 2251-2269.
- [109] M. Kunduraci, G. Amatucci, Synthesis and characterization of nanostructured 4.7 V $\text{Li}_x\text{Mn}_{1.5}\text{Ni}_{0.5}\text{O}_4$ spinels for high-power lithium-ion batteries, *J. Electrochem. Soc.* 153 (2006) A1345-A1352.

- [110] J.C. Arrebola, A. Caballero, M. Cruz, L. Hernán, J. Morales, E.R. Castellón, Crystallinity control of a nanostructured $\text{LiNi}_{0.5}\text{Mn}_{1.5}\text{O}_4$ spinel via polymer-assisted synthesis: A method for improving its rate capability and performance in 5 V lithium batteries, *Advanced Functional Materials* 16 (2006) 1904-1912.
- [111] K. Takahashi, S.J. Limmer, Y. Wang, G. Cao, Growth and electrochemical properties of single-crystalline V_2O_5 nanorod arrays, *Japanese journal of applied physics* 44 (2005) 662-668.
- [112] K. Takahashi, S.J. Limmer, Y. Wang, G. Cao, Synthesis and electrochemical properties of single-crystal V_2O_5 nanorod arrays by template-based electrodeposition, *The Journal of Physical Chemistry B* 108 (2004) 9795-9800.
- [113] W. West, N. Myung, J. Whitacre, B. Ratnakumar, Electrodeposited amorphous manganese oxide nanowire arrays for high energy and power density electrodes, *J. Power Sources* 126 (2004) 203-206.
- [114] F. Cheng, J. Zhao, W. Song, C. Li, H. Ma, J. Chen, et al., Facile controlled synthesis of MnO_2 nanostructures of novel shapes and their application in batteries, *Inorg. Chem.* 45 (2006) 2038-2044.
- [115] J. Janek, W.G. Zeier, A solid future for battery development, *Nature Energy* 1 (2016) 16141.
- [116] R. Chen, W. Qu, X. Guo, L. Li, F. Wu, The pursuit of solid-state electrolytes for lithium batteries: from comprehensive insight to emerging horizons, *Materials Horizons* 3 (2016) 487-516.
- [117] J. Gao, Y. Zhao, S. Shi, H. Li, Lithium-ion transport in inorganic solid state electrolyte, *Chinese Physics B* 25 (2015) 018211.
- [118] V. Thangadurai, S. Narayanan, D. Pinzarú, Garnet-type solid-state fast Li ion conductors for Li batteries: critical review, *Chem. Soc. Rev.* 43 (2014) 4714-4727.
- [119] Z. Lin, C. Liang, Lithium-sulfur batteries: from liquid to solid cells, *Journal of Materials Chemistry A* 3 (2015) 936-958.
- [120] J.W. Fergus, Ceramic and polymeric solid electrolytes for lithium-ion batteries, *J. Power Sources* 195 (2010) 4554-4569.
- [121] J. Song, Y. Wang, C.C. Wan, Review of gel-type polymer electrolytes for lithium-ion batteries, *J. Power Sources* 77 (1999) 183-197.
- [122] W.H. Meyer, Polymer electrolytes for lithium-ion batteries, *Adv Mater* 10 (1998) 439-448.

- [123] J. Trevey, J.S. Jang, Y.S. Jung, C.R. Stoldt, S. Lee, Glass-ceramic $\text{Li}_2\text{S}-\text{P}_2\text{S}_5$ electrolytes prepared by a single step ball milling process and their application for all-solid-state lithium-ion batteries, *Electrochemistry communications* 11 (2009) 1830-1833.
- [124] H. Okamoto, S. Hikazudani, C. Inazumi, T. Takeuchi, M. Tabuchi, K. Tatsumi, Upper voltage and temperature dependencies for an all-solid-state In/LiCoO_2 cell using sulfide glass electrolyte, *Electrochemical and Solid-State Letters* 11 (2008) A97-A100.
- [125] W. Yao, S.W. Martin, Ionic conductivity of glasses in the MI M_2S ($0.1\text{Ga}_2\text{S}_3+0.9\text{GeS}_2$) system (M= Li, Na, K and Cs), *Solid State Ionics* 178 (2008) 1777-1784.
- [126] Z. Nagamedianova, A. Hernández, E. Sánchez, Conductivity studies on $\text{LiX}-\text{Li}_2\text{S}-\text{Sb}_2\text{S}_3-\text{P}_2\text{S}_5$ (X= LiI or Li_3PO_4) glassy system, *Ionics* 12 (2006) 315-322.
- [127] T. Inada, T. Kobayashi, N. Sonoyama, A. Yamada, S. Kondo, M. Nagao, et al., All solid-state sheet battery using lithium inorganic solid electrolyte, thio-LISICON, *J. Power Sources* 194 (2009) 1085-1088.
- [128] Z. Liu, F. Huang, J. Yang, B. Wang, J. Sun, New lithium ion conductor, thio-LISICON lithium zirconium sulfide system, *Solid State Ionics* 179 (2008) 1714-1716.
- [129] X. Li, J. Liu, M.N. Banis, A. Lushington, R. Li, M. Cai, et al., Atomic layer deposition of solid-state electrolyte coated cathode materials with superior high-voltage cycling behavior for lithium ion battery application, *Energy & Environmental Science* 7 (2014) 768-778.
- [130] S. Stramare, V. Thangadurai, W. Weppner, Lithium lanthanum titanates: a review, *Chemistry of Materials* 15 (2003) 3974-3990.
- [131] R. Murugan, V. Thangadurai, W. Weppner, Lithium ion conductivity of $\text{Li}_{5x}\text{Ba}_x\text{La}_{3-x}\text{Ta}_2\text{O}_{12}$ ($x= 0-2$) with garnet-related structure in dependence of the barium content, *Ionics* 13 (2007) 195-203.
- [132] J. Awaka, N. Kijima, Y. Takahashi, H. Hayakawa, J. Akimoto, Synthesis and crystallographic studies of garnet-related lithium-ion conductors $\text{Li}_6\text{CaLa}_2\text{Ta}_2\text{O}_{12}$ and $\text{Li}_6\text{BaLa}_2\text{Ta}_2\text{O}_{12}$, *Solid State Ionics* 180 (2009) 602-606.
- [133] J. Percival, D. Apperley, P. Slater, Synthesis and structural characterisation of the Li ion conducting garnet-related systems, $\text{Li}_6\text{ALa}_2\text{Nb}_2\text{O}_{12}$ (A= Ca, Sr), *Solid State Ionics* 179 (2008) 1693-1696.
- [134] M.P. O'Callaghan, A.S. Powell, J.J. Titman, G.Z. Chen, E.J. Cussen, Switching on fast lithium ion conductivity in garnets: The structure and transport properties of $\text{Li}_{3x}\text{Nd}_3\text{Te}_{2-x}\text{Sb}_x\text{O}_{12}$, *Chemistry of Materials* 20 (2008) 2360-2369.
- [135] J. Kim, G. Park, K. Lee, H. Park, S. Nam, S. Song, Li-B-O-N electrolytes for all-solid-state thin film batteries, *J. Power Sources* 189 (2009) 211-216.

- [136] X. Wu, Z. Wen, X. Xu, J. Han, Synthesis and ionic conductivity of Mg-doped Li_2TiO_3 , *Solid State Ionics* 179 (2008) 1779-1782.
- [137] I. Leonidov, O. Leonidova, R. Samigullina, M. Patrakeev, Structural aspects of lithium transfer in solid electrolytes $\text{Li}_{2x}\text{Zn}_{2-3x}\text{Ti}_{1+x}\text{O}_4$ ($0.33 \leq x \leq 0.67$), *Journal of Structural Chemistry* 45 (2004) 262-268.
- [138] J.S. Thokchom, N. Gupta, B. Kumar, Superionic conductivity in a lithium aluminum germanium phosphate glass-ceramic, *J. Electrochem. Soc.* 155 (2008) A915-A920.
- [139] J. Xie, N. Imanishi, T. Zhang, A. Hirano, Y. Takeda, O. Yamamoto, Li-ion transport in all-solid-state lithium batteries with LiCoO_2 using NASICON-type glass ceramic electrolytes, *J. Power Sources* 189 (2009) 365-370.
- [140] T. Savitha, S. Selvasekarapandian, C. Ramya, Structural and electrical conductivity studies of $\text{Li}_x\text{AlZr}[\text{PO}_4]_3$ ($x = 1.8, 2.0, 2.2$), solid electrolyte for lithium-rechargeable batteries, *Journal of Solid State Electrochemistry* 12 (2008) 857-860.
- [141] K. Nagamine, K. Hirose, T. Honma, T. Komatsu, Lithium ion conductive glass-ceramics with $\text{Li}_3\text{Fe}_2(\text{PO}_4)_3$ and YAG laser-induced local crystallization in lithium iron phosphate glasses, *Solid State Ionics* 179 (2008) 508-515.
- [142] Y. Hamon, A. Douard, F. Sabary, C. Marcel, P. Vinatier, B. Pecquenard, et al., Influence of sputtering conditions on ionic conductivity of LiPON thin films, *Solid State Ionics* 177 (2006) 257-261.
- [143] M. Marzantowicz, J. Dygas, F. Krok, A. Tomaszewska, Z. Florjańczyk, E. Zygadło-Monikowska, et al., Star-branched poly (ethylene oxide) $\text{LiN}(\text{CF}_3\text{SO}_2)_2$: A promising polymer electrolyte, *J. Power Sources* 194 (2009) 51-57.
- [144] H. Pitawala, M. Dissanayake, V. Seneviratne, B. Mellander, I. Albinson, Effect of plasticizers (EC or PC) on the ionic conductivity and thermal properties of the $(\text{PEO})_9\text{LiTf}:\text{Al}_2\text{O}_3$ nanocomposite polymer electrolyte system, *Journal of Solid State Electrochemistry* 12 (2008) 783-789.
- [145] T. Uno, S. Kawaguchi, M. Kubo, T. Itoh, Ionic conductivity and thermal property of solid hybrid polymer electrolyte composed of oligo (ethylene oxide) unit and butyrolactone unit, *J. Power Sources* 178 (2008) 716-722.
- [146] K. Ishmukhametova, O. Yarmolenko, L. Bogdanova, B. Rozenberg, O. Efimov, New solid polymer electrolytes based on polyester diacrylate for lithium power sources, *Russian J. Electrochem.* 45 (2009) 558-563.
- [147] Z. Bakenov, M. Nakayama, M. Wakihara, I. Taniguchi, Lithium AlPO_4 composite polymer battery with nanostructured LiMn_2O_4 cathode, *Journal of Solid State Electrochemistry* 12 (2008) 295-302.

- [148] T. Niitani, M. Amaike, H. Nakano, K. Dokko, K. Kanamura, Star-shaped polymer electrolyte with microphase separation structure for all-solid-state lithium batteries, *J. Electrochem. Soc.* 156 (2009) A577-A583.
- [149] P. Raghavan, X. Zhao, J. Kim, J. Manuel, G.S. Chauhan, J. Ahn, et al., Ionic conductivity and electrochemical properties of nanocomposite polymer electrolytes based on electrospun poly (vinylidene fluoride-co-hexafluoropropylene) with nano-sized ceramic fillers, *Electrochim. Acta* 54 (2008) 228-234.
- [150] D. Zhou, G. Wang, W. Li, G. Li, C. Tan, M. Rao, et al., Preparation and performances of porous polyacrylonitrile-methyl methacrylate membrane for lithium-ion batteries, *J. Power Sources* 184 (2008) 477-480.
- [151] X. Huang, Separator technologies for lithium-ion batteries, *Journal of Solid State Electrochemistry* 15 (2011) 649-662.
- [152] S.S. Zhang, A review on the separators of liquid electrolyte Li-ion batteries, *J. Power Sources* 164 (2007) 351-364.
- [153] S. Nagou, S. Nakamura, Microporous film and process for production thereof, U.S. Patent No. 4791144. (1988).
- [154] P. Jacoby, C.W. Bauer, Oriented porous polypropylene films, U.S. Patent No. 4975469. (1990).
- [155] N. Kaimai, K. Takita, K. Kono, H. Funaoka, Method of producing highly permeable microporous polyolefin membrane, U.S. Patent No. 6,153,133. (2000).
- [156] A. Hashimoto, K. Yagi, H. Mantoku, Porous film of high molecular weight polyolefin and process for producing same, U.S. Patent No. 6,048,607. (2000).
- [157] C. Chandavasu, M. Xanthos, K.K. Sirkar, C. Gogos, Preparation of microporous films from immiscible blends via melt processing and stretching, U.S. Patent No. 6,824,680. (2004).
- [158] S.J. Law, H. Street, G.J. Askew, Method of manufacture of nonwoven fabric, U.S. Patent No. 6,358,461. (2002).
- [159] P. Kritzer, Nonwoven support material for improved separators in Li-polymer batteries, *J. Power Sources* 161 (2006) 1335-1340.
- [160] Y.M. Lee, N. Choi, J.A. Lee, W. Seol, K. Cho, H. Jung, et al., Electrochemical effect of coating layer on the separator based on PVdF and PE non-woven matrix, *J. Power Sources* 146 (2005) 431-435.

- [161] K.M. Kim, N. Park, K.S. Ryu, S.H. Chang, Characteristics of PVdF-HFP/TiO₂ composite membrane electrolytes prepared by phase inversion and conventional casting methods, *Electrochim. Acta* 51 (2006) 5636-5644.
- [162] D. Takemura, S. Aihara, K. Hamano, M. Kise, T. Nishimura, H. Urushibata, et al., A powder particle size effect on ceramic powder based separator for lithium rechargeable battery, *J. Power Sources* 146 (2005) 779-783.
- [163] S.A. Carlson, Q. Ying, Z. Deng, T.A. Skotheim, Separators for electrochemical cells, U.S. Patent No. 6,306,545. (2001).
- [164] H.T. Taskier, Hydrophilic polymer coated microporous membranes capable of use as a battery separator, U.S. Patent No. 4,359,510. (1982).
- [165] S. Senyarich, P. Viaud, Method of forming a separator for alkaline electrolyte secondary electric cell, U.S. Patent No. 6,042,970. (2000).
- [166] M. Urairi, T. Tachibana, K. Matsumoto, T. Shinomura, H. Iida, K. Kawamura, et al., Process for producing a wind-type alkaline secondary battery, U.S. Patent No. 5,558,682. (1996).
- [167] Y. Jeong, D. Kim, Effect of thickness of coating layer on polymer-coated separator on cycling performance of lithium-ion polymer cells, *J. Power Sources* 128 (2004) 256-262.
- [168] Y.S. Jung, A.S. Cavanagh, L. Gedvilas, N.E. Widjonarko, I.D. Scott, S. Lee, et al., Improved functionality of lithium-ion batteries enabled by atomic layer deposition on the porous microstructure of polymer separators and coating electrodes, *Advanced Energy Materials* 2 (2012) 1022-1027.
- [169] H. Chen, Q. Lin, Q. Xu, Y. Yang, Z. Shao, Y. Wang, Plasma activation and atomic layer deposition of TiO₂ on polypropylene membranes for improved performances of lithium-ion batteries, *J. Membr. Sci.* 458 (2014) 217-224.
- [170] J.B. Goodenough, K. Park, The Li-ion rechargeable battery: a perspective, *J. Am. Chem. Soc.* 135 (2013) 1167-1176.
- [171] S.J. An, J. Li, C. Daniel, D. Mohanty, S. Nagpure, D.L. Wood III, The state of understanding of the lithium-ion-battery graphite solid electrolyte interphase (SEI) and its relationship to formation cycling, *Carbon* 105 (2016) 52-76.
- [172] H. Ota, K. Shima, M. Ue, J. Yamaki, Effect of vinylene carbonate as additive to electrolyte for lithium metal anode, *Electrochim. Acta* 49 (2004) 565-572.
- [173] I. Park, T. Nam, J. Kim, Diphenyloctyl phosphate as a solid electrolyte interphase forming additive for Li-ion batteries, *J. Power Sources* 244 (2013) 122-128.

- [174] H.M. Jung, S. Park, J. Jeon, Y. Choi, S. Yoon, J. Cho, et al., Fluoropropane sultone as an SEI-forming additive that outperforms vinylene carbonate, *Journal of Materials Chemistry A* 1 (2013) 11975-11981.
- [175] B. Li, Y. Wang, H. Rong, Y. Wang, J. Liu, L. Xing, et al., A novel electrolyte with the ability to form a solid electrolyte interface on the anode and cathode of a LiMn_2O_4 /graphite battery, *Journal of Materials Chemistry A* 1 (2013) 12954-12961.
- [176] Y.S. Jung, A.S. Cavanagh, A.C. Dillon, M.D. Groner, S.M. George, S. Lee, Enhanced stability of LiCoO_2 cathodes in lithium-ion batteries using surface modification by atomic layer deposition, *J. Electrochem. Soc.* 157 (2010) A75-A81.
- [177] M. Yu, A. Wang, Y. Wang, C. Li, G. Shi, An alumina stabilized ZnO-graphene anode for lithium ion batteries via atomic layer deposition, *Nanoscale* 6 (2014) 11419-11424.
- [178] Y. He, X. Yu, Y. Wang, H. Li, X. Huang, Alumina-coated patterned amorphous silicon as the anode for a lithium-ion battery with high Coulombic efficiency, *Adv Mater* 23 (2011) 4938-4941.
- [179] M.Q. Snyder, S.A. Trebukhova, B. Ravdel, M.C. Wheeler, J. DiCarlo, C.P. Tripp, et al., Synthesis and characterization of atomic layer deposited titanium nitride thin films on lithium titanate spinel powder as a lithium-ion battery anode, *J. Power Sources* 165 (2007) 379-385.
- [180] C. Ban, M. Xie, X. Sun, J.J. Travis, G. Wang, H. Sun, et al., Atomic layer deposition of amorphous TiO_2 on graphene as an anode for Li-ion batteries, *Nanotechnology* 24 (2013) 424002.
- [181] S. Bhattacharya, A.R. Riahi, A.T. Alpas, Electrochemical cycling behaviour of lithium carbonate (Li_2CO_3) pre-treated graphite anodes-SEI formation and graphite damage mechanisms, *Carbon* 77 (2014) 99-112.
- [182] M. Scott, A. Whitehead, J. Owen, Chemical formation of a solid electrolyte interface on the carbon electrode of a Li-ion cell, *J. Electrochem. Soc.* 145 (1998) 1506-1510.
- [183] Y. Ein-Eli, V.R. Koch, Chemical oxidation: A route to enhanced capacity in Li-ion graphite anodes, *J. Electrochem. Soc.* 144 (1997) 2968-2973.
- [184] Q. Pan, H. Wang, Y. Jiang, Covalent modification of natural graphite with lithium benzoate multilayers via diazonium chemistry and their application in lithium ion batteries, *Electrochemistry Communications* 9 (2007) 754-760.
- [185] Q. Pan, H. Wang, Y. Jiang, Natural graphite modified with nitrophenyl multilayers as anode materials for lithium ion batteries, *Journal of Materials Chemistry* 17 (2007) 329-334.

- [186] Y. He, B. Li, Q. Yang, H. Du, F. Kang, G. Ling, et al., Effects of current densities on the formation of LiCoO₂/graphite lithium ion battery, *Journal of Solid State Electrochemistry* 15 (2011) 1977-1985.
- [187] C. Huang, K. Huang, H. Wang, S. Liu, Y. Zeng, The effect of solid electrolyte interface formation conditions on the aging performance of Li-ion cells, *Journal of Solid State Electrochemistry* 15 (2011) 1987-1995.
- [188] M. Ritala, M. Leskela, HS Nalwa (Ed.), *Handbook of Thin Film Materials*, 1 (2001) 103.
- [189] O. Sneh, R.B. Clark-Phelps, A.R. Londergan, J. Winkler, T.E. Seidel, Thin film atomic layer deposition equipment for semiconductor processing, *Thin Solid Films* 402 (2002) 248-261.
- [190] R.F. Bunshah, *Handbook of deposition technologies for films and coatings: science, technology, and applications*, William Andrew (1994).
- [191] S. Dana, M. Liehr, M. Anderle, G. Rubloff, Kinetics of nucleation and growth of Si on SiO₂ in very low pressure SiH₄ chemical vapor deposition, *Appl. Phys. Lett.* 61 (1992) 3035-3037.
- [192] S. Boukhalifa, K. Evanoff, G. Yushin, Atomic layer deposition of vanadium oxide on carbon nanotubes for high-power supercapacitor electrodes, *Energy & Environmental Science* 5 (2012) 6872-6879.
- [193] M. Liu, X. Li, S.K. Karuturi, A.I.Y. Tok, H.J. Fan, Atomic layer deposition for nanofabrication and interface engineering, *Nanoscale* 4 (2012) 1522-1528.
- [194] X. Meng, X. Yang, X. Sun, Emerging applications of atomic layer deposition for lithium-ion battery studies, *Adv Mater* 24 (2012) 3589-3615.
- [195] X. Sun, M. Xie, G. Wang, H. Sun, A.S. Cavanagh, J.J. Travis, et al., Atomic layer deposition of TiO₂ on graphene for supercapacitors, *J. Electrochem. Soc.* 159 (2012) A364-A369.
- [196] X. Meng, X. Wang, D. Geng, C. Ozgit-Akgun, N. Schneider, J.W. Elam, Atomic layer deposition for nanomaterial synthesis and functionalization in energy technology, *Materials Horizons* 4 (2017) 133-154.
- [197] E. Ahvenniemi, A.R. Akbashev, S. Ali, M. Bechelany, M. Berdova, S. Boyadjiev, et al., Recommended reading list of early publications on atomic layer deposition-outcome of the "Virtual Project on the History of ALD", *Journal of Vacuum Science & Technology A: Vacuum, Surfaces, and Films* 35 (2017) 010801.
- [198] T. Suntola, J. Antson, Method for producing compound thin films, U.S. Patent No. 4,058,430. (1977).

- [199] T. Suntola, From Ideas to global industry-40 years of ALD in Finland, 12th International Baltic ALD conference (2014).
- [200] R.L. Puurunen, A short history of atomic layer deposition: Tuomo Suntola's atomic layer epitaxy, *Chemical Vapor Deposition* 20 (2014) 332-344.
- [201] K. Mistry, C. Allen, C. Auth, B. Beattie, D. Bergstrom, M. Bost, et al., A 45nm logic technology with high-k metal gate transistors, strained silicon, 9 Cu interconnect layers, 193nm dry patterning, and 100% Pb-free packaging, *Electron Devices Meeting, 2007. IEDM 2007. IEEE International. IEEE, (2007)* 247-250.
- [202] T. Wang, Z. Luo, C. Li, J. Gong, Controllable fabrication of nanostructured materials for photoelectrochemical water splitting via atomic layer deposition, *Chem. Soc. Rev.* 43 (2014) 7469-7484.
- [203] W. Niu, X. Li, S.K. Karuturi, D.W. Fam, H. Fan, S. Shrestha, et al., Applications of atomic layer deposition in solar cells, *Nanotechnology* 26 (2015) 064001.
- [204] X. Meng, Towards high-energy and durable lithium-ion batteries via atomic layer deposition: elegantly atomic-scale material design and surface modification, *Nanotechnology* 26 (2014) 020501.
- [205] M. Knez, K. Nielsch, L. Niinistö, Synthesis and surface engineering of complex nanostructures by atomic layer deposition, *Adv Mater* 19 (2007) 3425-3438.
- [206] B.J. O'Neill, D.H. Jackson, J. Lee, C. Canlas, P.C. Stair, C.L. Marshall, et al., Catalyst design with atomic layer deposition, *Acs Catalysis* 5 (2015) 1804-1825.
- [207] S. Skoog, J. Elam, R. Narayan, Atomic layer deposition: medical and biological applications, *International Materials Reviews* 58 (2013) 113-129.
- [208] T. Mayer, J. Elam, S. George, P. Kotula, R. Goeke, Atomic-layer deposition of wear-resistant coatings for microelectromechanical devices, *Appl. Phys. Lett.* 82 (2003) 2883-2885.
- [209] O.J. Kilbury, K.S. Barrett, X. Fu, J. Yin, D.S. Dinair, C.J. Gump, et al., Atomic layer deposition of solid lubricating coatings on particles, *Powder Technol* 221 (2012) 26-35.
- [210] A. Pereira, J.L. Palma, J.C. Denardin, J. Escrig, Temperature-dependent magnetic properties of Ni nanotubes synthesized by atomic layer deposition, *Nanotechnology* 27 (2016) 345709.
- [211] H. Kim, Atomic layer deposition of metal and nitride thin films: Current research efforts and applications for semiconductor device processing, *Journal of Vacuum Science & Technology B: Microelectronics and Nanometer Structures Processing, Measurement, and Phenomena* 21 (2003) 2231-2261.

- [212] M. Putkonen, A. Szeghalmi, E. Pippel, M. Knez, Atomic layer deposition of metal fluorides through oxide chemistry, *Journal of Materials Chemistry* 21 (2011) 14461-14465.
- [213] M. Ylilampi, T. Ranta-aho, Metal fluoride thin films prepared by atomic layer deposition, *J. Electrochem. Soc.* 141 (1994) 1278-1284.
- [214] N.P. Dasgupta, X. Meng, J.W. Elam, A.B. Martinson, Atomic layer deposition of metal sulfide materials, *Acc. Chem. Res.* 48 (2015) 341-348.
- [215] J. Hämäläinen, M. Ritala, M. Leskelä, Atomic layer deposition of noble metals and their oxides, *Chemistry of Materials* 26 (2013) 786-801.
- [216] B.S. Lim, A. Rahtu, R.G. Gordon, Atomic layer deposition of transition metals, *Nature materials* 2 (2003) 749-754.
- [217] C. Platzer-Björkman, T. Törndahl, D. Abou-Ras, J. Malmström, J. Kessler, L. Stolt, Zn (O, S) buffer layers by atomic layer deposition in Cu (In, Ga) Se₂ based thin film solar cells: band alignment and sulfur gradient, *J. Appl. Phys.* 100 (2006) 044506.
- [218] E. Thimsen, S.C. Riha, S.V. Baryshev, A.B. Martinson, J.W. Elam, M.J. Pellin, Atomic layer deposition of the quaternary chalcogenide Cu₂ZnSnS₄, *Chemistry of Materials* 24 (2012) 3188-3196.
- [219] C. Bugot, C. Broussillou, A. Sorba, L. Parissi, N. Schneider, D. Lincot, et al., Temperature effect during atomic layer deposition of zinc oxysulfide-Zn (O, S) buffer layers on Cu (In, Ga)(S, Se)₂ synthesized by co-evaporation and electro-deposition techniques, *Photovoltaic Specialist Conference (PVSC), 2015 IEEE 42nd. IEEE, (2015) 1-6.*
- [220] R.L. Puurunen, Surface chemistry of atomic layer deposition: A case study for the trimethylaluminum/water process, *J. Appl. Phys.* 97 (2005) 121301.
- [221] C. Reitz, B. Breitung, A. Schneider, D. Wang, M. von der Lehr, T. Leichtweiss, et al., Hierarchical carbon with high nitrogen doping level: A versatile anode and cathode host material for long-life lithium-ion and lithium-sulfur batteries, *ACS applied materials & interfaces* 8 (2016) 10274-10282.
- [222] J. Klaus, S. George, Atomic layer deposition of SiO₂ at room temperature using NH₃-catalyzed sequential surface reactions, *Surf. Sci.* 447 (2000) 81-90.
- [223] J.W. Klaus, O. Sneh, S.M. George, Growth of SiO₂ at room temperature with the use of catalyzed sequential half-reactions, *Science* 278 (1997) 1934-1936.
- [224] W. Gasser, Y. Uchida, M. Matsumura, Quasi-monolayer deposition of silicon dioxide, *Thin Solid Films* 250 (1994) 213-218.

- [225] Y. Luo, D. Slater, M. Han, J. Moryl, R. Osgood Jr, Low-temperature, chemically driven atomic-layer epitaxy: In situ monitored growth of CdS/ZnSe (100), *Appl. Phys. Lett.* 71 (1997) 3799-3801.
- [226] M. Groner, F. Fabreguette, J. Elam, S. George, Low-temperature Al₂O₃ atomic layer deposition, *Chemistry of Materials* 16 (2004) 639-645.
- [227] J. Niinistö, N. Petrova, M. Putkonen, L. Niinistö, K. Arstila, T. Sajavaara, Gadolinium oxide thin films by atomic layer deposition, *J. Cryst. Growth* 285 (2005) 191-200.
- [228] K. Kukli, M. Ritala, M. Leskelä, T. Sajavaara, J. Keinonen, D.C. Gilmer, et al., Atomic layer deposition of HfO₂ thin films and nanolayered HfO₂-Al₂O₃-Nb₂O₅ dielectrics, *J. Mater. Sci.: Mater. Electron.* 14 (2003) 361-367.
- [229] M. Yu, A. Wang, Y. Wang, C. Li, G. Shi, An alumina stabilized ZnO-graphene anode for lithium ion batteries via atomic layer deposition, *Nanoscale* 6 (2014) 11419-11424.
- [230] X. Meng, An overview of molecular layer deposition for organic and organic-inorganic hybrid materials: mechanisms, growth characteristics, and promising applications, *Journal of Materials Chemistry A* 5 (2017) 18326-18378.
- [231] A. Dillon, A. Ott, J. Way, S. George, Surface chemistry of Al₂O₃ deposition using Al(CH₃)₃ and H₂O in a binary reaction sequence, *Surf. Sci.* 322 (1995) 230-242.
- [232] S. George, A. Ott, J. Klaus, Surface chemistry for atomic layer growth, *J. Phys. Chem.* 100 (1996) 13121-13131.
- [233] A. Ott, J. Klaus, J. Johnson, S. George, Al₃O₃ thin film growth on Si (100) using binary reaction sequence chemistry, *Thin Solid Films* 292 (1997) 135-144.
- [234] H. Outokumpu, *Chemistry for Windows* program package, (2002).
- [235] J. Elam, M. Groner, S. George, Viscous flow reactor with quartz crystal microbalance for thin film growth by atomic layer deposition, *Rev. Sci. Instrum.* 73 (2002) 2981-2987.
- [236] J. Aarik, A. Aidla, H. Mändar, T. Uustare, Atomic layer deposition of titanium dioxide from TiCl₄ and H₂O: investigation of growth mechanism, *Appl. Surf. Sci.* 172 (2001) 148-158.
- [237] E.B. Yousfi, J. Fouache, D. Lincot, Study of atomic layer epitaxy of zinc oxide by in-situ quartz crystal microgravimetry, *Appl. Surf. Sci.* 153 (2000) 223-234.
- [238] P. Coon, P. Gupta, M.L. Wise, S. George, Adsorption and desorption kinetics for SiH₂Cl₂ on Si (111) 7×7, *Journal of Vacuum Science & Technology A: Vacuum, Surfaces, and Films* 10 (1992) 324-333.

- [239] B. Koehler, C. Mak, D. Arthur, P. Coon, S. George, Desorption kinetics of hydrogen and deuterium from Si (111) 7×7 studied using laser-induced thermal desorption, *J. Chem. Phys.* 89 (1988) 1709-1718.
- [240] P. Gupta, P. Coon, B. Koehler, S. George, Desorption product yields following Cl_2 adsorption on Si (111) 7×7 : Coverage and temperature dependence, *Surf. Sci.* 249 (1991) 92-104.
- [241] S.M. George, Atomic layer deposition: an overview, *Chem. Rev.* 110 (2010) 111-131.
- [242] H. Kim, C. Cabral Jr, C. Lavoie, S. Rossnagel, Diffusion barrier properties of transition metal thin films grown by plasma-enhanced atomic-layer deposition, *Journal of Vacuum Science & Technology B: Microelectronics and Nanometer Structures Processing, Measurement, and Phenomena* 20 (2002) 1321-1326.
- [243] S. Rossnagel, A. Sherman, F. Turner, Plasma-enhanced atomic layer deposition of Ta and Ti for interconnect diffusion barriers, *Journal of Vacuum Science & Technology B: Microelectronics and Nanometer Structures Processing, Measurement, and Phenomena* 18 (2000) 2016-2020.
- [244] T. Aaltonen, A. Rahtu, M. Ritala, M. Leskelä, Reaction mechanism studies on atomic layer deposition of ruthenium and platinum, *Electrochemical and solid-state letters* 6 (2003) C130-C133.
- [245] R. Grubbs, N. Steinmetz, S. George, Gas phase reaction products during tungsten atomic layer deposition using WF_6 and Si_2H_6 , *Journal of Vacuum Science & Technology B: Microelectronics and Nanometer Structures Processing, Measurement, and Phenomena* 22 (2004) 1811-1821.
- [246] J. Klaus, S. Ferro, S. George, Atomic layer deposition of tungsten using sequential surface chemistry with a sacrificial stripping reaction, *Thin Solid Films* 360 (2000) 145-153.
- [247] O. Sneh, M. Wise, A. Ott, L. Okada, S. George, Atomic layer growth of SiO_2 on Si (100) using SiCl_4 and H_2O in a binary reaction sequence, *Surf. Sci.* 334 (1995) 135-152.
- [248] J.C. Hackley, J.D. Demaree, T. Gougousi, Growth and interface of HfO_2 films on H-terminated Si from a TDMAH and H_2O atomic layer deposition process, *Journal of Vacuum Science & Technology A: Vacuum, Surfaces, and Films* 26 (2008) 1235-1240.
- [249] R.W. Johnson, A. Hultqvist, S.F. Bent, A brief review of atomic layer deposition: from fundamentals to applications, *Materials today* 17 (2014) 236-246.
- [250] J.S. Ponraj, G. Attolini, M. Bosi, Review on atomic layer deposition and applications of oxide thin films, *Critical Reviews in Solid State and Materials Sciences* 38 (2013) 203-233.

- [251] T. Tynell, M. Karppinen, Atomic layer deposition of ZnO: a review, *Semiconductor Science and Technology* 29 (2014) 043001.
- [252] E. Riyanto, E. Rijanto, B. Prawara, A review of atomic layer deposition for nanoscale devices, *Journal of Mechatronics, Electrical Power, and Vehicular Technology* 3 (2012) 65-72.
- [253] D. Nazarov, N. Bobrysheva, O. Osmolovskaya, M. Osmolovsky, V. Smirnov, Atomic layer deposition of tin dioxide nanofilms: A review, *Rev. Adv. Mater. Sci* 40 (2015) 262-275.
- [254] S.K. Panda, H. Shin, Step coverage in ALD, *Atomic layer deposition of nanostructured materials* (2011) 23-40.
- [255] T. Yoshimura, S. Tatsuura, W. Sotoyama, Polymer films formed with monolayer growth steps by molecular layer deposition, *Appl. Phys. Lett.* 59 (1991) 482-484.
- [256] T. Yoshimura, S. Tatsuura, W. Sotoyama, A. Matsuura, T. Hayano, Quantum wire and dot formation by chemical vapor deposition and molecular layer deposition of one-dimensional conjugated polymer, *Appl. Phys. Lett.* 60 (1992) 268-270.
- [257] A. Kim, M.A. Filler, S. Kim, S.F. Bent, Layer-by-layer growth on Ge (100) via spontaneous urea coupling reactions, *J. Am. Chem. Soc.* 127 (2005) 6123-6132.
- [258] N. Adamczyk, A. Dameron, S. George, Molecular layer deposition of poly (p-phenylene terephthalamide) films using terephthaloyl chloride and p-phenylenediamine, *Langmuir* 24 (2008) 2081-2089.
- [259] Y. Du, S. George, Molecular layer deposition of nylon 66 films examined using in situ FTIR spectroscopy, *The Journal of Physical Chemistry C* 111 (2007) 8509-8517.
- [260] M. Putkonen, J. Harjuoja, T. Sajavaara, L. Niinistö, Atomic layer deposition of polyimide thin films, *Journal of Materials Chemistry* 17 (2007) 664-669.
- [261] P.W. Loscutoff, H. Lee, S.F. Bent, Deposition of ultrathin polythiourea films by molecular layer deposition, *Chemistry of Materials* 22 (2010) 5563-5569.
- [262] J.S. Lee, Y.J. Lee, E.L. Tae, Y.S. Park, K.B. Yoon, Synthesis of zeolite as ordered multicrystal arrays, *Science* 301 (2003) 818-821.
- [263] T. Yoshimura, S. Ito, T. Nakayama, K. Matsumoto, Orientation-controlled molecule-by-molecule polymer wire growth by the carrier-gas-type organic chemical vapor deposition and the molecular layer deposition, *Appl. Phys. Lett.* 91 (2007) 033103.
- [264] T.V. Ivanova, P.S. Maydannik, D.C. Cameron, Molecular layer deposition of polyethylene terephthalate thin films, *Journal of Vacuum Science & Technology A: Vacuum, Surfaces, and Films* 30 (2012) 01A121.

- [265] S.E. Atanasov, M.D. Losego, B. Gong, E. Sachet, J. Maria, P.S. Williams, et al., Highly conductive and conformal poly (3, 4-ethylenedioxythiophene)(PEDOT) thin films via oxidative molecular layer deposition, *Chemistry of Materials* 26 (2014) 3471-3478.
- [266] D.H. Kim, S.E. Atanasov, P. Lemaire, K. Lee, G.N. Parsons, Platinum-free cathode for dye-sensitized solar cells using poly (3, 4-ethylenedioxythiophene)(PEDOT) formed via oxidative molecular layer deposition, *ACS applied materials & interfaces* 7 (2015) 3866-3870.
- [267] T. Miyamae, K. Tsukagoshi, O. Matsuoka, S. Yamamoto, H. Nozoye, Preparation of polyimide-polyamide random copolymer thin film by sequential vapor deposition polymerization, *Japanese journal of applied physics* 41 (2002) 746.
- [268] P.W. Loscutoff, H. Zhou, S.B. Clendenning, S.F. Bent, Formation of organic nanoscale laminates and blends by molecular layer deposition, *Acs Nano* 4 (2009) 331-341.
- [269] S.M. George, B.H. Lee, B. Yoon, A.I. Abdulagatov, R.A. Hall, Metalcones: Hybrid organic-inorganic films fabricated using atomic and molecular layer deposition techniques, *Journal of nanoscience and nanotechnology* 11 (2011) 7948-7955.
- [270] A.A. Dameron, D. Seghete, B. Burton, S. Davidson, A. Cavanagh, J. Bertrand, et al., Molecular layer deposition of alucone polymer films using trimethylaluminum and ethylene glycol, *Chemistry of Materials* 20 (2008) 3315-3326.
- [271] B. Yoon, J.L. O'Patchen, D. Seghete, A.S. Cavanagh, S.M. George, Molecular Layer Deposition of Hybrid Organic-Inorganic Polymer Films using Diethylzinc and Ethylene Glycol, *Chemical Vapor Deposition* 15 (2009) 112-121.
- [272] A.I. Abdulagatov, R.A. Hall, J.L. Sutherland, B.H. Lee, A.S. Cavanagh, S.M. George, Molecular layer deposition of titanicone films using $TiCl_4$ and ethylene glycol or glycerol: growth and properties, *Chemistry of Materials* 24 (2012) 2854-2863.
- [273] B.H. Lee, V.R. Anderson, S.M. George, Growth and properties of hafnicone and HfO_2 /hafnicone nanolaminate and alloy films using molecular layer deposition techniques, *ACS applied materials & interfaces* 6 (2014) 16880-16887.
- [274] B. Yoon, B.H. Lee, S.M. George, Highly conductive and transparent hybrid organic-inorganic zincone thin films using atomic and molecular layer deposition, *The Journal of Physical Chemistry C* 116 (2012) 24784-24791.
- [275] K. Van de Kerckhove, F. Mattelaer, J. Dendooven, C. Detavernier, Molecular layer deposition of "vanadicone", a vanadium-based hybrid material, as an electrode for lithium-ion batteries, *Dalton Transactions* 46 (2017) 4542-4553.
- [276] C. Kao, J. Yoo, Y. Min, A.J. Epstein, Molecular layer deposition of an organic-based magnetic semiconducting laminate, *ACS applied materials & interfaces* 4 (2012) 137-141.

- [277] C. Kao, B. Li, Y. Lu, J. Yoo, A.J. Epstein, Thin films of organic-based magnetic materials of vanadium and cobalt tetracyanoethylene by molecular layer deposition, *Journal of Materials Chemistry C* 2 (2014) 6171-6176.
- [278] O. Nilsen, K. Klepper, H. Nielsen, H. Fjellvåg, Deposition of organic-inorganic hybrid materials by atomic layer deposition, *Ecs Transactions* 16 (2008) 3-14.
- [279] O. Nilsen, K.R. Haug, T. Finstad, H. Fjellvåg, Molecular hybrid structures by atomic layer deposition-Deposition of Alq_3 , Znq_2 and Tiq_4 ($q=$ 8-hydroxyquinoline), *Chemical Vapor Deposition* 19 (2013) 174-179.
- [280] L.D. Salmi, M.J. Heikkilä, E. Puukilainen, T. Sajavaara, D. Grosso, M. Ritala, Studies on atomic layer deposition of MOF-5 thin films, *Microporous and Mesoporous Materials* 182 (2013) 147-154.
- [281] L.D. Salmi, M.J. Heikkilä, M. Vehkamäki, E. Puukilainen, M. Ritala, T. Sajavaara, Studies on atomic layer deposition of IRMOF-8 thin films, *Journal of Vacuum Science & Technology A: Vacuum, Surfaces, and Films* 33 (2015) 01A121.
- [282] E. Ahvenniemi, M. Karppinen, Atomic/molecular layer deposition: a direct gas-phase route to crystalline metal-organic framework thin films, *Chemical Communications* 52 (2016) 1139-1142.
- [283] M. Nisula, M. Karppinen, Atomic/molecular layer deposition of lithium terephthalate thin films as high rate capability Li-ion battery anodes, *Nano letters* 16 (2016) 1276-1281.
- [284] D. Sarkar, S. Ishchuk, D.H. Taffa, N. Kaynan, B.A. Berke, T. Bendikov, et al., Oxygen-deficient titania with adjustable band positions and defects; molecular layer deposition of hybrid organic-inorganic thin films as precursors for enhanced photocatalysis, *The Journal of Physical Chemistry C* 120 (2016) 3853-3862.
- [285] H. Zhou, S.F. Bent, Fabrication of organic interfacial layers by molecular layer deposition: Present status and future opportunities, *Journal of Vacuum Science & Technology A: Vacuum, Surfaces, and Films* 31 (2013) 040801.
- [286] C. Ban, S.M. George, Molecular layer deposition for surface modification of lithium-ion battery electrodes, *Advanced Materials Interfaces* 3 (2016) 1600762.
- [287] Y. Zhao, X. Sun, Molecular layer deposition for energy conversion and storage, *ACS Energy Letters* 3 (2018) 899-914.
- [288] B.H. Lee, B. Yoon, A.I. Abdulagatov, R.A. Hall, S.M. George, Growth and properties of hybrid organic-inorganic metalcone films using molecular layer deposition techniques, *Advanced Functional Materials* 23 (2013) 532-546.

- [289] B. Gong, J.C. Spagnola, G.N. Parsons, Hydrophilic mechanical buffer layers and stable hydrophilic finishes on polydimethylsiloxane using combined sequential vapor infiltration and atomic/molecular layer deposition, *Journal of Vacuum Science & Technology A: Vacuum, Surfaces, and Films* 30 (2012) 01A156.
- [290] P. Sundberg, M. Karppinen, Organic and inorganic-organic thin film structures by molecular layer deposition: A review, *Beilstein J. Nanotechnol* 5 (2014) 1104-1136.
- [291] K. Gregorczyk, M. Knez, Hybrid nanomaterials through molecular and atomic layer deposition: Top down, bottom up, and in-between approaches to new materials, *Progress in Materials Science* 75 (2016) 1-37.
- [292] E. Ahvenniemi, M. Karppinen, ALD/MLD processes for Mn and Co based hybrid thin films, *Dalton Transactions* 45 (2016) 10730-10735.
- [293] D. Choudhury, S.K. Sarkar, N. Mahuli, Molecular layer deposition of alucone films using trimethylaluminum and hydroquinone, *Journal of Vacuum Science & Technology A: Vacuum, Surfaces, and Films* 33 (2015) 01A115.
- [294] S.M. George, B. Yoon, A.A. Dameron, Surface chemistry for molecular layer deposition of organic and hybrid organic-inorganic polymers, *Acc. Chem. Res.* 42 (2009) 498-508.
- [295] B.H. Lee, B. Yoon, V.R. Anderson, S.M. George, Alucone alloys with tunable properties using alucone molecular layer deposition and Al₂O₃ atomic layer deposition, *The Journal of Physical Chemistry C* 116 (2012) 3250-3257.
- [296] B.H. Lee, V.R. Anderson, S.M. George, Metalcone and metalcone/metal oxide alloys grown using atomic and molecular layer deposition, *ECS Transactions* 41 (2011) 131-138.
- [297] L. Ghazaryan, E. Kley, A. Tünnermann, A. Viorica Szeghalmi, Stability and annealing of alucones and alucone alloys, *Journal of Vacuum Science & Technology A: Vacuum, Surfaces, and Films* 31 (2013) 01A149.
- [298] J. Cai, Q. Sun, X. Meng, Novel nanostructured materials by atomic and molecular layer deposition, *AIMS Materials Science* 5 (2018) 957-999.
- [299] X. Liang, A.W. Weimer, An overview of highly porous oxide films with tunable thickness prepared by molecular layer deposition, *Current Opinion in Solid State and Materials Science* 19 (2015) 115-125.
- [300] S. De Gendt, S. Bent, A. Delabie, J. Elam, S. Kang, O. van der Straten, et al., Atomic layer deposition applications 5, *ECS Transactions* 25 (2009).
- [301] B. Yoon, D. Seghete, A.S. Cavanagh, S.M. George, Molecular layer deposition of hybrid organic-inorganic alucone polymer films using a three-step ABC reaction sequence, *Chemistry of Materials* 21 (2009) 5365-5374.

- [302] A. Sood, P. Sundberg, M. Karppinen, ALD/MLD of novel layer-engineered Zn-based inorganic-organic hybrid thin films using heterobifunctional 4-aminophenol as an organic precursor, Dalton Transactions 42 (2013) 3869-3875.
- [303] Q. Sun, K.C. Lau, D. Geng, X. Meng, Atomic and molecular layer deposition for superior lithium-sulfur batteries: Strategies, performance, and mechanisms, Batteries & Supercaps 1 (2018) 41-68.

2 GROWTH PROPERTIES OF DIFFERENT COATINGS

2.1 Materials

Glycerol (GL), Titanium isopropoxide (TTIP), H₂O were purchased from Sigma Aldrich. TMA and DEZ were bought from Strem Chemicals, Inc. N-doped graphene (NGS) was purchase from ACS Materials LLC. These chemicals were summarized in Table 1.

Table 1. Summary of needed chemicals (1)

Chemicals	CAS#	Formula	Molecular weight	Flash point	Melting point	Boiling point	Source
Glycerol (GL)	56-81-5	500 mL (one bottle)	0	1	0 °C	/	Sigma aldrich
Deionized water	7732-18-5	/	18.02	/	0 °C	100 °C	Sigma aldrich
N-doped graphene (NGS)	7782-42-5 (graphite)	C	12.01 g/mol	/	3650 °C	/	ACS material LLC
Trimethylaluminum (TMA)	75-24-1	C ₃ H ₉ Al	144.18 g/mol	-17°C	15.4 °C	127 °C	Strem chemicals. INC
Diethylzinc (DEZ)	557-20-0	(C ₂ H ₅) ₂ Zn	123.51 g/mol	-18°C	-28 °C	124 °C	Strem chemicals. INC
Titanium isopropoxide (TTIP)	546-68-9	Ti[OCH(CH ₃) ₂] ₄	284.22 g/mol	45 °C	14~17 °C	232 °C	Sigma aldrich

2.2 ALD/MLD Deposition Parameters

Different coatings (Al₂O₃, ZnO, TiO₂, AlGL and ZnGL) were deposited on Si wafer and their growth properties were investigated using quartz crystal microbalance (QCM) method. The parameters of ALD were summarized in Table 2. These coatings were deposited by the

Savannah S200 atomic layer deposition systems (Ultratech/Cambridge nanotech) as shown in Figure 1.

Table 2. Deposition parameters of different coatings

Method	Coatings	Precursors	Deposition conditions
ALD	Al ₂ O ₃	Trimethylaluminum (TMA), H ₂ O	TMA-purge-H ₂ O-purge (0.015-15-0.015-15 s), 50 °C
			TMA-purge-H ₂ O-purge (0.015-10-0.015-10 s), 75 °C
			TMA-purge-H ₂ O-purge (0.015-5-0.015-5 s), 100 °C
			TMA-purge-H ₂ O-purge (0.015-5-0.015-5 s), 150 °C
			TMA-purge-H ₂ O-purge (1-5-1-5 s), 150 °C
	TiO ₂	titanium tetraisopropoxide (TTIP), H ₂ O	TTIP-purge-H ₂ O-purge (1-5-1-5 s), 150 °C
ZnO	Diethylzinc (DEZ), H ₂ O	DEZ-purge-H ₂ O-purge (1-5-1-5 s), 150 °C	
MLD	AlGL	TMA, glycerol (GL)	TMA-purge-GL-purge (0.015-20-2-60 s), 50°C
			TMA-purge-GL-purge (0.015-15-2-40 s), 75°C
			TMA-purge-GL-purge (0.015-60-2-60 s), 75°C
	ZnGL	DEZ, GL	DEZ-purge-GL-purge (0.015-20-2-60 s), 50 °C
			DEZ-purge-GL-purge (0.015-15-2-40 s), 75 °C



Figure 1. ALD/MLD system

2.3 ALD Coatings

2.3.1 Al₂O₃ film growth

Al₂O₃ was deposited on Si wafer by ALD using TMA and H₂O as precursors. QCM was employed to investigate the growth property of ALD-Al₂O₃. According to the mass gain of three consecutive ALD cycles, we could find that using the recipe of (TMA-purge-H₂O-purge, 0.015-15-0.015-15 s, 50 °C) leads to mass gains of 37, 36 and 35 ng, respectively. Correspondingly, TMA contributed 23, 24 and 22 ng, while H₂O contributed 14, 12 and 13 ng (Figure 2(b)). Introducing the recipe of (TMA-purge-H₂O-purge, 0.015-10-0.015-10 s, 75 °C) generated mass gains of 30, 35 and 36 ng. TMA gave mass gains of 21, 27 and 19 ng. H₂O contributed 9, 8 and 7 ng (Figure 2(e)). Employing the recipe of (TMA-purge-H₂O-purge, 0.015-5-0.015-5 s, 100 °C) resulted in mass gains of 24, 25 and 24 ng (Figure 2(h)). In this case, the growth rate was 1 Å/cycle (Figure 2(i)). When Al₂O₃ was deposited at a higher temperature of 150 °C, the recipe of (TMA-purge-H₂O-purge, 0.015-5-0.015-5 s) gave mass gains of 40, 39 and 38 ng (Figure 2(k)),

while the recipe of (TMA-purge-H₂O-purge, 1-5-1-5 s) led to mass gains of 49, 49 and 48 ng (Figure 2(n)). Additionally, mass gain of the whole ALD-Al₂O₃ process using different recipes and corresponding film thickness curves were shown in Figure 2.

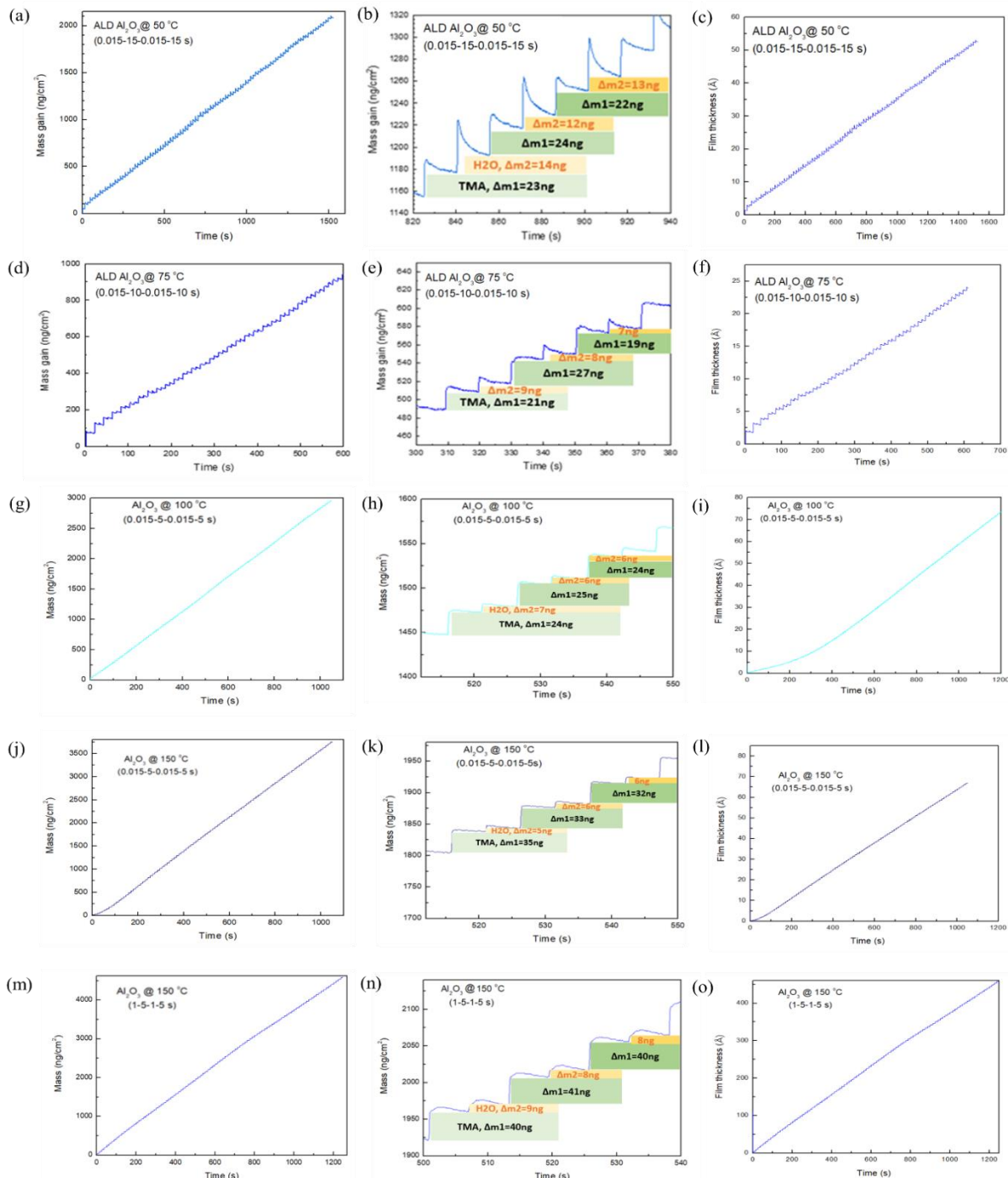


Figure 2. (a) Mass gain of Al_2O_3 deposited at 50 °C using the recipe of (TMA-purge-H₂O-purge, 0.015-15-0.015-15 s); (b) Three consequential cycles of Al_2O_3 deposited at 50 °C using the recipe of (TMA-purge-H₂O-purge, 0.015-15-0.015-15 s); (c) Film thickness of Al_2O_3 deposited at 50 °C using the recipe of (TMA-purge-H₂O-purge, 0.015-15-0.015-15 s); (d) Mass gain of Al_2O_3 deposited at 75 °C using the recipe of (TMA-purge-H₂O-purge, 0.015-10-0.015-10 s); (e) Three consequential cycles of Al_2O_3 deposited at 75 °C using the recipe of (TMA-purge-H₂O-purge, 0.015-10-0.015-10 s); (f) Film thickness of Al_2O_3 deposited at 75 °C

using the recipe of (TMA-purge-H₂O-purge, 0.015-10-0.015-10 s); (g) Mass gain of Al₂O₃ deposited at 100 °C using the recipe of (TMA-purge-H₂O-purge, 0.015-5-0.015-5 s); (h) Three consequential cycles of Al₂O₃ deposited at 100 °C using the recipe of (TMA-purge-H₂O-purge, 0.015-5-0.015-5 s); (i) Film thickness of Al₂O₃ deposited at 100 °C using the recipe of (TMA-purge-H₂O-purge, 0.015-5-0.015-5 s); (j) Mass gain of Al₂O₃ deposited at 150 °C using the recipe of (TMA-purge-H₂O-purge, 0.015-5-0.015-5 s); (k) Three consequential cycles of Al₂O₃ deposited at 150 °C using the recipe of (TMA-purge-H₂O-purge, 0.015-5-0.015-5 s); (l) Film thickness of Al₂O₃ deposited at 150 °C using the recipe of (TMA-purge-H₂O-purge, 0.015-5-0.015-5 s); (m) Mass gain of Al₂O₃ deposited at 150 °C using the recipe of (TMA-purge-H₂O-purge, 1-5-1-5 s); (n) Three consequential cycles of Al₂O₃ deposited at 150 °C using the recipe of (TMA-purge-H₂O-purge, 1-5-1-5 s); (o) Film thickness of Al₂O₃ deposited at 150 °C using the recipe of (TMA-purge-H₂O-purge, 1-5-1-5 s).

Al₂O₃ was deposited on NGS at 100 °C by ALD using TMA and H₂O as precursors. 1x ALD-Al₂O₃ on NGS consisted of a TMA dosing--ten times of (pulse 0.2s-stop valve closed-wait 2s-stop valve open-wait 2s) followed by H₂O dosing--ten times of (pulse 0.2s-stop valve closed-wait 2s-stop valve open-wait 2s) as shown in Figure 3(e). SEM picture indicated that bare NGS exhibited a wrinkled and smooth morphology (Figure 3(a)), while small particles of Al₂O₃ can be detected for ALD-Al₂O₃ coated NGS, especially for 3x and 5x ALD-Al₂O₃ coated NGS samples (Figure 3 (c)(d)), indicating successful deposition of Al₂O₃ by ALD. Percentage of ALD-Al₂O₃ in total mass of Al₂O₃+NGS was calculated and the result was shown in Table 3. The percentage of ALD-Al₂O₃ increased from 1.66 % to 45.76 % as the ALD cycles grew from 1x to 10x.

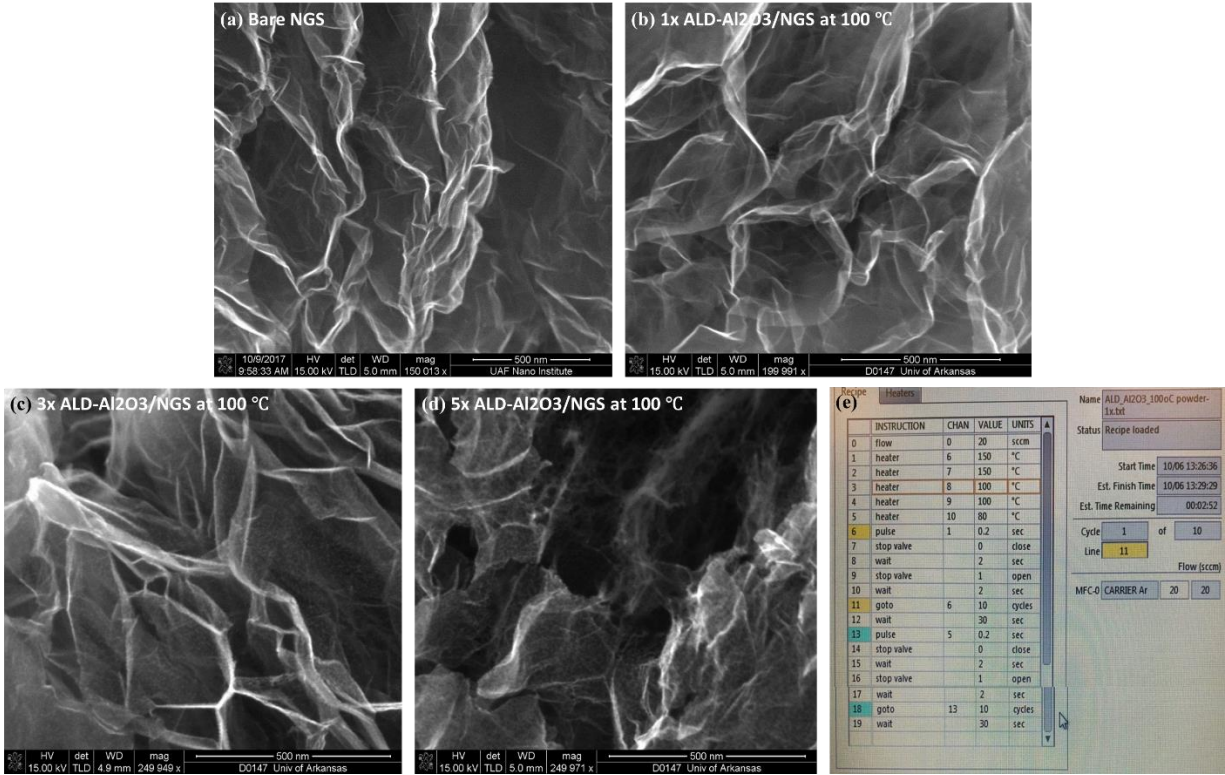


Figure 3. SEM pictures of (a) bare NGS and ALD-Al₂O₃ deposited on N-doped single layer graphene (NGS) at 100 °C using (b) 1x, (c) 3x, and (d) 5x ALD cycles. (e) The recipe of 1x ALD-Al₂O₃ on NGS is as the following: TMA dosing--ten times of (pulse 0.2s-stop valve closed-wait 2s-stop valve open-wait 2s) and H₂O dosing--ten times of (pulse 0.2s-stop valve closed-wait 2s-stop valve open-wait 2s).

Table 3. Summary of percentage of ALD-Al₂O₃ in total mass of Al₂O₃+NGS

	ALD Cycles	before coating m ₁ (mg)	after coating m ₂ (mg)	m ₂ -m ₁ (mg)	(m ₂ -m ₁)/m ₂ (%)
Al ₂ O ₃ on NGS	1x	19.50	19.83	0.33	1.66
	3x	21.00	23.78	2.78	11.69
	5x	20.30	27.45	8.15	28.65
	10x	20.00	36.87	16.87	45.76

2.3.2 TiO₂ film growth

TTIP and H₂O were employed as precursors to deposit TiO₂ on Si wafer at 150 °C using the recipe of (TTIP-purge-H₂O-purge, 1-5-1-5 s). QCM was utilized to investigate the growth

property of ALD-TiO₂. We could observe that TTIP contributed a mass gain of 28, 27 and 27 ng for the three consecutive cycles respectively. Correspondingly, the introduction of H₂O gave a mass gain of 13, 14 and 15 ng (Figure 4(b)). Therefore, the mass gain for the three consecutive ALD-TiO₂ cycles were calculated to be 15, 13 and 12 ng. Film thickness was given in Figure 4(c).

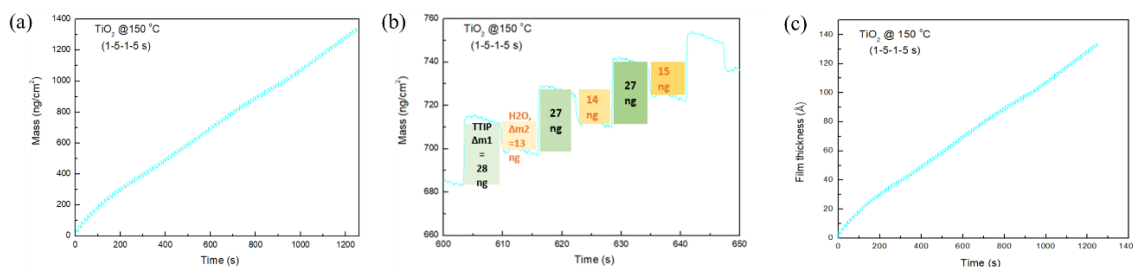


Figure 4. (a) Mass gain of TiO₂ deposited at 150 °C using the recipe of (TTIP-purge-H₂O-purge, 1-5-1-5 s); (b) Three consequential cycles of TiO₂ deposited at 150 °C using the recipe of (TTIP-purge-H₂O-purge, 1-5-1-5 s); (c) Film thickness of TiO₂ deposited at 150 °C using the recipe of (TTIP-purge-H₂O-purge, 1-5-1-5 s).

TiO₂ was deposited on NGS at 100 °C by ALD using TTIP and H₂O as precursors. 1x ALD-TiO₂ on NGS stood for a TMA dosing--ten times of (pulse 0.2s-stop valve closed-wait 2s-stop valve open-wait 2s) followed by H₂O dosing--ten times of (pulse 0.2s-stop valve closed-wait 2s-stop valve open-wait 2s) as shown in Figure 5(f). 3x, 15x, 30x and 60x ALD cycles were performed. No obvious morphological difference was observed between bare NGS and ALD-TiO₂ coated NGS (Figure 5(a)-(e)). Percentages of ALD-TiO₂ were 4.2 wt%, 26.21 wt%, 55.89 wt%, and 80.21 wt% for 3x, 15x, 30x and 60x ALD-TiO₂ coated NGS samples (Table 4).

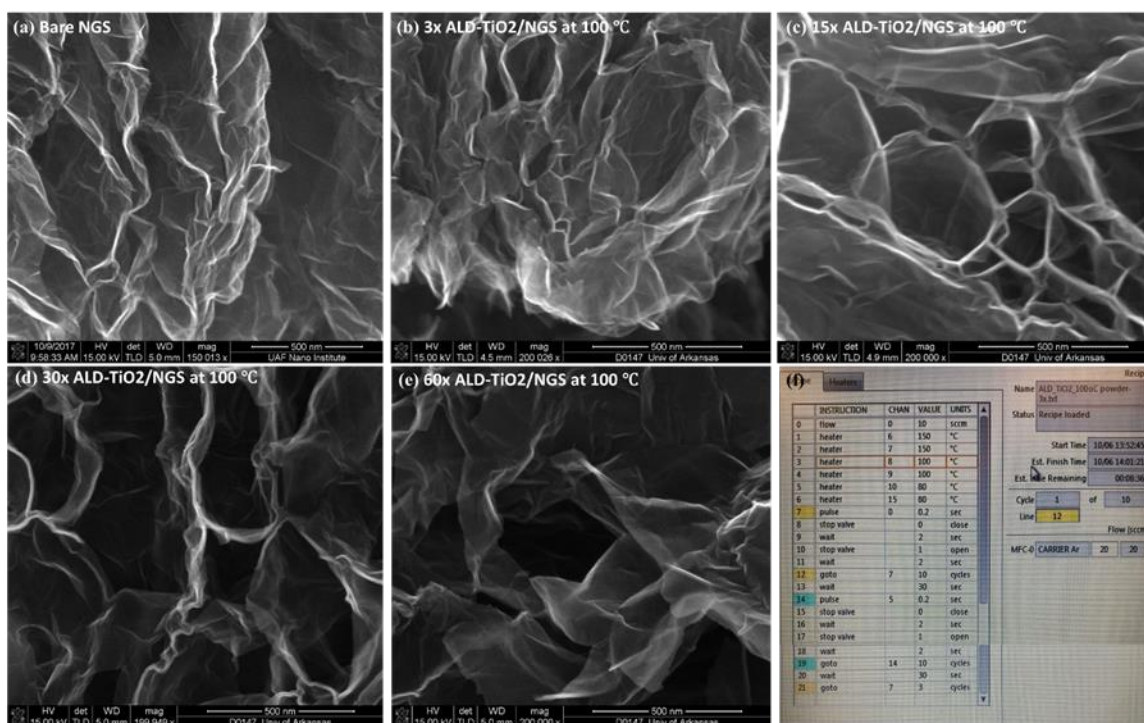


Figure 5. SEM pictures of (a) bare NGS and ALD-TiO₂ deposited on N-doped single layer graphene (NGS) at 100 °C using (b) 3x, (c) 15x, (d) 30x, and (e) 60x ALD cycles. (f) The recipe of 3x ALD-TiO₂ on NGS is as the following: 1x cycle is composed of TTIP dosing--ten times of (pulse 0.2s-stop valve closed-wait 2s-stop valve open-wait 2s) and H₂O dosing--ten times of (pulse 0.2s-stop valve closed-wait 2s-stop valve open-wait 2s), repeating the 1x cycles three times we get the recipe of 3x ALD-TiO₂ on NGS.

Table 4. Summary of percentage of ALD-TiO₂ in total mass of TiO₂+NGS

	ALD Cycles	before coating m_1 (mg)	after coating m_2 (mg)	$m_2 - m_1$ (mg)	$(m_2 - m_1)/m_2$ (%)
TiO ₂ on NGS	3x	23.10	24.11	1.01	4.20
	15x	23.40	31.71	8.31	26.21
	30x	20.60	46.70	26.10	55.89
	60x	23.20	117.23	94.03	80.21

2.3.3 ZnO film growth

ZnO was deposited on Si wafer by ALD at 150 °C using the recipe of (DEZ-purge-H₂O-purge, 1-5-1-5 s). Growth property of ALD-ZnO was measured by QCM. Figure 6(b) demonstrated that in

the three continuous ALD cycles, DEZ contributed mass gain of 125, 124 and 125 ng, while H₂O gave the mass gain of 4, 5 and 4 ng. Therefore, the mass gain of the three continuous cycles was 129, 129 and 129 ng. Film thickness of ZnO was shown as Figure 6(c).

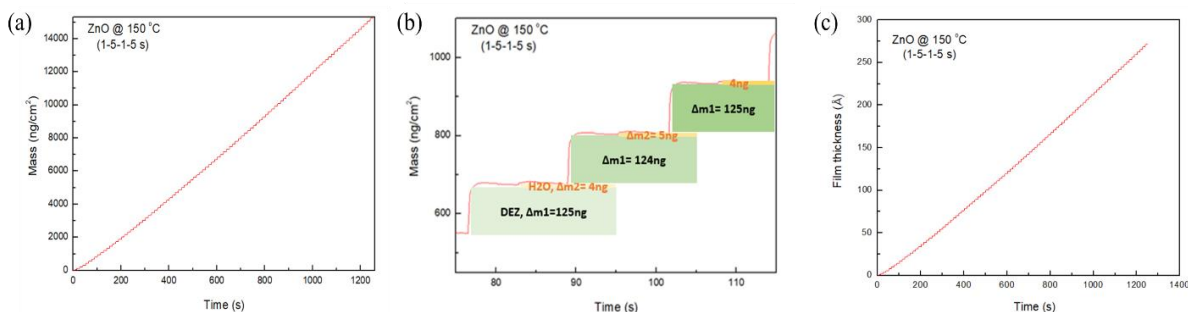


Figure 6. (a) Mass gain of ZnO deposited at 150 °C using the recipe of (DEZ-purge-H₂O-purge, 1-5-1-5 s); (b) Three consequential cycles of ZnO deposited at 150 °C using the recipe of (DEZ-purge-H₂O-purge, 1-5-1-5 s); (c) Film thickness of ZnO deposited at 150 °C using the recipe of (DEZ-purge-H₂O-purge, 1-5-1-5 s).

ZnO was deposited on NGS at 100 °C using precursors of DEZ and H₂O. The recipe of depositing 1x ALD-ZnO on NGS was composed of DEZ dosing--ten times of (pulse 0.2s-stop valve closed-wait 2s-stop valve open-wait 2s), followed by H₂O dosing--ten times of (pulse 0.2s-stop valve closed-wait 2s-stop valve open-wait 2s) as indicated by Figure 7(f). Different cycles of 1x, 5x, 10x, and 20x ALD cycles were conducted. SEM results indicated that with the increasing ALD cycles, more ZnO particles on NGS could be observed (Figure 7(b)-(e)). The thicknesses of ZnO layer tested by SEM were 0.57, 2.06, 3.89 and 5.61 nm for 1x, 5x, 10x, and 20x ALD-ZnO coated NGS samples, which agreed well with the calculated thickness based on growth rate (0.4508, 2.0178, 3.8329 and 5.4503 nm for 1x, 5x, 10x and 20x ALD-ZnO samples) (Table 5). According to Table 6, percentages of ALD-ZnO were 6.76 wt%, 30.27 wt%, 57.49 wt%, and 81.75wt% for 1x, 5x, 10x and 20x ALD-ZnO coated NGS samples, respectively.

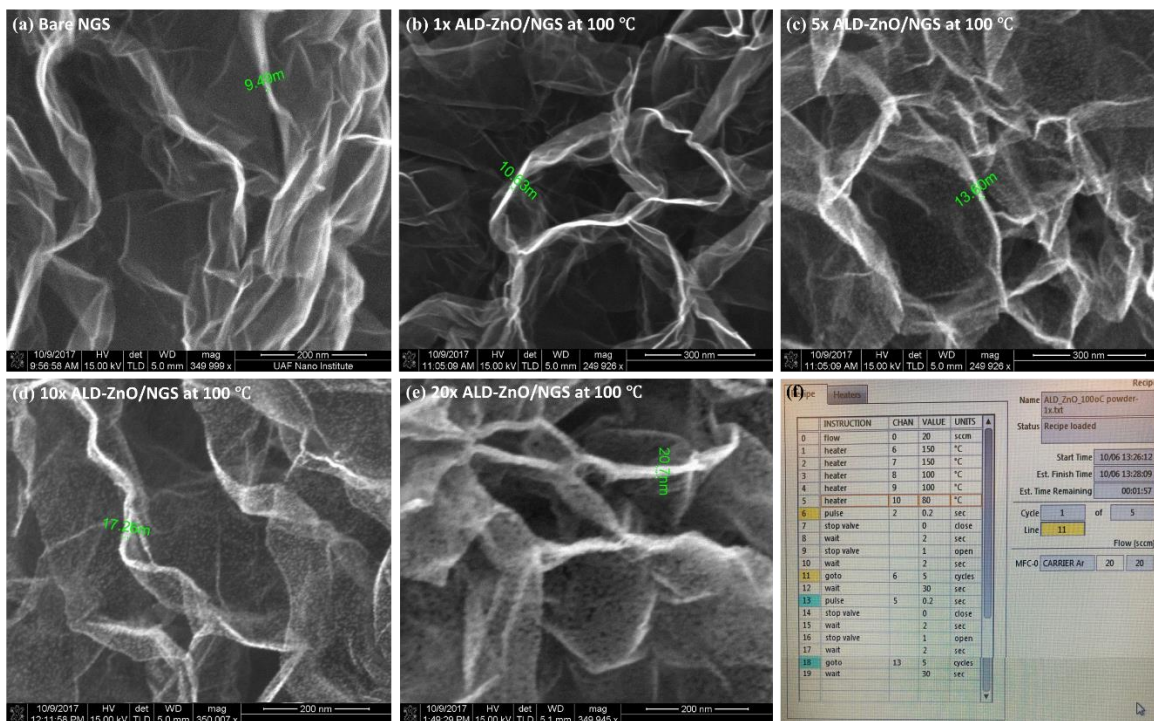


Figure 7. SEM pictures of (a) bare NGS and ALD-ZnO deposited on N-doped single layer graphene (NGS) at 100 °C using (b) 1x, (c) 5x, (d) 10x, and (e) 20x ALD cycles. (f) The recipe of 1x ALD-ZnO on NGS is as the following: DEZ dosing--ten times of (pulse 0.2s-stop valve closed-wait 2s-stop valve open-wait 2s) and H₂O dosing--ten times of (pulse 0.2s-stop valve closed-wait 2s-stop valve open-wait 2s).

Table 5. Summary of thickness of ALD-ZnO film

	ALD Cycles	Calculated ALD-ZnO layer Thickness (nm) based on growth rate	SEM Tested ALD-ZnO/NGS Thickness (nm)	Tested ALD-ZnO thickness (nm)
ZnO on NGS	0x	/	9.49	/
	1x	0.4508	10.63	0.57
	5x	2.0178	13.60	2.06
	10x	3.8329	17.26	3.89
	20x	5.4503	20.7	5.61

Table 6. Summary of percentage of ALD-ZnO in total mass of ZnO+NGS

	ALD Cycles	before coating m_1 (mg)	after coating m_2 (mg)	$m_2 - m_1$ (mg)	$(m_2 - m_1)/m_2$ (%)
ZnO on NGS	1x	23.30	24.99	1.69	6.76
	5x	23.80	34.13	10.33	30.27
	10x	23.60	55.52	31.92	57.49
	20x	20.60	112.90	92.30	81.75

Additionally, ZnO was deposited on NGS by ALD at different temperatures of 80, 100, 150, 200 and 250 °C using the recipe of (DEZ-purge-H₂O-purge, 0.015-5-0.015-5 s). Morphology of the samples deposited using 100, 200, 300 and 400 ALD cycles was investigated. And SEM results were given in Figure 8. We could summary that at same temperature, larger ALD cycles led to a denser morphology. Besides, rice-like surface could be detected for the samples deposited at 80-150 °C. The morphology of samples deposited at 200 °C looked like diamond and rice. Samples deposited at 250 °C performed a diamond-like surface.

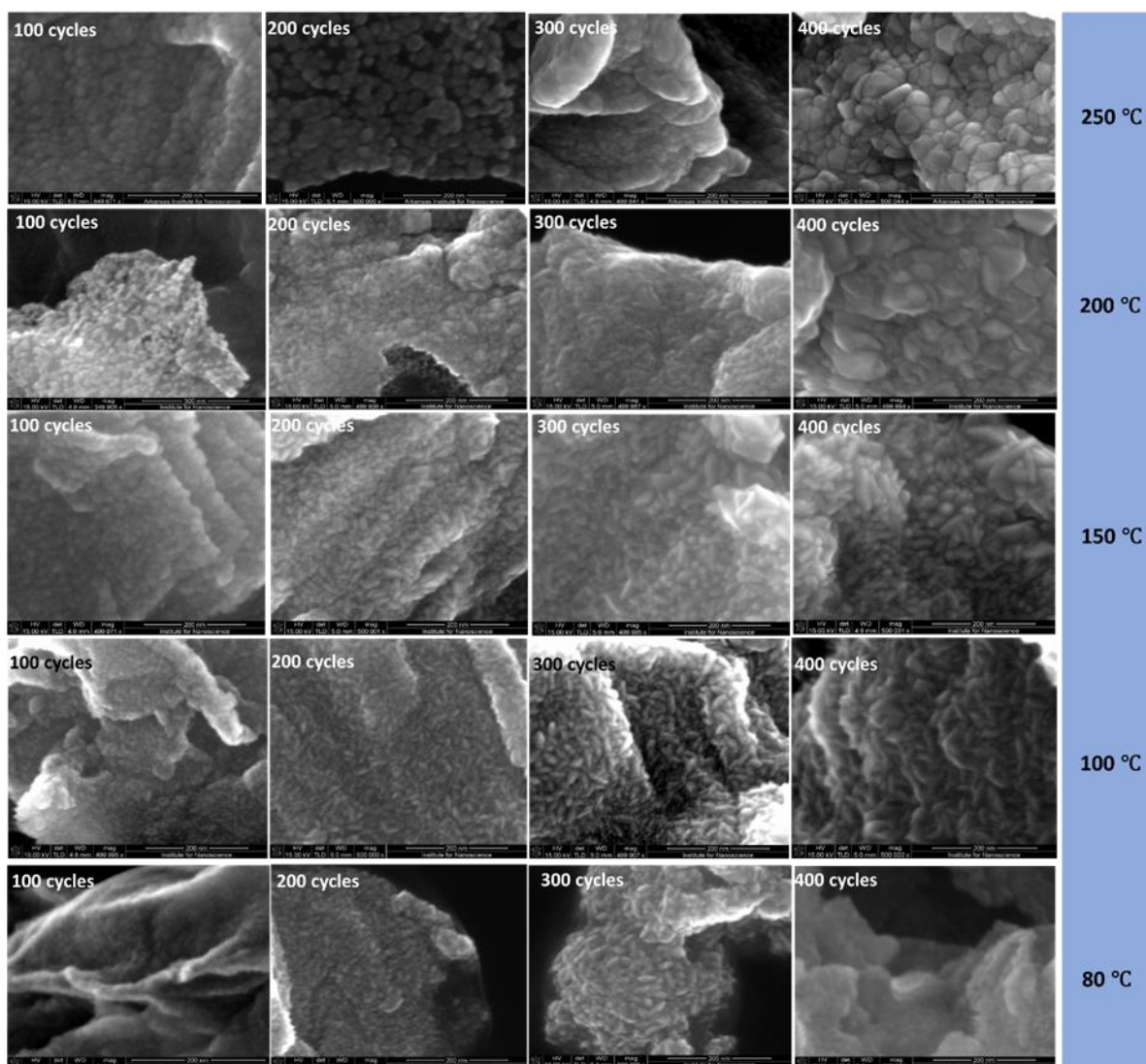


Figure 8. SEM pictures of ZnO deposited on N-doped single layer graphene (NGS) at 250, 200, 150, 100 and 80 °C using 100, 200, 300, 400 ALD cycles. The recipe is (DEZ-purge-H₂O-purge, 0.015-5-0.015-5 s), the growth rate is 0.7-2.5 Å/cycle. (Samples were prepared by Jiyu Cai. SEM pictures were taken by him and me.)

2.4 MLD Coatings

2.4.1 AIGL film growth

AIGL films were deposited on Si wafer by MLD and their growth property was studied by QCM.

The mass gain curve of three consecutive cycles was extracted from the stable mass gain curve of the whole MLD process. When using the recipe of TMA-purge-GL-purge (0.015-20-2-60 s,

50 °C), TMA generated mass gains of 40, 49 and 49 ng, while GL contributed 67, 72 and 84 ng for the three continuous cycles (Figure 9(b)). When using the recipe of (TMA-purge-GL-purge, 0.015-15-2-40 s, 75 °C), we calculated that the mass gains of TMA for the three consecutive cycles were 37, 39, and 48 ng. And the mass gains of GL were 54, 50 and 67 ng. When the recipe of (TMA-purge-GL-purge, 0.015-60-2-60 s, 75 °C) was employed, we found that for the three continuous cycles, TMA gave mass gains of 48, 44 and 30 ng, while GL contributed 52, 50 and 40 ng (Figure 9(d)).

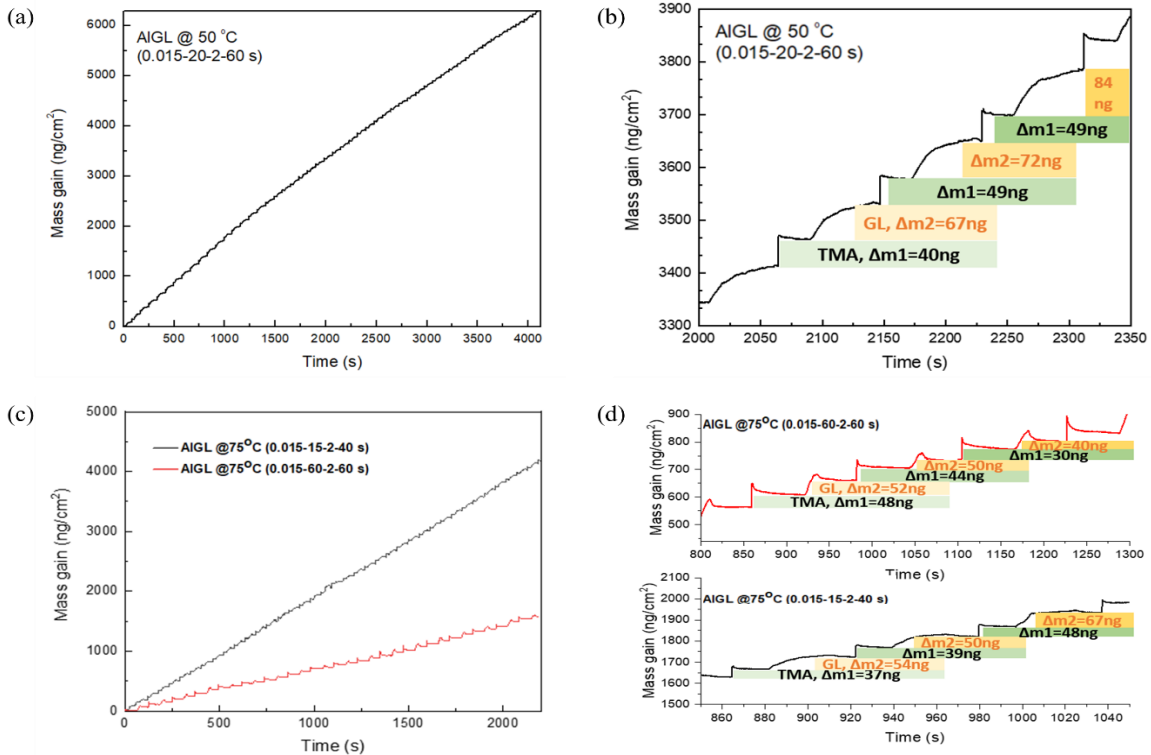


Figure 9. (a) Mass gain of AIGL deposited at 50 °C using the recipe of (TMA-purge-GL-purge, 0.015-20-2-60 s); (b) Three consequential cycles of AIGI deposited at 50 °C using the recipe of (TMA-purge-GL-purge, 0.015-20-2-60 s); (c) Mass gain of AIGL deposited at 75 °C using the recipe of (TMA-purge-GL-purge, 0.015-15-2-40 s) and (TMA-purge-GL-purge, 0.015-60-2-60 s); (d) Three consequential cycles of AIGI deposited at 75 °C using the recipe of (TMA-purge-GL-purge, 0.015-15-2-40 s) and (TMA-purge-GL-purge, 0.015-60-2-60 s).

2.4.2 ZnGL film growth

ZnGL was deposited on Si wafer by MLD. QCM was used to investigate their growth property. Based on the mass gain curve of three consecutive cycles, for the recipe of (DEZ-purge-GL-purge, 0.015-20-2-60 s, 50 °C), we calculated that DEZ contributed mass gains of 38, 35 and 34 ng and GL generated mass gains of 24, 23 and 23 ng (Figure 10(b)). For the recipe of (DEZ-purge-GL-purge, 0.015-15-2-40 s, 75 °C), we found that the mass gains of TMA were 49, 59 and 45 ng and that of GL were 41, 37 and 35 ng (Figure 10(d)).

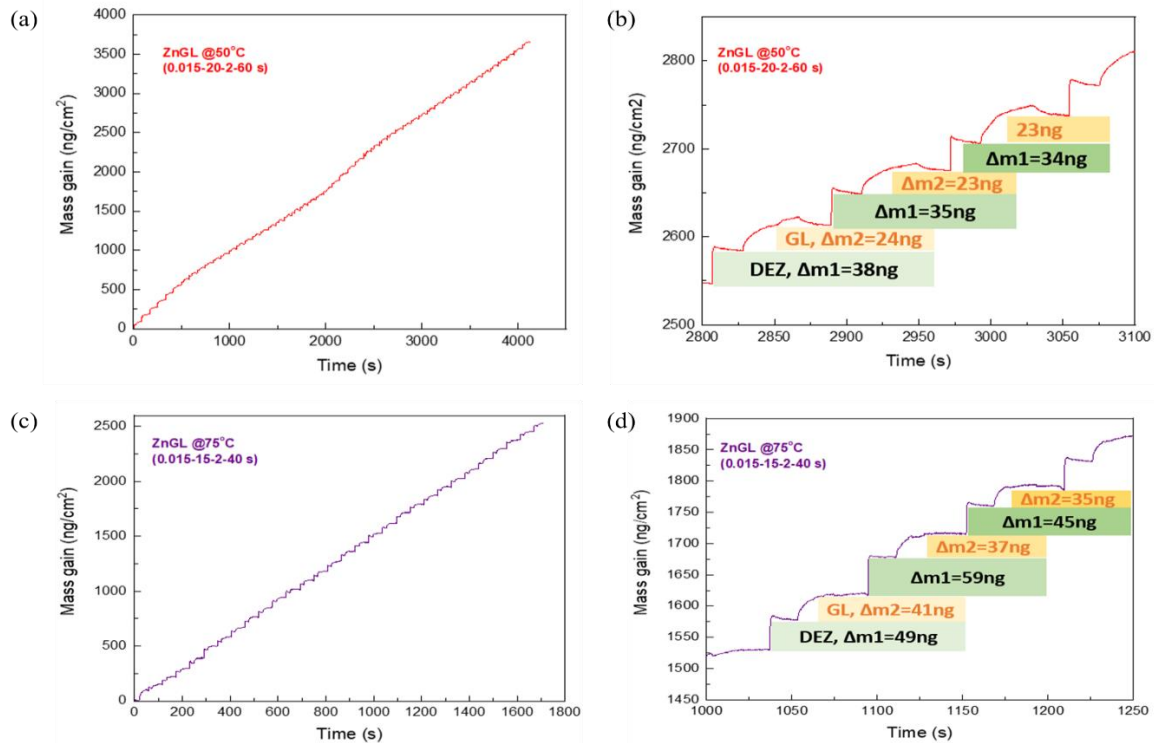


Figure 10. (a) Mass gain of ZnGL deposited at 50 °C using the recipe of (DEZ-purge-GL-purge, 0.015-20-2-60 s); (b) Three consequential cycles of ZnGL deposited at 50 °C using the recipe of (DEZ-purge-GL-purge, 0.015-20-2-60 s); (c) Mass gain of ZnGL deposited at 75 °C using the recipe of (DEZ-purge-GL-purge, 0.015-15-2-40 s); (d) Three consequential cycles of ZnGL deposited at 75 °C using the recipe of (DEZ-purge-GL-purge, 0.015-15-2-40 s).

ZnGL was deposited on NGS at 50 °C by MLD using a recipe of (DEZ-purge-GL-purge, 0.03-20-4-60 s). SEM results indicated that no obvious morphological difference between bare NGS (Figure 11(a)(b)) and 5x ZnGL coated NGS (Figure 11(c)(d)) were observed. Small particles of ZnGL can be detected for 10x and 15x ZnGL coated NGS (Figure 11(e)-(h)).

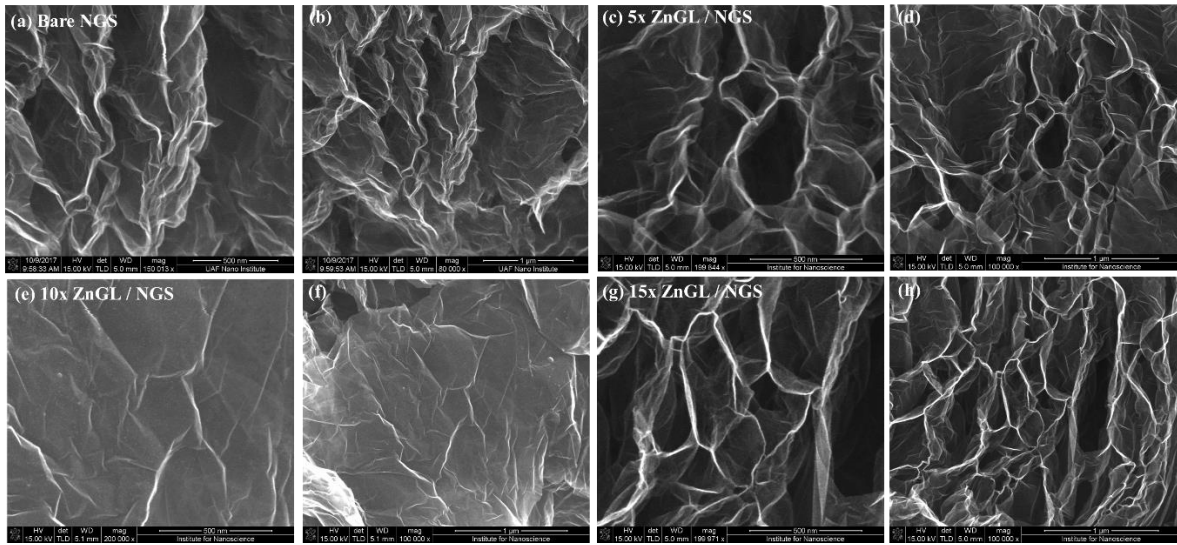


Figure 11. SEM pictures of (a) (b) bare NGS and (c) (d) 5x ZnGL coated NGS, (e) (f) 10x ZnGL coated NGS, and (g) (h) 15x ZnGL coated NGS. ZnGL was deposited at 50 °C using a recipe of (DEZ-purge-GL-purge, 0.03-20-4-60s).

AFM was also employed to characterize the surface roughness of ZnGL. The ZnGL sample for AFM test was deposited on Si wafer at 150 °C using 150 cycles of (DEZ-purge-GL-purge, 1-60-1-60 s). The arithmetical mean deviation (R_a) of the assessed $600 \times 600 \text{ nm}^2$ area was 0.118 nm. And the room-mean-squared (RMS) surface roughness for a $1 \times 1 \text{ }\mu\text{m}^2$ area averaged 0.112 nm (Figure 12).

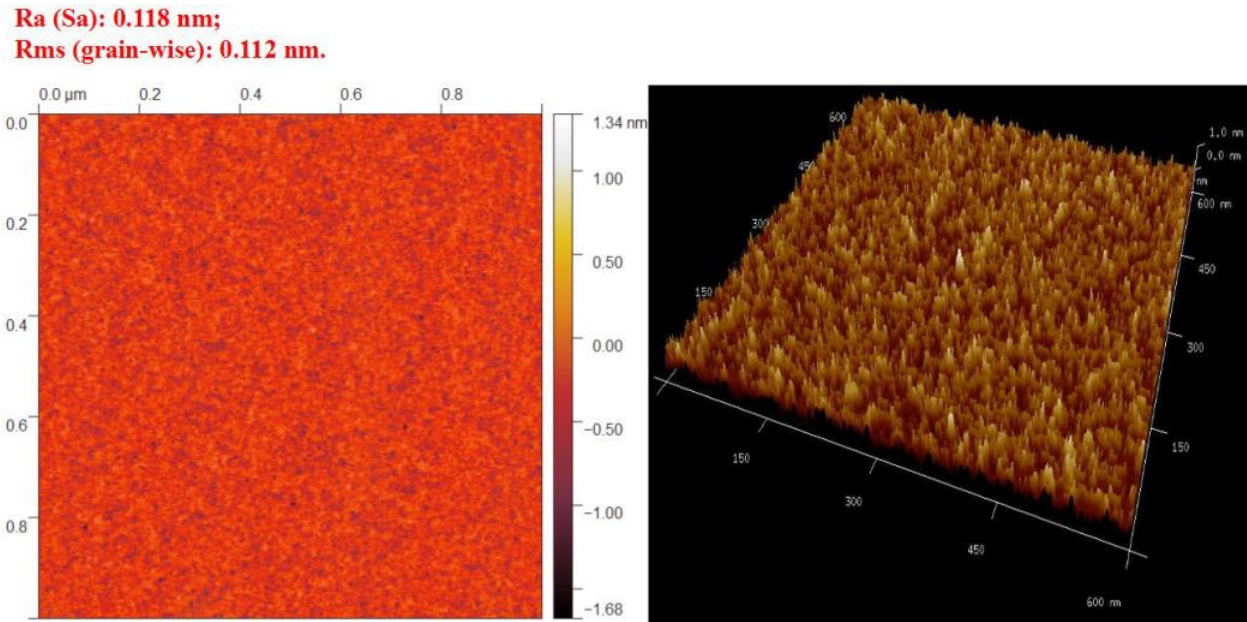


Figure 12. AFM of ZnGL deposited on Si wafer at 150 °C using 150 cycles of (DEZ-purge-GL-purge, 1 s-60 s-1 s-60 s).

2.5 Summary

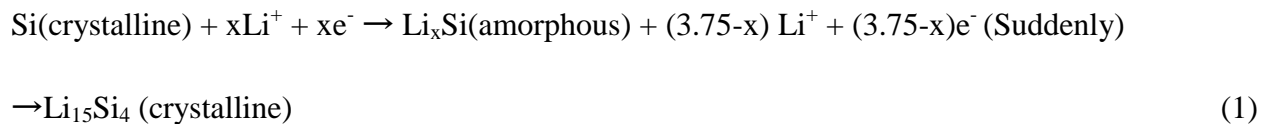
In this chapter, I deposited Al_2O_3 , TiO_2 , ZnO by ALD on Si wafer and employed QCM to investigate their growth properties. MGPC and GPC were analyzed. Similarly, AlGL and ZnGL were deposited by MLD on Si wafer to study their growth properties. MGPC was analyzed. Additionally, SEM was employed to investigate the morphologies of the deposited materials on NGS.

3 MODIFICATION OF SI-ELECTROLYTE INTERFACE

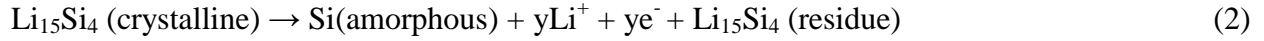
3.1 Introduction of Si Electrode

In recent years, LIBs are becoming more and more important in electric vehicles (EVs), hybrid-electric vehicles (HEVs) and energy storage of renewable sources (wind, solar) [1]. However, traditional electrodes materials [2] exhibit low storage capacity, plaguing LIBs. Different types of anode materials are intensively investigated, for example, intercalation/de-intercalation (graphite), alloy/de-alloy (Si), and conversion anodes (metal sulfides). A graphite/LiCoO₂ battery operates with an electrochemical mechanism based on Li⁺ intercalation [3,4]. But graphite and LiCoO₂ have low theoretical capacities of 372 and 147 mAh/g [5]. Compared with intercalation/de-intercalation anodes, alloy/de-alloy anode materials usually achieve higher capacity. And alloying reaction can also store more lithium than intercalation reaction [6]. Since 1971, Dey [7] indicated that Li can alloy with Sn, Al, Mg and Cu at room temperature in organic electrolytes. Si becomes the main research material attributed to its high capacity in Li alloy-based anode materials [8]. In 1966, Inhoffen [9] firstly discovered Li₂₂Si₅, demonstrating the mechanism of Si lithiation. Later, researchers found that Li₁₂Si₇, Li₁₄Si₆, Li₁₃Si₄, and Li₂₂Si₅ alloys formed because of the alloying process in Si anodes [10,11]. During discharge, crystal Si transitioned to lithiated amorphous Li_xSi, and then suddenly turned to Li₁₅Si₄ at 50 mV. While during charge, a reversible transition from Li₁₅Si₄ to Si (amorphous) happened. These could be described as Equations (1) and (2) [12-14].

During dealloying (lithiation, discharge):



During alloying (delithiation, charge):



Si exhibits a high theoretical value of 4200 mAh/g [15], which makes it a promising anode material for LIBs. However, Si anodes suffer from several challenges. (1) Si exhibits large volume change of 400% during charge-discharge process because of the Li insertion and extraction [1,11]. The volume expansion of Si by Li insertion will lead to large elastic strain and structural pulverization [16-18] (Figure 1(a)). (2) After several charge-discharge cycles, stress induced by the volume expansion/contraction of Si will lead to morphological change (fracture) of Si electrode [19]. Si crumbles away from the electrode, thereby lowering the electrode capacity [1,20] (Figure 1(b)). (3) There is continuous growth of SEI between Si and electrolyte ascribed to the large volume change of Si, consuming electrolyte and lithium [1,21] (Figure 1(c)). Several strategies can be employed to address these problems, including applying nanostructured Si anodes (nanotubes [22,23], nanowires [24,25], nanocomposite [26], thin films [27,28], nanoporous structures [29,30]), alloying Si with other materials [31], and modifying Si-electrolyte interface [32,33]. Among these efforts, ALD is confirmed to be effective in modifying Si anodes. Different ALD coatings were deposited on Si-based anodes, such as ALD- Al_2O_3 [34,35], ALD- TiO_2 [36], ALD- ZnO [37], ALD- TiN [38], and ALD- HfO_2 [39,40]. These coatings can effectively improve the electrochemical performance of Si-based anodes.

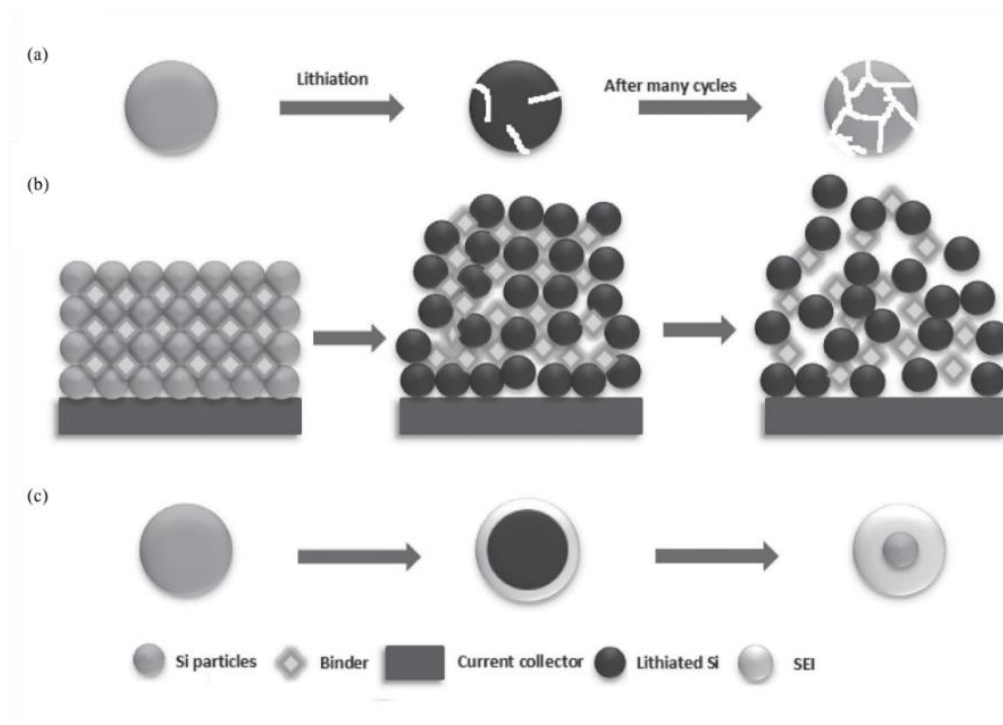


Figure 1. Failure mechanisms of a Si anode: (a) material pulverization and volume change of the Si electrodes, (b) morphology change of Si electrodes, and (c) SEI formation [1]. Reprinted (adapted) with permission from ref. [1]. Copyright (2015) John Wiley and Sons.

3.2 Experimental Materials and Equipment

3.2.1 Materials

DEZ was purchased from Strem chemicals. INC. H₂O was purchased from Sigma Aldrich. The silicon-graphite (Si-G) electrodes were obtained from Oak Ridge National Laboratory (ORNL). The Si-G electrode was composed of 15 wt% Si/73 wt% graphite/2 wt% C65 carbon black/10 wt% LiPAA. Therefore, the effective materials in Si-G electrode account for 88 % (15 % Si+73 % graphite). The electrode loading was 3.6 mg/cm². Lithium polyacrylate (LiPAA) was titrated from PAA to pH=7 corresponding to about 80 % of proton being replaced by Li. It's water soluble and thermally stable up to 190-200 °C. In comparison, PAA started decomposing at 150 °C. The electrolyte consisted of 90 wt% G2 (1.2 M LiPF₆ in EC/EMC (3:7, wt:wt)) with 10 wt% fluoroethylene carbonate (FEC), provided by ORNL.

3.2.2 Equipment

The Savannah S200 atomic layer deposition systems (Ultratech/Cambridge nanotech) was integrated with the glove box as shown in Figure 2(a). Electrochemical behavior of batteries was tested using the Xinwei battery testing station (BTS) as shown in Figure 2(b)(c)(d). Coin Cell Crimper was shown in Figure 2(e). Electrochemical impedance spectroscopy (EIS) was measured by SP-200 BioLogic Science Instrument as shown in Figure 2(f). SEM and EDX pictures were taken by FEI Nova Nanolab 200 Dual-Beam Workstation at University of Arkansas, as indicated in Figure 2(g). The accelerating voltages were 200 V to 30 kV for electrons and 5 to 30 kV for ions. Detectors were In-Lens SE and BSE Detector and Bruker XFlash 5010. SEM resolutions were 1.0 nm @ 15 kV and 2.5 nm @ 1 kV.



Figure 2. An Integrated System Combining Atomic/Molecular Layer Deposition with Glove Box; (b) (c) Battery Cyclers; (d) Battery Cyclers; (e) Coin Cell Crimper; (f) SP-200 BioLogic Science Instrument; (g) FEI Nova Nanolab 200 Dual-Beam Workstation.

3.3 Deposition of ZnO on Si-G Electrode

ZnO was deposited on Si-G electrode at 150 °C using DEZ and H₂O as precursors. The recipe was (DEZ-purge-H₂O-purge, 0.015-5-0.015-5 s) and the growth rate was 2.5 Å/cycle. Thicknesses of ZnO films were 0, 2, 4, 6, 8 and 10 nm controlled by 0, 8, 16, 24, 32 and 40 ALD cycles respectively. The obtained electrode was signed as ALD-ZnO coated Si-G.

3.4 Preparation of Li/Si-G batteries

Li/Si-G cell was prepared in the glove box. The components of Li/Si-G battery and order of their assembly into a CR2032 coin-type cell were shown in Figure 3. Firstly, Li metal was put on the cap, followed by adding electrolyte (G2:FEC, 9:1, wt:wt). Then, separator (polypropylene, polyethylene materials and additives) was put. On separator, electrolyte (G2:FEC, 9:1, wt:wt) was added to saturate the battery. Next, Si-G anode or ALD-ZnO coated Si-G was put. After which, spacer, cone spring, gasket and can was put sequentially. Finally, the coin cell was crimped, put in the glove box (10 h) for electrochemical behavior tests. Batteries were assembled and summarized in Table 1.

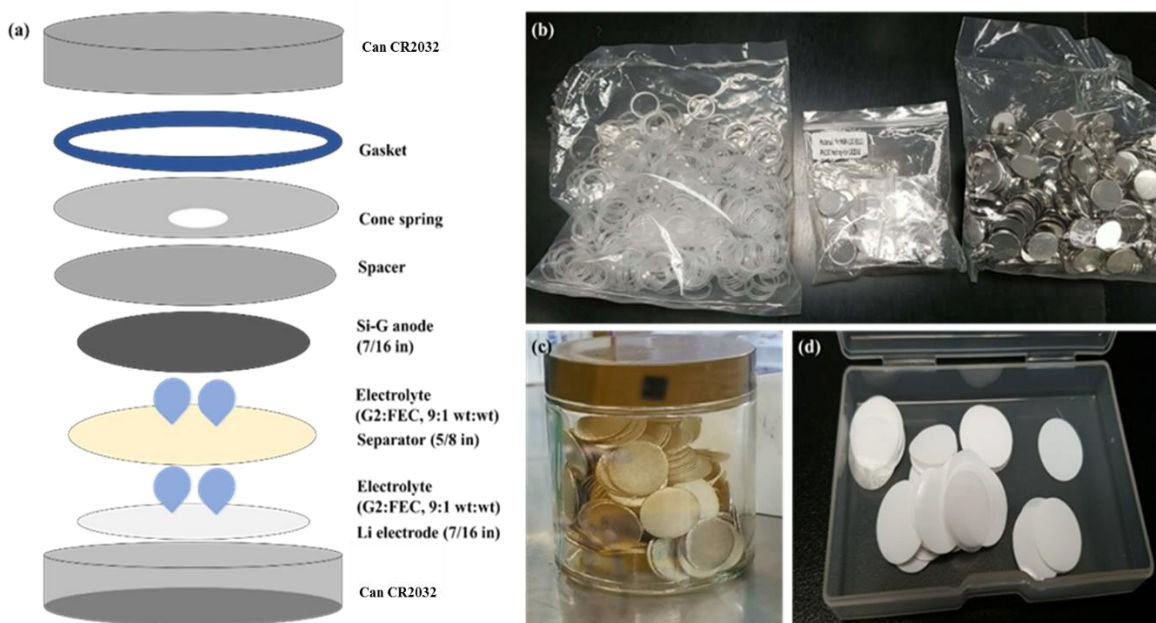


Figure 3. (a) Schematic illustration of Li/Si-G cell; (b) CR2032 coin cell; (c) Li metal; (d) Separator (polypropylene, polyethylene materials and additives).

Table 1. Summary of assembled batteries (1)

Battery	Electrolyte: G2/FEC (9:1, wt:wt)		
	Group1	Group2	Group3
Bare Li/Si-G	10 μ L	20 μ L	Electrolyte was added to saturate the Li/Si-G battery
Li/2 nm ZnO coated Si-G			
Li/4 nm ZnO coated Si-G			
Li/6 nm ZnO coated Si-G			
Li/8 nm ZnO coated Si-G			
Li/10 nm ZnO coated Si-G			

3.5 Results Discussion

3.5.1 AFM picture

AFM was employed to determine the surface roughness of the ALD ZnO. ZnO was deposited directly on Si at 150 °C by 150 ALD cycles of (DEZ-purge-H₂O-purge, 0.015-5-0.015-5 s) for

AFM test. The result indicated that Ra for a $600 \times 600 \text{ nm}^2$ area was 0.802 nm and RMS surface roughness for a $1 \times 1 \mu\text{m}^2$ area averaged 1.041 nm (Figure 4).

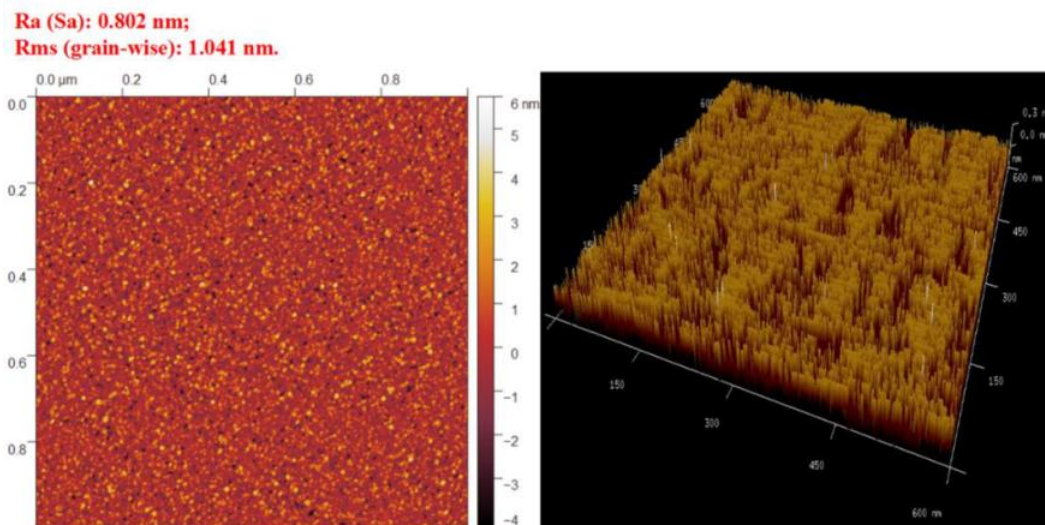


Figure 4. AFM picture of ALD-ZnO deposited on Si wafer at 150 °C using 150 ALD cycles of (DEZ-purge-H₂O-purge, 0.015-5-0.015-5 s).

3.5.2 SEM and EDX pictures

SEM results demonstrated the morphology of bare Si-G electrode (Figure 5(a)-(c)). And EDX confirmed C, Si and O distribution for bare Si-G electrode (Figure 5(d)-(f) for Figure 5(c)).

Compared with the bare Si-G, small particles of ZnO can be observed in the 6 nm ZnO coated Si-G electrode, as shown in Figure 6(a)-(c). C, Si, Zn and O distribution confirmed by EDX (Figure 6(d)-(g) for Figure 6(c)) also demonstrated successful deposition of ZnO on Si-G electrode.

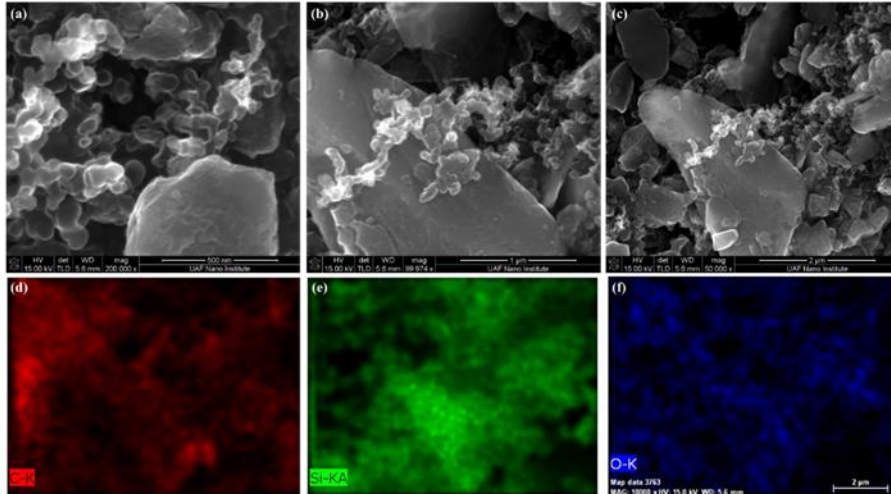


Figure 5. SEM pictures of bare Si-G electrode with magnifications of (a) (x200000), (b) (x99974), and (c) (x50000) before battery cycling; EDX results of (d) C, (e) Si, and (f) O distribution for (c).

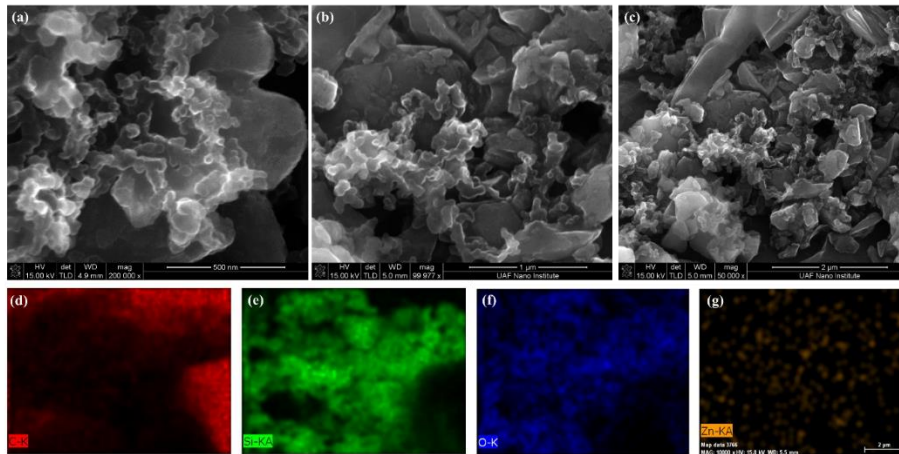


Figure 6. SEM pictures of 6 nm ALD-ZnO (deposited at 150 °C) coated Si-G electrode with magnifications of (a) (x200000), (b) (x99977), and (c) (x50000) before battery cycling; EDX results of (d) C, (e) Si, (f) O, and (g) Zn distribution for (c).

According to the peak heights of Zn in EDX mapping for bare Si-G and ZnO coated Si-G samples (Figure 7(a)), we conclude observe that the thicker the ZnO layer was, the larger peak value of Zn in EDX mapping would be.

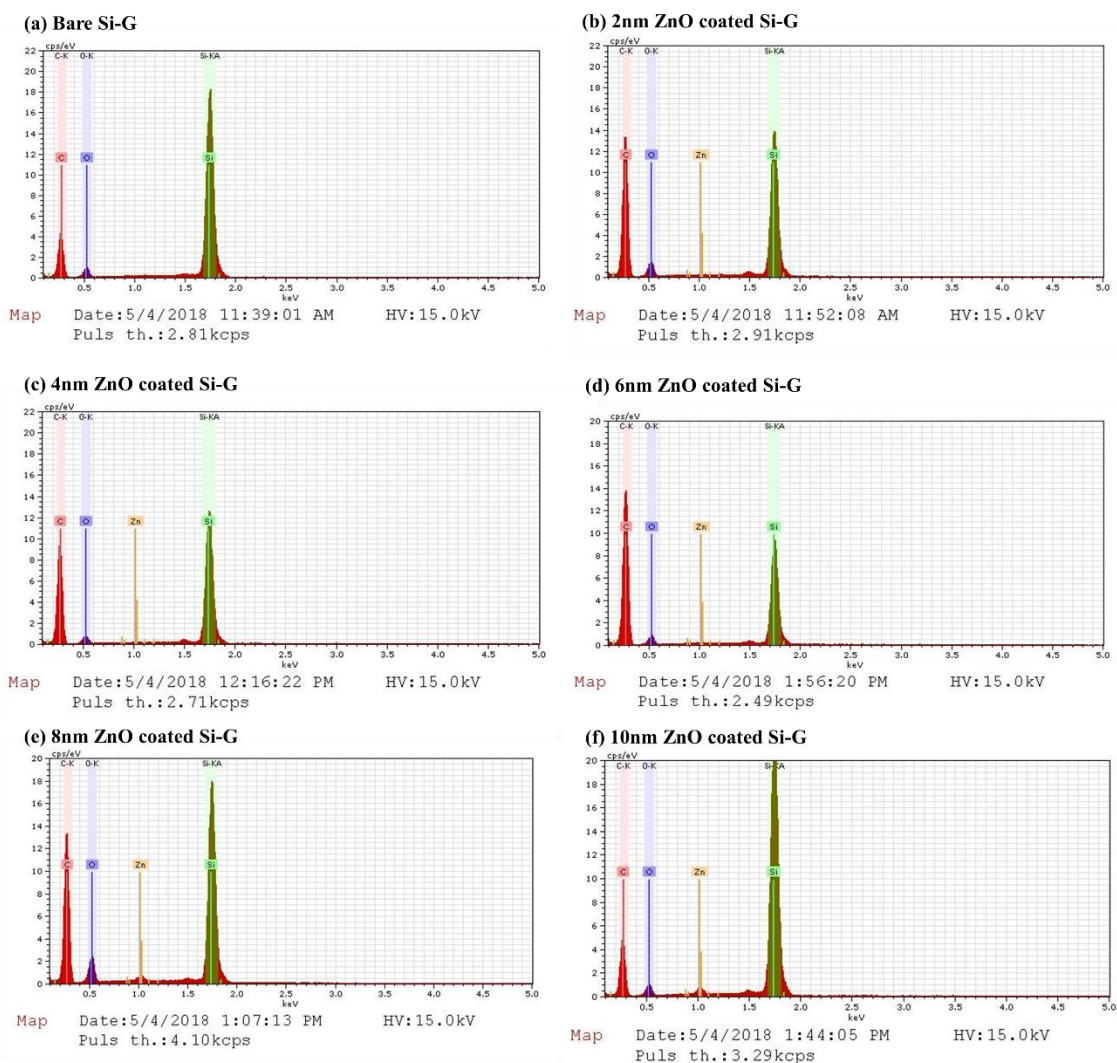


Figure 7. EDX mapping results of (a) bare Si-G, (b) 2nm ZnO coated Si-G, (c) 4nm ZnO coated Si-G, (d) 6nm ZnO coated Si-G, (e) 8nm ZnO coated Si-G, and (f) 10nm ZnO coated Si-G before battery cycling, which correspond to their SEM pictures with magnification of (x50000).

Bare Si-G and ZnO coated Si-G were paired with Li metal to assemble batteries. Before battery cycling (first 3 cycles at 1/20 C, last 97 cycles at 1/3 C, 1C = 808 mA/g), we could observe thin layers on Si-G electrodes, indicating successful deposition of ZnO (Figure 8(a)-(d)). While after 100 discharging-charging cycles, morphologies of samples changed greatly. White parts in Figure 8(e)-(h) referred to SEI, therefore we could conclude that the effects of ZnO on improving Si-G was ordered as 6 nm ZnO coated Si-G > bare Si-G > 8 nm ZnO coated Si-G > 10 nm ZnO

coated Si-G. The reason why this happened would be given in **3.5.4 Electrochemical behavior of Si-G electrode.**

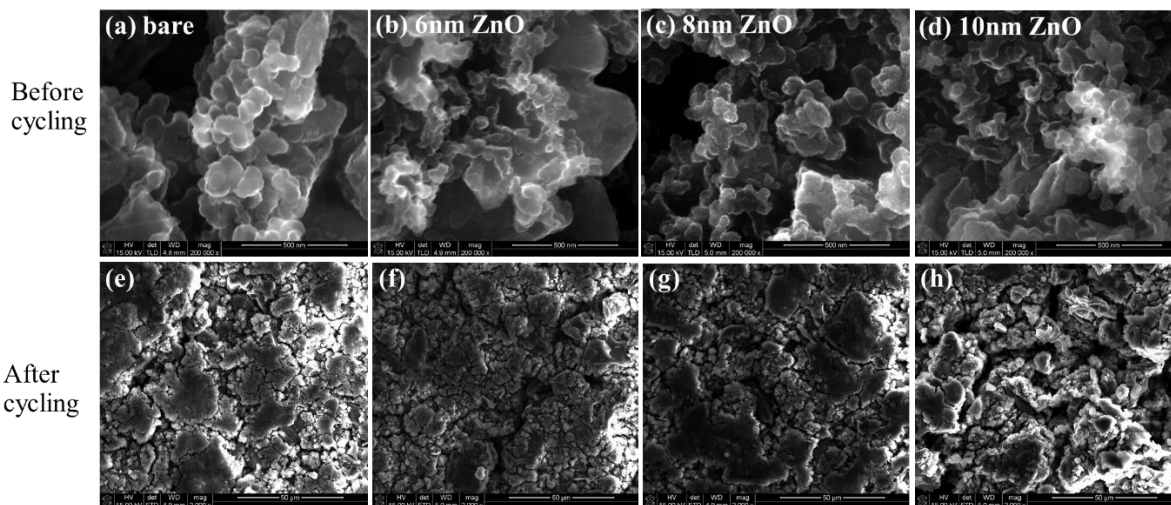


Figure 8. SEM pictures of (a) (e) bare Si-G electrode and (b) (f) 6 nm, (c) (g) 8 nm, (d) (h) 10 nm ZnO (deposited at 150 °C) coated Si-G electrodes before and after 100 discharge-charge cycles. Recipe of ALD-ZnO is (DEZ-purge-H₂O-purge, 0.015-5-0.015-5 s), the growth rate is 1.0 Å/cycle.

3.5.3 XRD result

X-ray diffraction (XRD) was employed to identify the crystal orientation of ZnO. As shown in Figure 9, ZnO deposited at 150 °C exhibited a crystal of Zn (101).

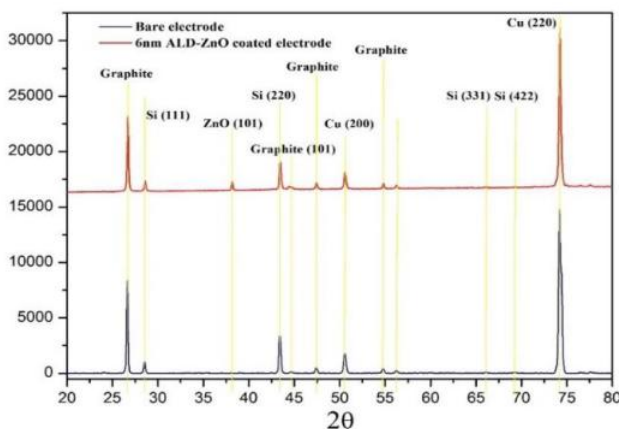


Figure 9. XRD of Si-G electrode and 6 nm ALD-ZnO (deposited at 150 °C) coated Si-G anode.

3.5.4 Electrochemical behavior of Si-G electrode

3.5.4.1 Discharge capacity, retention and voltage-capacity profile of bare Si-G electrode and ZnO coated Si-G

Electrochemical behavior of bare Li/Si-G and Li/ZnO coated Si-G batteries were tested using Xinwei battery testing station (BTS) (first 3 cycles at 1/20 C, last 97 cycles at 1/3 C, then back to 1/20 C, 1 C = 808 mA/g). Electrochemical behavior of bare Si-G and ZnO coated Si-G was compared, the discharge capacity and capacity retention of these electrodes were sequenced as 6 nm ZnO coated Si-G > 4 nm ZnO coated Si-G > 2 nm ZnO coated Si-G > bare Si-G > 8 nm ZnO coated Si-G > 10 nm ZnO coated Si-G (Figure 10(a)(b)(d)(e)). 6 nm ZnO was optimal to improve the performance of Si-G electrode by protecting Si-G electrode and suppressing the side reaction between Si-G electrode and electrolyte, which was followed by 4 nm ZnO. 2 nm ZnO was too thin to cover the Si-G surface completely, it can increase the capacity less effectively than 4 nm and 6 nm ZnO. Too thick ZnO layers (8, 10 nm) blocked ion transfer, thus leading to worse electrochemical performance than bare Si-G. Electrolyte volume was important to the performance of Li/Si-G batteries, we can observe that batteries using 10 μ L G2/FEC (9:1, wt/wt) exhibited faster capacity fading and worse capacity retention than those saturated by electrolyte. Li/6 nm ZnO coated Si-G with 10 μ L electrolyte displayed a discharge capacity of 907.14856 mAh/g initially, and 860.01816 mAh/g for the second cycle, higher than the capacities of 834.46502 (first cycle) and 796.56928 (second cycle) mAh/g of bare Li/Si-G with 10 μ L electrolyte (Figure 10(c)). Li/6 nm ZnO coated Si-G (saturated electrolyte) also exhibited higher discharge capacity than bare Li/Si-G (saturated electrolyte) for the first two cycles. Discharge capacities of batteries for the first three cycles were summarized in Table 2.

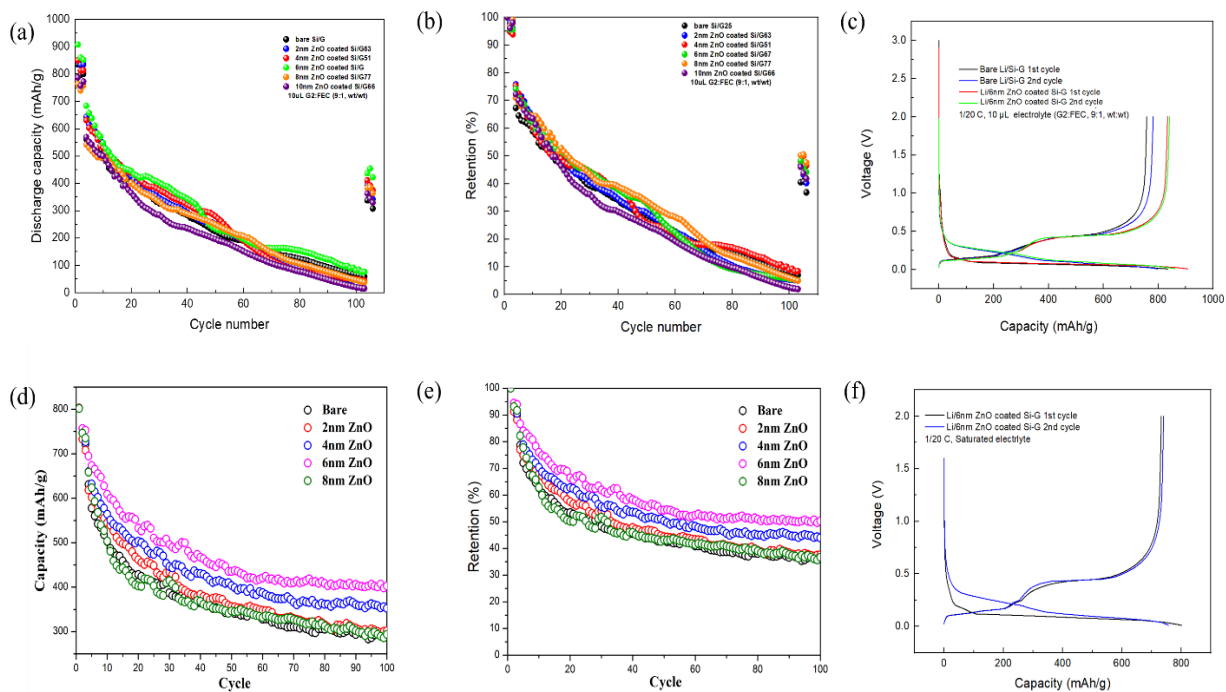


Figure 10. Discharge capacity of bare Li/Si-G and Li/ZnO coated Si-G batteries with (a) 10 μL electrolyte and (d) saturated electrolyte; Capacity retention of bare Li/Si-G and Li/ZnO coated Si-G batteries with (b) 10 μL electrolyte and (e) saturated electrolyte; Voltage-capacity profile for first two cycles of (c) bare Li/Si-G and Li/ 6 nm ZnO coated Si-G batteries with 10 μL electrolyte and (f) that of Li/6 nm ZnO coated Si-G batteries with saturated electrolyte.

Table 2. Discharge capacities for first 3 cycles of batteries

Battery	Electrolyte	Discharge capacity (mAh/g)		
		1st cycle	2nd cycle	3rd cycle
Bare Li/Si-G	10 μL G2:FEC, (9:1, wt:wt)	834.46502	796.56928	800.10832
Li/6 nm ZnO coated Si-G		907.14856	860.01816	851.65036
Bare Li/Si-G	saturated	801.37143	756.74606	720.99725
Li/6 nm ZnO coated Si-G	G2:FEC, (9:1, wt:wt)	801.46302	756.80805	752.82198

3.5.4.2 EIS result

Electrochemical impedance spectroscopy (EIS) was utilized to evaluate the performance of batteries. Figure 11(a) compared the electrochemical impedance of bare Li/Si-G and Li/ZnO coated Si-G (10 μ L electrolyte). Equivalent circuits were inserted in Figure 11(a), and the measured impedance curves consisted of depressed semicircles in the high frequency region representing the charge transfer resistance on electrode/electrolyte interface (R_{ct}) and sloping lines in the low frequency range representing the interfacial diffusion resistance of ions at the interface of electrolyte and anode (Warburg impedance, W) [41,42]. The simulated results were given in Table 3, the impedance was ordered as 10 nm ZnO coated Si/G > 8 nm ZnO coated Si/G > bare Si/G > 2 nm ZnO coated Si/G > 4 nm ZnO coated Si/G > 6 nm ZnO coated Si/G, confirming the performance of batteries as 6 nm ZnO coated Si/G > 4 nm ZnO coated Si/G > 2 nm ZnO coated Si/G > bare Si/G > 8 nm ZnO coated Si/G > 10 nm ZnO coated Si/G.

Bare Li/Si-G (20 μ L electrolyte) delivered a smaller impedance after 8 cycles than that after 15 and 20 cycles. After 20 cycles, the bare Li/Si-G exhibited a semicircle (the first one) that is related to SEI in the high frequency. And the second semicircle is related to the electron transfer in particles of active materials. The linear part was related to the solid diffusion process of Li^+ in the inside of particles of active materials (Figure 11(b)). The Li/6 nm ZnO coated Si-G (20 μ L electrolyte) delivered larger impedance after 27 cycles than that after cycling 11 cycles. After 21 cycles, there exhibited two semicircles related to SEI (high frequency) and the electron transfer in particles of active materials, respectively. After 27 cycles, the impedances increased greatly (Figure 11(c)).

For Li/6 nm ZnO coated Si-G (saturated electrolyte), the impedance was ordered as after 28 cycles > after 0 cycles > 7 cycles > 14 cycles > 21 cycles (Figure 11(d)). This probably because

ZnO started exhibiting obvious effect of lowering impedance after 7 cycles. With the increase of charging-discharging cycles, this effect faded, thereby leading to increased impedance.

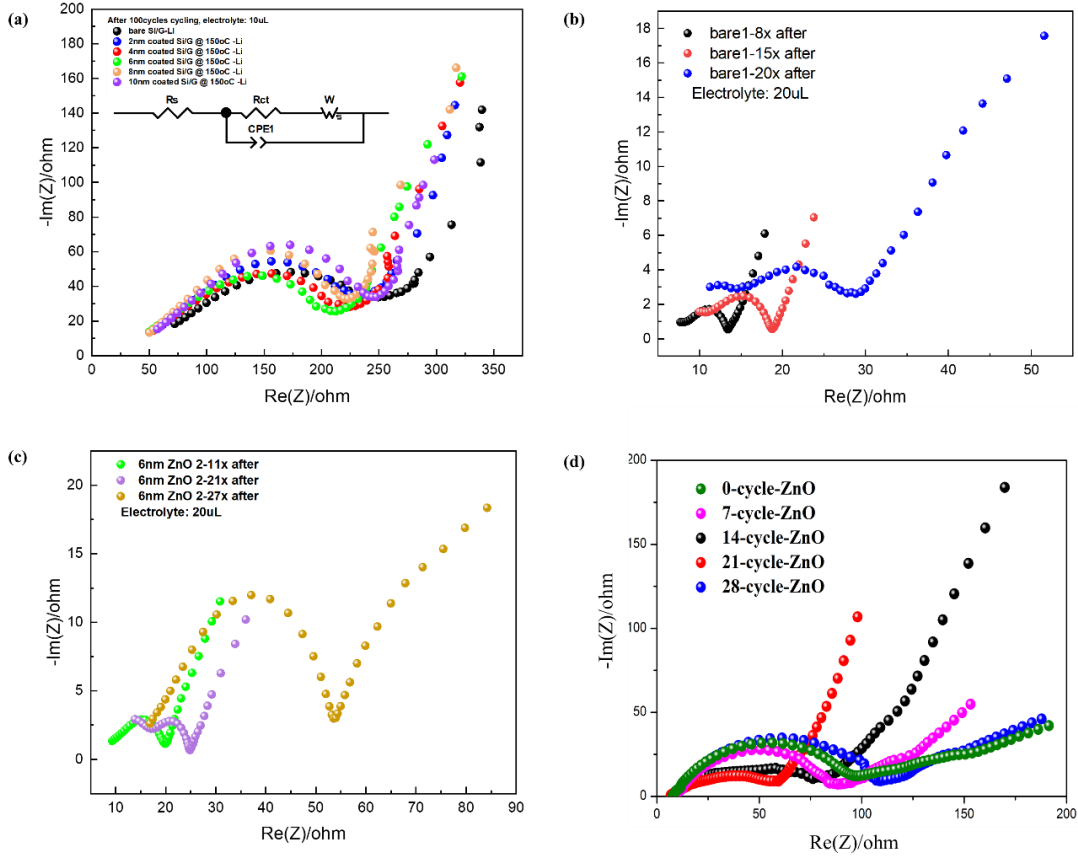


Figure 11. EIS results of (a) bare Li/Si-G and Li/ZnO coated Si-G battery using 10 μ L electrolyte (G2/FEC, 9:1, wt:wt) after 100 charge-discharge cycles; (b) bare Li/Si-G battery using 20 μ L electrolyte (G2/FEC, 9:1, wt:wt) after 8, 15 and 20 charge-discharge cycles; (c) Li/6 nm ZnO coated Si-G battery using 20 μ L electrolyte (G2/FEC, 9:1, wt:wt) after 11, 21 and 27 charge-discharge cycles; (d) Li/6 nm ZnO coated Si-G battery using saturated electrolyte after 0, 7, 14, 21 and 28 charge-discharge cycles.

Table 3. Simulated EIS results of bare Li/Si-G and Li/ZnO coated Si-G batteries using 10 μ L electrolyte (G2/FEC, 9:1, wt:wt)

Batteries	Rs(ohms)	Rct(ohms)	CPE1 (F)
Bare Li/Si-G	/	135.4	/
Li/2 nm ZnO coated Si-G	85.62	135.1	0.5619E-6
Li/4 nm ZnO coated Si-G	65.76	129.2	0.7162E-6
Li/6 nm ZnO coated Si-G	61.02	123.2	0.7502E-6
Li/8 nm ZnO coated Si-G	60.73	136.3	0.7907E-6
Li/10 nm ZnO coated Si-G	69.12	150.2	0.7144E-6

3.6 Summary

In this chapter, ALD ZnO was deposited using DEZ and H₂O as precursors at 150 °C to modify the interface between Si-G and electrolyte. 2, 4, 6, 8 and 10 nm ZnO were deposited on Si/G, then the obtained ZnO coated Si-G electrodes were paired with Li metal to assemble batteries. AFM was used to determine the surface roughness of ZnO on silicon wafer. SEM and EDX were employed to characterize the morphology and bare Si-G and ZnO coated Si-G electrodes. XRD was utilized to indicate that ZnO deposited at 150 °C exhibited a crystal orientation of Zn (101). Then, electrochemical behavior of bare Li/Si-G and Li/6 nm ZnO coated Si-G was investigated. 6 nm ZnO coated Si-G exhibited the best electrochemical performance in terms of discharge capacity and capacity retention, which was followed by 4 nm ZnO coated Si-G. 2 nm ZnO was too thin and cannot cover the Si-G surface completely, thereby improving the battery performance less effectively than 4 nm and 6 nm coated Si-G. 10 nm ZnO was too thick and blocked ion transfer, leading to worse electrochemical behavior than bare Si-G. Finally, EIS was used to evaluate the performance of batteries.

3.7 References

- [1] M.A. Rahman, G. Song, A.I. Bhatt, Y.C. Wong, C. Wen, Nanostructured silicon anodes for high-performance lithium-ion batteries, *Advanced Functional Materials* 26 (2016) 647-678.
- [2] B. Dunn, H. Kamath, J.M. Tarascon, Electrical energy storage for the grid: a battery of choices, *Science* 334 (2011) 928-935.
- [3] P. He, H. Yu, H. Zhou, Layered lithium transition metal oxide cathodes towards high energy lithium-ion batteries, *Journal of Materials Chemistry* 22 (2012) 3680-3695.
- [4] Z. Shu, R. McMillan, J. Murray, Electrochemical intercalation of lithium into graphite, *J. Electrochem. Soc.* 140 (1993) 922-927.
- [5] H. Peng, *Fiber-shaped energy harvesting and storage devices*, Springer (2015).
- [6] D. Ma, Z. Cao, A. Hu, Si-based anode materials for Li-ion batteries: a mini review, *Nano-Micro Letters* 6 (2014) 347-358.
- [7] A. Dey, Electrochemical alloying of lithium in organic electrolytes, *J. Electrochem. Soc.* 118 (1971) 1547-1549.
- [8] C. Park, J. Kim, H. Kim, H. Sohn, Li-alloy based anode materials for Li secondary batteries, *Chem. Soc. Rev.* 39 (2010) 3115-3141.
- [9] H.H. Inhoffen, J. Fuhrhop, H. Voigt, H. Brockmann Jr, Zur weiteren Kenntnis des Chlorophylls und des Hämins, VI. Formylierung der meso-Kohlenstoffatome von Alkyl-substituierten Porphyrinen, *Justus Liebigs Ann. Chem.* 695 (1966) 133-143.
- [10] W. Weydanz, M. Wohlfahrt-Mehrens, R.A. Huggins, A room temperature study of the binary lithium-silicon and the ternary lithium-chromium-silicon system for use in rechargeable lithium batteries, *J. Power Sources* 81 (1999) 237-242.
- [11] B. Boukamp, G. Lesh, R. Huggins, All-solid lithium electrodes with mixed-conductor matrix, *J. Electrochem. Soc.* 128 (1981) 725-729.
- [12] J. Li, J. Dahn, An in situ X-ray diffraction study of the reaction of Li with crystalline Si, *J. Electrochem. Soc.* 154 (2007) A156-A161.
- [13] I. Ryu, J.W. Choi, Y. Cui, W.D. Nix, Size-dependent fracture of Si nanowire battery anodes, *J. Mech. Phys. Solids* 59 (2011) 1717-1730.
- [14] T. Hatchard, J. Dahn, In situ XRD and electrochemical study of the reaction of lithium with amorphous silicon, *J. Electrochem. Soc.* 151 (2004) A838-A842.

- [15] H. Ma, F. Cheng, J. Chen, J. Zhao, C. Li, Z. Tao, et al., Nest-like silicon nanospheres for high-capacity lithium storage, *Adv Mater* 19 (2007) 4067-4070.
- [16] H. Kim, M. Seo, M. Park, J. Cho, A critical size of silicon nano-anodes for lithium rechargeable batteries, *Angewandte Chemie International Edition* 49 (2010) 2146-2149.
- [17] T. Ichitsubo, S. Yukitani, K. Hirai, S. Yagi, T. Uda, E. Matsubara, Mechanical-energy influences to electrochemical phenomena in lithium-ion batteries, *Journal of Materials Chemistry* 21 (2011) 2701-2708.
- [18] T. Ichitsubo, S. Yagi, T. Doi, S. Yukitani, K. Hirai, E. Matsubara, Influence of mechanical strain on the electrochemical lithiation of aluminum-based electrode materials, *J. Electrochem. Soc.* 159 (2011) A14-A17.
- [19] L. Beaulieu, K. Eberman, R. Turner, L. Krause, J. Dahn, Colossal reversible volume changes in lithium alloys, *Electrochemical and Solid-State Letters* 4 (2001) A137-A140.
- [20] J. Graetz, C. Ahn, R. Yazami, B. Fultz, Highly reversible lithium storage in nanostructured silicon, *Electrochemical and Solid-State Letters* 6 (2003) A194-A197.
- [21] H. Wu, G. Chan, J.W. Choi, I. Ryu, Y. Yao, M.T. McDowell, et al., Stable cycling of double-walled silicon nanotube battery anodes through solid–electrolyte interphase control, *Nature nanotechnology* 7 (2012) 310-315.
- [22] M. Park, M.G. Kim, J. Joo, K. Kim, J. Kim, S. Ahn, et al., Silicon nanotube battery anodes, *Nano letters* 9 (2009) 3844-3847.
- [23] T. Song, J. Xia, J. Lee, D.H. Lee, M. Kwon, J. Choi, et al., Arrays of sealed silicon nanotubes as anodes for lithium ion batteries, *Nano letters* 10 (2010) 1710-1716.
- [24] K. Peng, J. Jie, W. Zhang, S. Lee, Silicon nanowires for rechargeable lithium-ion battery anodes, *Appl. Phys. Lett.* 93 (2008) 033105.
- [25] C.K. Chan, H. Peng, G. Liu, K. McIlwrath, X.F. Zhang, R.A. Huggins, et al., Materials for sustainable energy: A collection of peer-reviewed research and review articles from nature publishing group, World Scientific, (2011).
- [26] S. Ng, J. Wang, D. Wexler, K. Konstantinov, Z. Guo, H. Liu, Highly reversible lithium storage in spheroidal carbon-coated silicon nanocomposites as anodes for lithium-ion batteries, *Angewandte Chemie* 118 (2006) 7050-7053.
- [27] J. Maranchi, A. Hepp, P. Kumta, High capacity, reversible silicon thin-film anodes for lithium-ion batteries, *Electrochemical and solid-state letters* 6 (2003) A198-A201.
- [28] M. Demirkan, L. Trahey, T. Karabacak, Cycling performance of density modulated multilayer silicon thin film anodes in Li-ion batteries, *J. Power Sources* 273 (2015) 52-61.

- [29] C. Dücső, N.Q. Khanh, Z. Horváth, I. Bársony, M. Utriainen, S. Lehto, et al., Deposition of tin oxide into porous silicon by atomic layer epitaxy, *J. Electrochem. Soc.* 143 (1996) 683-687.
- [30] H. Kim, B. Han, J. Choo, J. Cho, Three-dimensional porous silicon particles for use in high-performance lithium secondary batteries, *Angewandte Chemie* 120 (2008) 10305-10308.
- [31] M. Obrovac, L. Christensen, D.B. Le, J.R. Dahn, Alloy design for lithium-ion battery anodes, *J. Electrochem. Soc.* 154 (2007) A849-A855.
- [32] Y. Chen, M. Nie, B.L. Lucht, A. Saha, P.R. Guduru, A. Bose, High capacity, stable silicon/carbon anodes for lithium-ion batteries prepared using emulsion-templated directed assembly, *ACS applied materials & interfaces* 6 (2014) 4678-4683.
- [33] J. Shin, K. Park, W. Ryu, J. Jung, I. Kim, Graphene wrapping as a protective clamping layer anchored to carbon nanofibers encapsulating Si nanoparticles for a Li-ion battery anode, *Nanoscale* 6 (2014) 12718-12726.
- [34] S. Myung, K. Amine, Y. Sun, Surface modification of cathode materials from nano-to microscale for rechargeable lithium-ion batteries, *Journal of Materials Chemistry* 20 (2010) 7074-7095.
- [35] M. Copel, E. Cartier, E. Gusev, S. Guha, N. Bojarczuk, M. Poppeller, Robustness of ultrathin aluminum oxide dielectrics on Si (001), *Appl. Phys. Lett.* 78 (2001) 2670-2672.
- [36] X. Su, Q. Wu, X. Zhan, J. Wu, S. Wei, Z. Guo, Advanced titania nanostructures and composites for lithium ion battery, *J. Mater. Sci.* 47 (2012) 2519-2534.
- [37] B. Zhu, N. Liu, M. McDowell, Y. Jin, Y. Cui, J. Zhu, Interfacial stabilizing effect of ZnO on Si anodes for lithium ion battery, *Nano Energy* 13 (2015) 620-625.
- [38] A. Kohandehghan, P. Kalisvaart, K. Cui, M. Kupsta, E. Memarzadeh, D. Mitlin, Silicon nanowire lithium-ion battery anodes with ALD deposited TiN coatings demonstrate a major improvement in cycling performance, *Journal of Materials Chemistry A* 1 (2013) 12850-12861.
- [39] J.C. Hackley, J.D. Demaree, T. Gougousi, Growth and interface of HfO₂ films on H-terminated Si from a TDMAH and H₂O atomic layer deposition process, *Journal of Vacuum Science & Technology A: Vacuum, Surfaces, and Films* 26 (2008) 1235-1240.
- [40] Q. Zhang, L. Han, J. Pan, Z. Chen, Y. Cheng, Chemically stable artificial SEI for Li-ion battery electrodes, *Appl. Phys. Lett.* 110 (2017) 133901.
- [41] T. Xu, N. Lin, W. Cai, Z. Yi, J. Zhou, Y. Han, et al., Stabilizing Si/graphite composites with Cu and in situ synthesized carbon nanotubes for high-performance Li-ion battery anodes, *Inorganic Chemistry Frontiers* (2018).

[42] R. Ruffo, S.S. Hong, C.K. Chan, R.A. Huggins, Y. Cui, Impedance analysis of silicon nanowire lithium ion battery anodes, *The Journal of Physical Chemistry C* 113 (2009) 11390-11398.

4 STABILIZATION OF LITHIUM METAL VIA ALD COATINGS

4.1 Introduction of Li Metal Anode

Since commercialized in the early 1990s [1-5], lithium ion batteries (LIBs) have dominated the field of portable electronics. However, LIBs exhibit low energy density of 100-220 Wh/kg [4,6], which is not favorable for their further developments in electric vehicles. Meanwhile, LIBs also have other problems such as stability and safety. In this case, lithium metal attracts much interests because of its high theoretical capacity (3860 mAh/g [7], much higher than 372 mAh/g of graphite anode in LIBs [2,8]), low density of 0.59 g/cm^3 , and low electrochemical potential of -3.04 V vs standard hydrogen electrode [7]. Li metal was employed as promising anodes in novel lithium metal batteries, such as Li-S [9] and Li-O₂ batteries. Li-S batteries exhibit a theoretical specific energy of $\sim 2600 \text{ Wh/kg}$, which is five to ten times higher than that of LIBs (Figure 1 (b)) [9,10]. Li-O₂ batteries (Figure 1 (c)) display theoretical energy densities of 3600 Wh/kg based on the reaction of $2\text{Li}^+ + \text{O}_2 \leftrightarrow \text{Li}_2\text{O}_2$ ($E^0 = 2.96 \text{ V}$) and 12000 Wh/kg based on the mass of Li metal only [11-15].

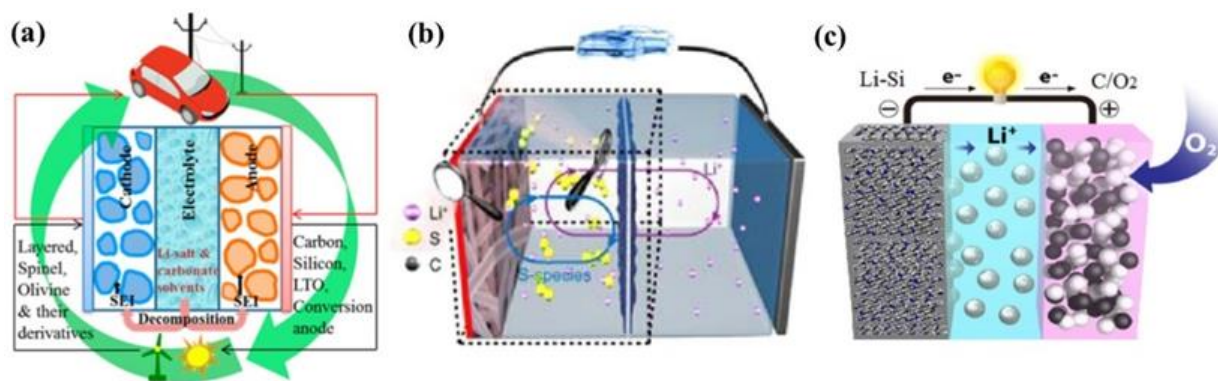


Figure 1. Schematic representations of (a) Li-ion [58]. Reprinted (adapted) with permission from ref. [58]. Copyright (2014) American Chemical Society. (b) Li-S [10]. Reprinted (adapted) with permission from ref. [13]. Copyright (2015) American Chemical Society. (c) Li-O₂ cells [15]. Reprinted (adapted) with permission from ref. [15]. Copyright (2012) American Chemical Society.

However, lithium metal suffered from many issues such as poor cyclability, inferior reversibility and safety risks. One serious problem is the growth of lithium dendrites, because of inhomogeneous Li^+ deposition. Li dendrites will decrease the Coulombic efficiency, lower the cycling performance, and affect the structure of interface of Li/electrode. In order to calculate the initiation time of dendrite growth near solid electrolyte interphase (SEI), Henry J. S. [16] proposed “Sand's time” (τ_s) in 1901 as shown in Equation 1.

$$\tau_s = \pi D \left(\frac{C_0 e Z_c}{2J} \right)^2 \left(\frac{\mu_a + \mu_c}{\mu_a} \right)^2 \quad (1)$$

Where μ_a and μ_c are anionic and cationic mobilities, e is electronic charge, J stands for effective electrode current density, C_0 is the initial concentration of Li salt. D is the diffusion coefficient, $D = (\mu_a D_c + \mu_c D_a) / (\mu_a + \mu_c)$, where D_c and D_a are cationic and anionic diffusion coefficients.

This equation indicates that large immigration rate of Li^+ (D and μ_c) and small current density (J) leads to large Sand's time” (τ_s), meaning that the battery exhibits a long cycling life before Li dendrite growth.

There are three kinds of lithium dendrites, including needle-like [17], mossy-like [18] and fractal-like [19]. Needle-like dendrites usually formed at a current density lower than 0.5 mA/cm^2 in LiPF_6 DMC/EC 1:1. They depended on many factors such as the electrolyte components, current density and substrate [17]. Needle-like dendrites grew in both diameter and length at the same time, being prone to cause shorted lithium metal batteries. Mossy-like dendrites generated at higher current density. Due to the increased surface area of Li dendrites, the cell potential decreased [18]. In this regard, the high ionic flux led to more SEI fractures and Li exposure to the electrolyte. Fractal-like dendrites happened at the Li/electrolyte interfaces where the Li ion concentration was zero and the potential fluctuated unstably all the times [20]. It needed to

mention that fractal-like dendrites would penetrate the separator, leading to shorted cell and even explosion.

There are several issues generated by Li dendrites (Figure 2) [13,21].

(1) Li anode displays huge volume change because of its hostless property, compared with the volume change of intercalated anodes (graphite (100%), silicon (400%)). This volume expansion will result in SEI cracks where lithium dendrites grew.

(2) Dead Li evolved from lithium dendrites. Li dendrites blocked ion transfer. Removal of Li from the roots of the dendrites generates dead Li, thereby decreasing Coulombic efficiency.

(3) Li dendrites growth will increase the surface area of Li and induce more parasitic reactions of lithium and the electrolyte.

(4) Li dendrites exhibit with porous structure increased diffusion pathway and resistance of Li^+ and e^- , leading to an increased polarization.

(5) Large-scale Li dendrites can penetrate the separator, short the battery, and lead to safety issues such as the electrolyte combustion and cell explosion.

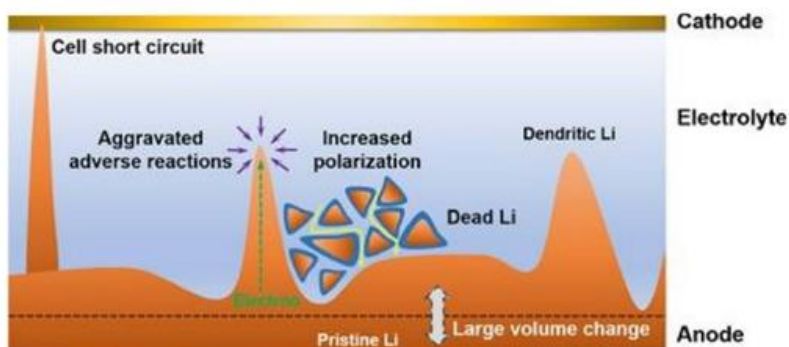


Figure 2. Scheme of dilemma for Li metal anode in rechargeable batteries [21]. Reprinted (adapted) with permission from ref. [21]. Copyright (2017) American Chemical Society.

In order to address these problems, several strategies are proposed, including modifying electrolyte via additives (LiNO_3 [22], CO_2 [23,24], fluorinated compounds (HF) [25,26], 2-methoxyfuran [27], vinylene carbonate (VC) [28], metal ions (Cs^+ , Na^+ , Mg^{2+}) [29-31] and organic aromatic compounds [32]) and high concentration salt [33-35], applying solid-state electrolyte [38-40] such as inorganic ceramic electrolytes (e.g., $\text{Li}_{10}\text{GeP}_2\text{S}_{12}$ and $\text{Li}_7\text{La}_3\text{Zr}_2\text{O}_{12}$) [41,42] and polymer electrolytes (e.g., PEO-LiTFSI, PEA-LiTFSI, LAGP-PEO) [43], building artificial SEI (Li_3PO_4 layer [44], Cu_3N styrene-butadiene rubber [45], Li polyacrylic acid (LiPAA) layer [46], ALD- Al_2O_3 layer [47]), modifying separators via SiO_2 modified separator [48] and copper thin film [49], and employing electrode framework (glass fibers [50], Kimwipe paper [51], nitrogen (N) doped graphene [52], and lithiophilic graphene oxide (GO) [53], Li_7B_6 framework [54], 3D Cu foam [55], Li-Ni foam composite electrode [56]). All these methods are effective in obtaining dendrite-free lithium, thereby improving the electrochemical performance of batteries.

4.2 Materials

Electrolyte solvents (DOL, DME), and lithium salt (LITFSI) were purchased from Sigma aldrich.

These chemicals were summarized in Table 1.

Table 1. Summary of needed chemicals (2)

Chemicals	CAS#	Formula	Molecular weight	Flash point	Melting point	Boiling point	Source
1, 3-Dioxolane (DOL)	646-06-0	C ₃ H ₆ O ₂	74.08 g/mol	-3 °C	-95 °C	75-76 °C at 1013 hPa	Sigma aldrich, USA
1,2-Dimethoxyethane (DME)	110-71-4	C ₄ H ₁₀ O ₂	90.12 g/mol	-2 °C	-58 °C	85 °C	Sigma Aldrich, USA
Bis (trifluoromethane)sulfonimide lithium salt (LITFSI)	90076-65-6	C ₂ F ₆ LiN O ₄ S ₂	287.09 g/mol	/	234 ~238 °C	/	Sigma Aldrich

4.3 Deposition of Al₂O₃ and ZnO

Al₂O₃ was deposited on Li metal by ALD at 100 °C using the recipe of (TMA-purge-H₂O-purge, 0.015-5-0.015-5 s). The growth rate was 1 Å/cycle. Thicknesses of Al₂O₃ films were 0, 2, 4, 6, 8 and 10 nm controlled by 0, 20, 40, 60, 80 and 100 ALD cycles respectively. The obtained electrode was signed as Al₂O₃ coated Li.

10nm Al₂O₃ was deposited on Ni foam and Cu at 100 °C, respectively. The obtained samples were signed as Ni foam + 10 nm Al₂O₃ and Cu + 10 nm Al₂O₃.

ZnO was deposited on Li metal by ALD at 100 °C using the recipe of (DEZ-purge-H₂O-purge, 0.015-5-0.015-5 s). The growth rate was 1.7 Å/cycle. Thicknesses of ZnO films were 0, 2, 4, 6, 8,

and 10 nm controlled by 0, 12, 24, 36, 48 and 60 ALD cycles respectively. The obtained electrode was signed as ZnO coated Li.

10 nm ZnO was deposited on Ni foam at 100 °C. The obtained samples were signed as Ni foam + 10 nm ZnO.

4.4 Preparation of Bare Li/Ni Foam (or Cu), Bare Li/ALD Coated Ni Foam (or ALD Coated Cu), and ALD Coated Li/Ni Foam (or Cu) Batteries

Batteries were prepared in the glove box. Figure 3 showed the components of bare Li/Ni foam (or Cu) battery and order of their assembly into a CR2032 coin-type cell. Firstly, Li metal was put on the cap, followed by adding electrolyte (1M LITFSI in DOL/DME, 1:1, v:v). Then, separator (polypropylene, polyethylene materials and additives) was put. On separator, electrolyte (1M LITFSI in DOL/DME, 1:1, v:v) was added. Next, bare Ni foam or Cu was put. After which, spacer, cone spring, gasket and can was put sequentially. Finally, the coin cell was crimped, put in the glove box (10 h) for electrochemical behavior tests. The prepared batteries were signed as bare Li/Ni foam, bare Li/Cu battery.

Additionally, Li/Ni foam + 10nm Al₂O₃ (1M LITFSI in DOL/DME, 1:1, v:v), Li/Cu+ 10nm Al₂O₃ (1M LITFSI in DOL/DME, 1:1, v:v), Li/Ni foam + 10nm Al₂O₃ (4M LITFSI in DME), Li/Ni foam + 10nm ZnO (4M LITFSI in DME), Li/Cu + 10nm Al₂O₃ (4M LITFSI in DME), x nm Al₂O₃ coated Li/Cu (x=2, 4, 6, 8, 10 nm, 30 μL 1M LITFSI in DOL/DME, 1:1, v:v), x nm ZnO coated Li/Cu (x=2, 4, 6, 8, 10 nm, 30 μL 1M LITFSI in DOL/DME, 1:1, v:v), and x nm ZnO coated Li/Ni foam (x=2, 4, 6, 8, 10 nm, 30 μL 1M LITFSI in DOL/DME, 1:1, v:v) were assembled. Assembled batteries were summarized in Table 2.



Figure 3. (a) Schematic illustration of bare Li/Cu or bare Li/Ni foam cell; (b) Cu; (c) Ni foam; (d) CR2032 coin cell; (e) Separator; (f) Li metal.

Table 2. Summary of assembled batteries (2)

Battery		Electrolyte
Li/Cu	Li/Ni foam	30 μ L
Li/Cu +10 nm Al ₂ O ₃	Li/Ni foam +10 nm Al ₂ O ₃	1M LITFSI in DOL/DME, 1:1, v:v
Li/Cu	Li/Ni foam	30 μ L
Li/Cu +10 nm Al ₂ O ₃	Li/Ni foam +10 nm Al ₂ O ₃	4M LITFSI in DME
	Li/Ni foam +10 nm ZnO	
2 nm Al ₂ O ₃ coated Li/Cu	2 nm Al ₂ O ₃ coated Li/Ni foam	
4 nm Al ₂ O ₃ coated Li/Cu	4 nm Al ₂ O ₃ coated Li/Ni foam	
6 nm Al ₂ O ₃ coated Li/Cu	6 nm Al ₂ O ₃ coated Li/Ni foam	
8 nm Al ₂ O ₃ coated Li/Cu	8 nm Al ₂ O ₃ coated Li/Ni foam	
10 nm Al ₂ O ₃ coated Li/Cu	10 nm Al ₂ O ₃ coated Li/Ni foam	30 μ L
2 nm ZnO coated Li/Cu	2 nm ZnO coated Li/Ni foam	1M LITFSI in DOL/DME, 1:1, v:v
4 nm ZnO coated Li/Cu	4 nm ZnO coated Li/Ni foam	
6 nm ZnO coated Li/Cu	6 nm ZnO coated Li/Ni foam	
8 nm ZnO coated Li/Cu	8 nm ZnO coated Li/Ni foam	
10 nm ZnO coated Li/Cu	10 nm ZnO coated Li/Ni foam	
Li/Li symmetric cell	4 nm Al ₂ O ₃ coated Li/Ni foam +10 nm Al ₂ O ₃	
	4 nm Al ₂ O ₃ coated Li/Ni foam +10 nm ZnO	

4.5 Results Discussion

4.5.1 SEM pictures

SEM was performed to observe the morphology of electrodes in Li/Cu, Li/Ni foam, Li/Li and Li/Si-G batteries. For comparison, bare Li metal, bare Cu, and bare Ni foam were also characterized using SEM, as shown in Figure 4 and 5. We can observe that bare Li metal

revealed a crack-free morphology (Figure 4(a)(b)). Li electrode in Li/Cu cell after Li deposition at 0.5 mA/cm^2 for 2000s indicated some concave spots in the surface (Figure 4(c)(d)). Li electrode in Li/Ni foam cell after Li deposition at 0.5 mA/cm^2 for 2000s (Figure 4(e)(f)) also demonstrated some concave spots in the surface but shallower than those on Li surface in Li/Cu battery, attributed to the 3D Ni foam framework accommodating the Li volume change during deposition. Figure 4(g)(h) showed the morphology of Li positive electrode in Li/Li symmetric cell after Li deposition at 0.5 mA/cm^2 for 2000s. Correspondingly, Li negative electrode in Li/Li symmetric (Figure 4(i)(j)) exhibited a very rough and textured surface. Finally, Figure 4(k)(l) showed a very rough, cracked and textured surface for Li electrode in bare Si-G/Li cell after 100 discharge-charge cycles (first 3 cycles at $1/20 \text{ C}$, last 97 cycles at $1/3 \text{ C}$, $1\text{C} = 808 \text{ mA/g}$), this Li electrode was covered with lithium dendrites.

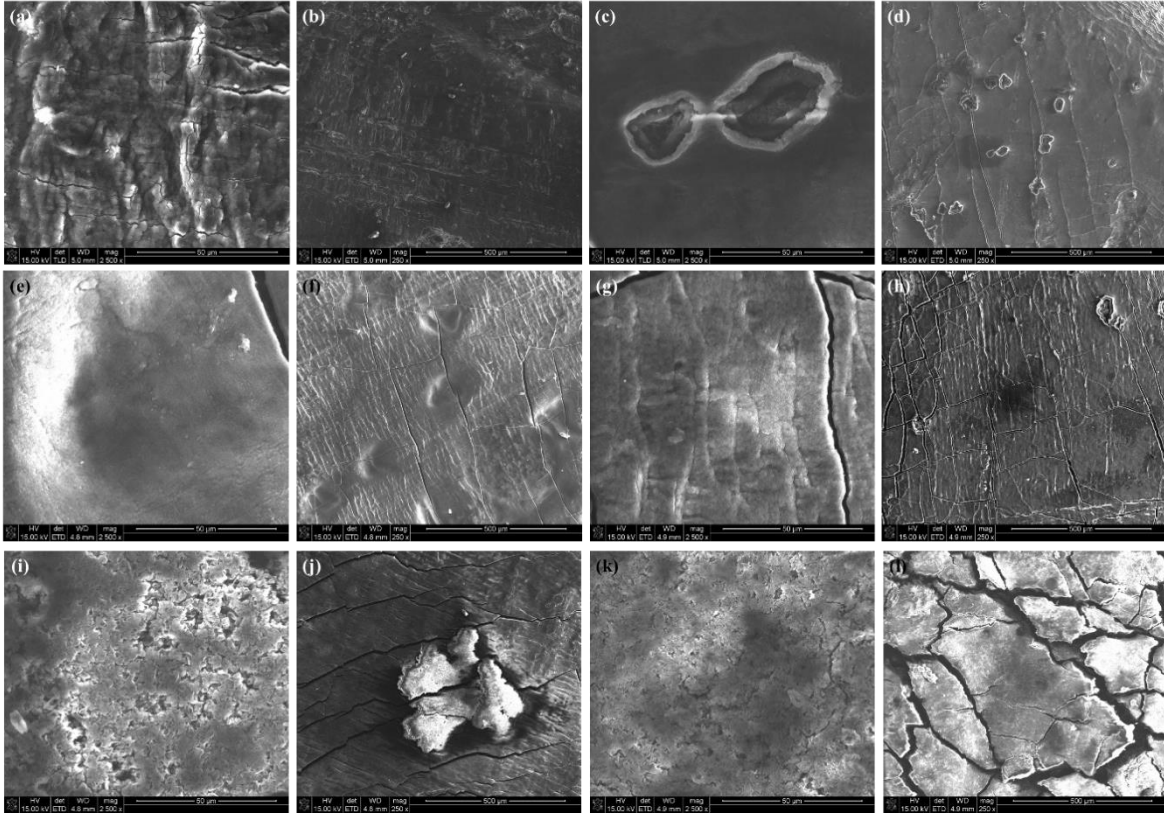


Figure 4. SEM pictures of (a) (b) bare Li, (c) (d) Li electrode in Li/Cu cell after Li deposition at 0.5 mA/cm^2 for 2000 s, (e) (f) Li electrode in Li/Ni foam cell after Li deposition at 0.5 mA/cm^2 for 2000 s, (g) (h) Li positive electrode in Li/Li cell after Li deposition at 0.5 mA/cm^2 for 2000 s, (i) (j) Li negative electrode in Li/Li cell after Li deposition at 0.5 mA/cm^2 for 2000 s, (k) (l) Li electrode in bare Si-G/Li cell after 100 discharge-charge cycles (first 3 cycles at $1/20 \text{ C}$, last 97 cycles at $1/3 \text{ C}$, $1\text{C} = 808 \text{ mA/g}$).

Compared with the smooth morphology of bare Cu (Figure 5(a)(b)), Cu electrode in Li/Cu after Li deposition at 0.5 mA/cm^2 for 2000 s indicated a textured and porous surface (Figure 5(c)(d)). Increasing the time of Li deposition at 0.5 mA/cm^2 to 4000 s gave a much more textured Cu surface as shown in Figure 5(e)(f). Interesting phenomena were detected for Ni foam (Figure 5(g)(h)), after Li deposition at 0.5 mA/cm^2 for 2000 s, we could observe that some shiny Li metal was successfully deposited on Ni foam (Figure 5(i)(j)). However, Li was only deposited on the surface of Ni foam. A longer Li deposition time of 4000 s at 0.5 mA/cm^2 led to much more Li dendrites on Ni foam surface because of non-uniform Li nucleation and distribution

(Figure 5(k)(l)). In this case, lithiophilic coatings such as ZnO should be deposited on 3D Ni foam to realize uniform Li nucleation for obtaining dendrite-free lithium metal anodes [52,56-58]. Fu et al [59] discovered that ZnO layer could electrochemically react with Li^+ to generate LiZn alloys during Li coating process, as described in Equations 2 and 3.

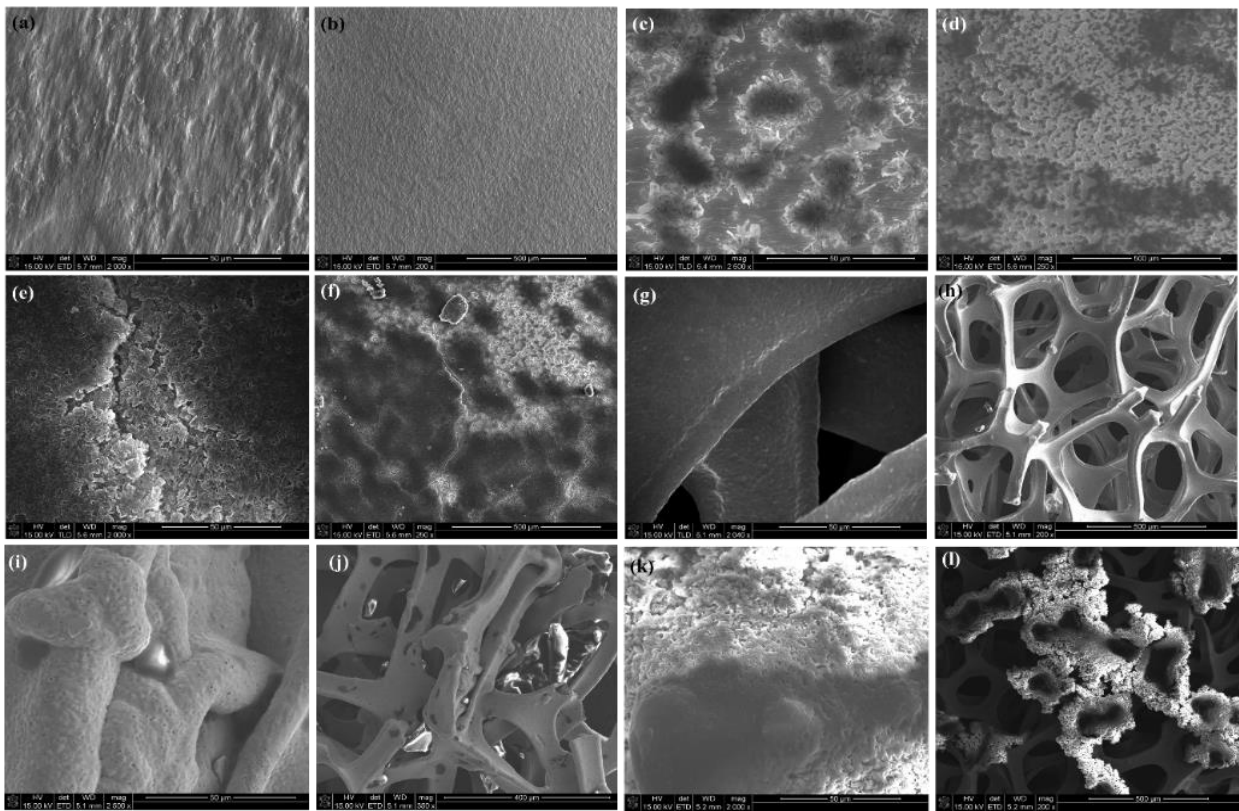
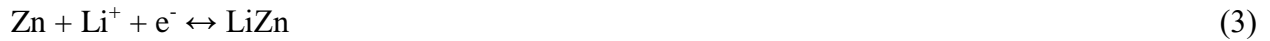


Figure 5. (a) (b) bare Cu, (c) (d) Cu in Li/Cu cell after Li deposition at 0.5 mA/cm^2 for 2000 s, (e) (f) Cu in Li/Cu cell after Li deposition at 1 mA/cm^2 for 4000 s, (g) (h) bare Ni foam, (i) (j) Ni foam in Li/Ni foam cell after Li deposition at 0.5 mA/cm^2 for 2000 s, (k) (l) Ni foam in Li/Ni foam cell after Li deposition at 1 mA/cm^2 for 4000 s.

4.5.2 Electrochemical behavior

4.5.2.1 Coulombic efficiency

Coulombic efficiency (CE) of different batteries was investigated with Li deposition at 0.5 mA/cm² for 2000s and Li stripping up to 1V. The results were shown in Figure 6. According to Figure 6(a), when using the electrolyte of 30 μ L 1M LITFSI in DOL/DME (1:1, v:v), we could observe that 10 nm Al₂O₃ on Cu or Ni foam did not improve the CE of Li/Cu or Li/Ni foam very effectively, probably a 10 nm Al₂O₃ layer was too thick. The Li/Cu or Ni foam + 10 nm Al₂O₃ exhibited a less stable and lower CE curve than Li/Cu or Ni foam batteries. When applying the electrolyte of 30 μ L 4M LITFSI in DME, 10 nm Al₂O₃ on Cu could not enhance the CE of Li/Cu, for Li/Ni foam batteries, the CE was ordered as Li/Ni foam + 10 nm Al₂O₃ > Li/Ni foam + 10 nm ZnO > Li/Ni foam (Figure 6(b)). High salt concentration electrolyte (4M LITFSI) can improve the CE of batteries but led to faster and earlier falling of CE compared with low salt concentration of 1M LITFSI (Figure 6(c)-(f)). For example, CE of Li/Ni foam with 4M LITFSI electrolyte displayed fell after 50 charge-discharge cycles, which was shorter than that of Li/Ni foam with 1M LITFSI electrolyte (150 charge-discharge cycles) (Figure 6(e)). CE of Li/Ni foam + 10 nm Al₂O₃ with 4M LITFSI electrolyte stabilized till about 50 charge-discharge cycles, while that of Li/Ni foam + 10 nm Al₂O₃ with 1M LITFSI electrolyte stabilized to approximately 170 charge-discharge cycles (Figure 6(f)).

In order to investigate the effects of ALD-Al₂O₃ and ALD-ZnO on stabilizing lithium metal electrode and improving CE of Li/Cu and Li/Ni foam batteries, different thickness of ALD coatings (2, 4, 6, 8, 10 nm) were deposited directly on Li metal. And then the ALD coated Li was paired with Cu or Ni foam to assemble batteries with the electrolyte of 30 μ L 1M LITFSI in DOL/DME (1:1, v:v) for testing the electrochemical behavior. Batteries were tested with Li

deposition at 0.5 mA/cm^2 for 2000 s and Li stripping up to 1 V. The results were shown in Figure 6(g)(h). From Figure 6(g), we could observe that CE of the batteries were sequenced as 4 nm Al_2O_3 coated Li/Ni foam > 2 nm Al_2O_3 coated Li/Ni foam > bare Li/Ni foam > 6 nm Al_2O_3 coated Li/Ni foam > 8 nm Al_2O_3 coated Li/Ni foam > 10 nm Al_2O_3 coated Li/Ni foam. Because 4 nm Al_2O_3 was proper to completely cover Li metal surface and favorable to protect Li electrode, 4 nm Al_2O_3 coated Li/Ni foam exhibited the most stable and highest CE among all the batteries, almost twice CE of the bare Li/Ni foam battery. A thinner thickness of 2 nm could improve CE less effectively than 4 nm Al_2O_3 . But thicker Al_2O_3 layers (6, 8, 10 nm) exhibited worse effects on CE based on bare Li/Ni foam battery, the thicker the Al_2O_3 layer was, the earlier and faster CE dropped. Figure 6(h) indicated that ALD- Al_2O_3 coatings did not work effectively on improving Li/Cu batteries, all Li/Cu batteries displayed similar CE. 4 nm Al_2O_3 coated Li/Ni foam exhibited the best performance. Therefore, 4 nm Al_2O_3 coated Li was chosen as the optimal electrode and paired with 10 nm Al_2O_3 coated Ni foam or 10 nm ZnO coated Ni foam to prepare batteries. Their CE was compared in Figure 6(i) and ordered as 4 nm Al_2O_3 coated Li/Ni foam > 4 nm Al_2O_3 coated Li/10 nm Al_2O_3 coated Ni foam > 4 nm Al_2O_3 coated Li/10 nm ZnO coated Ni foam. ZnO coatings did not work as effectively as Al_2O_3 coatings.

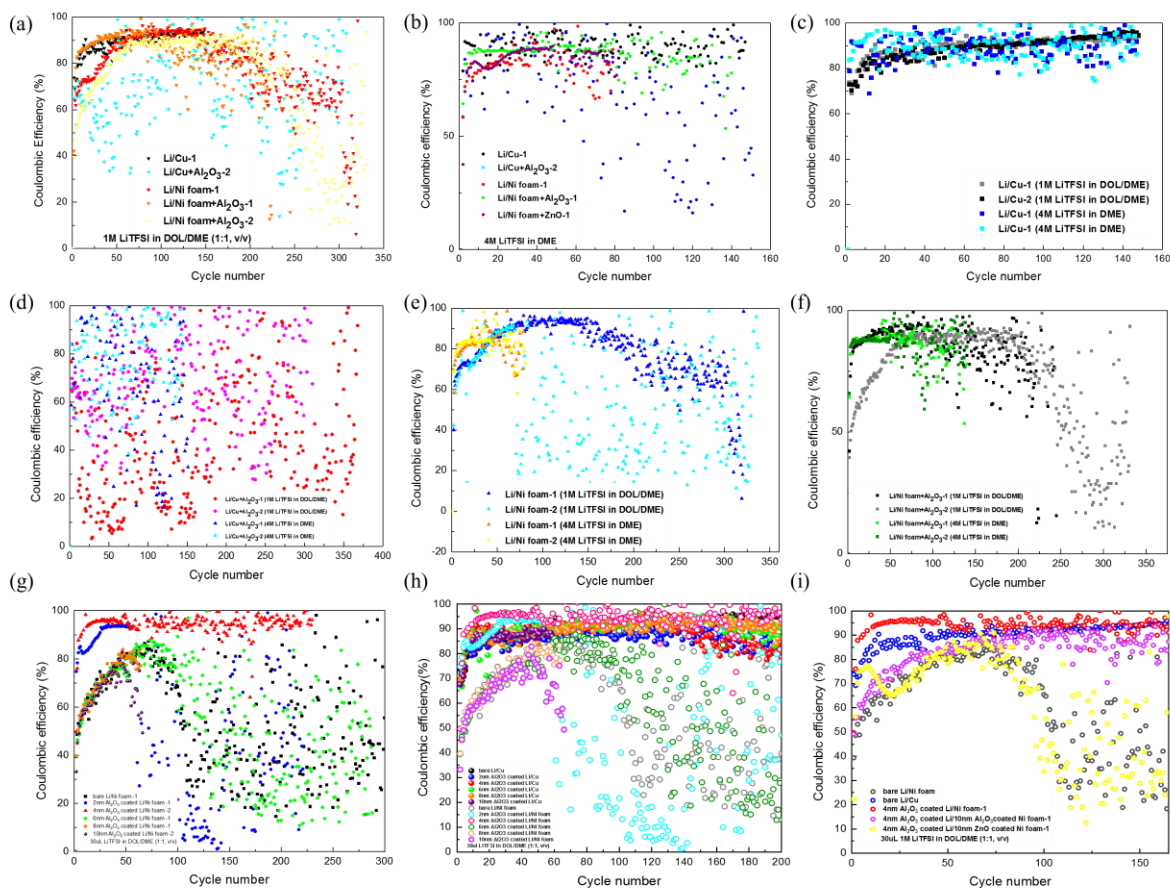


Figure 6. (a) Coulombic efficiency of bare Li/Cu, bare Li/Ni foam, Li/Cu + 10 nm Al_2O_3 , Li/Ni foam + 10 nm Al_2O_3 (30 μL 1M LITFSI in DOL/DME, 1:1, V:V); (b) Coulombic efficiency of bare Li/Cu, bare Li/Ni foam, Li/Cu + 10 nm Al_2O_3 , Li/Ni foam + 10 nm Al_2O_3 (30 μL 4M LITFSI in DME); (c) Coulombic efficiency of bare Li/Cu (30 μL 1M LITFSI in DOL/DME, 1:1, v:v), and bare Li/Cu (30 μL 4M LITFSI in DME); (d) Coulombic efficiency of Li/Cu + 10 nm Al_2O_3 (30 μL 1M LITFSI in DOL/DME, 1:1, v:v), and Li/Cu + 10 nm Al_2O_3 (30 μL 4M LITFSI in DME); (e) Coulombic efficiency of bare Li/Ni foam (30 μL 1M LITFSI in DOL/DME, 1:1, v:v), and bare Li/Ni foam (30 μL 4M LITFSI in DME); (f) Coulombic efficiency of Li/Ni foam + 10 nm Al_2O_3 (30 μL 1M LITFSI in DOL/DME, 1:1, v:v), and Li/Ni foam + 10 nm Al_2O_3 (30 μL 4M LITFSI in DME); (g) Coulombic efficiency of bare Li/Ni foam, xnm Al_2O_3 coated Li/Ni foam (x=2, 4, 6, 8, 10nm) (30 μL 1M LITFSI in DOL/DME, 1:1, v:v); (h) Coulombic efficiency of bare Li/Cu or Ni foam, x nm Al_2O_3 coated Li/Cu or Ni foam (x=2, 4, 6, 8, 10nm) (30 μL 1M LITFSI in DOL/DME, 1:1, v:v); (i) Coulombic efficiency of bare Li/Ni foam, bare Li/Cu, 4nm Al_2O_3 coated Li/Ni foam, 4nm Al_2O_3 coated Li/10nm Al_2O_3 coated Li Ni foam, 4nm Al_2O_3 coated Li/10 nm ZnO coated Li Ni foam (30 μL 1M LITFSI in DOL/DME, 1:1, v:v). Above batteries were tested with Li deposition at 0.5 mA/cm^2 for 2000 s and Li stripping up to 1V.

4.5.2.2 Voltage profiles

Voltage profiles of Li/Cu, Li/Cu + 10 nm Al₂O₃, Li/Ni foam and Li/Ni foam + 10 nm Al₂O₃ using the electrolyte of 30 μ L 1M LITFSI in DOL/DME (1:1, v:v) were given in Figure 7(a). Li/Cu battery exhibited a sharp voltage drop to -0.067 V at the beginning of the Li plating, which was associated with the nucleation of metallic Li. After which, the voltage increased to a voltage platform of -0.0260 V, this was called mass-transfer-controlled overpotential. Difference between these two voltages was the nucleation overpotential [52], which was 0.0387 V for Cu electrode. The nucleation voltage of Li/Cu + 10 nm Al₂O₃, Li/Ni foam and Li/Ni foam + 10 nm Al₂O₃ were 0.1464, 0.1371, and 0.0784 V as shown in Table 3.

Voltage profiles of Li/Cu, Li/Cu + 10 nm Al₂O₃, Li/Ni foam and Li/Ni foam + 10nm Al₂O₃ with electrolyte of 4M LITFSI in DME were shown in Figure 7(b). And voltage profiles of bare Li/Ni foam or Cu and Al₂O₃ coated Li/Ni foam or Cu with 30 μ L 1M LITFSI in DOL/DME (1:1, v:v) were also compared and shown in Figure 7(c)(d). The overpotentials of the first deposition/stripping cycle were summarized in Table 4.

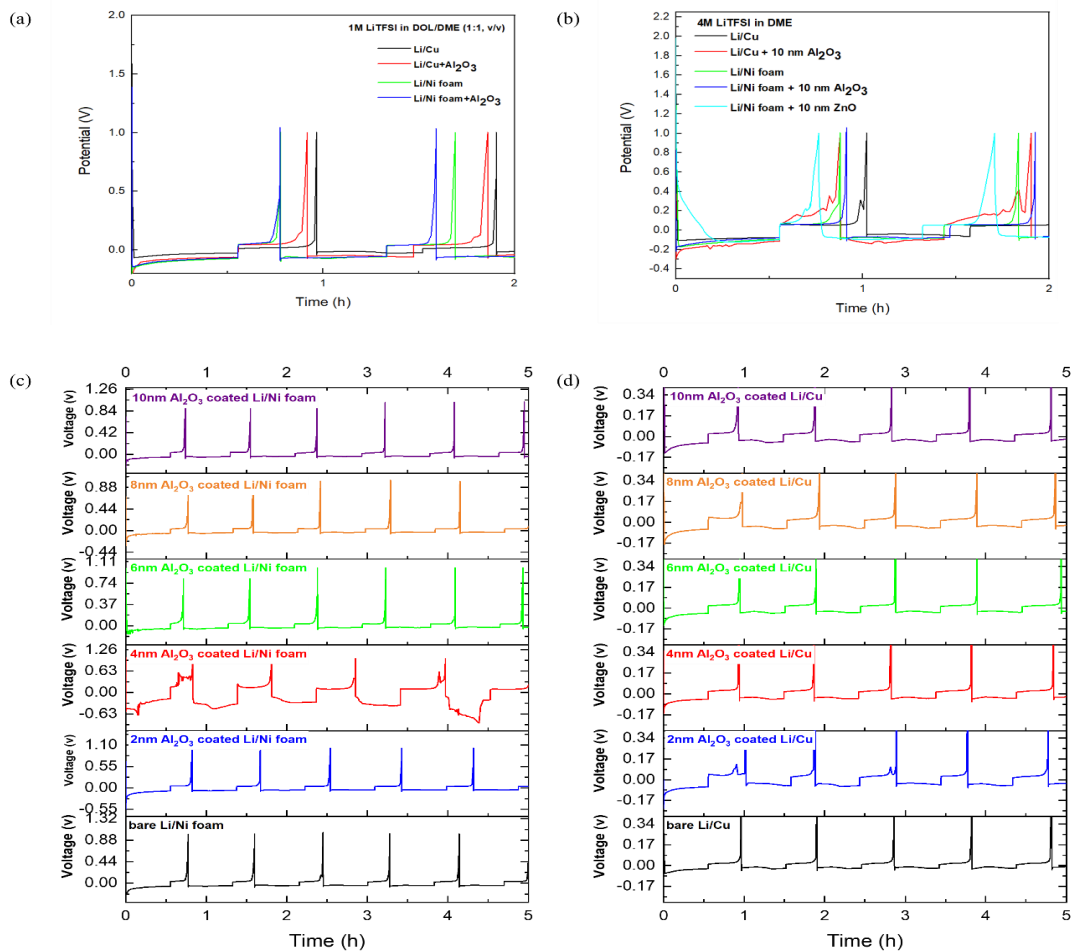


Figure 7. Voltage profiles of Li/Cu, Li/Cu +10 nm Al₂O₃, Li/Ni foam, Li/Ni foam +10 nm Al₂O₃, Li/Ni foam batteries with (a) 1M LITFSI and (b) 4M LITFSI electrolyte; (c) ALD Al₂O₃ coated Li/Ni foam and bare Li/Ni foam; (d) ALD Al₂O₃ coated Li/Cu and bare Li/Cu. All batteries were tested with Li deposition at 0.5 mA/cm² for 2000 s and Li stripping up to 1 V.

Table 3. Calculated nucleation overpotential of batteries

Battery	Electrolyte	Sharp tip voltage (V)	Mass-transfer-controlled overpotential (V)	Nucleation overpotential (V)
Li/Cu	30 μ L 1M LITFSI	-0.0647	-0.0260	0.0387
Li/Cu + 10 nm Al ₂ O ₃	in DOL/DME, 1:1, v:v	-0.2077	-0.0613	0.1464
Li/Ni foam		-0.2105	-0.0734	0.1371
Li/Ni foam + 10 nm Al ₂ O ₃		-0.1447	-0.0663	0.0784

Table 4. Summary of overpotential of batteries for first Li deposition/stripping cycle

Battery	Electrolyte	Overpotential (mV)
Li/Cu	30 μ L 4M LITFSI in DME	135
Li/Cu + 10 nm Al ₂ O ₃		266
Li/Ni foam		156
Li/Ni foam + 10 nm Al ₂ O ₃		139
Li/Ni foam + 10 nm ZnO		189
Bare Li/Cu	30 μ L 1M LITFSI in DOL/DME, 1:1, v:v	47
2 nm Al ₂ O ₃ coated Li/Cu		96
4 nm Al ₂ O ₃ coated Li/Cu		72
6 nm Al ₂ O ₃ coated Li/Cu		68
8 nm Al ₂ O ₃ coated Li/Cu		87
10 nm Al ₂ O ₃ coated Li/Cu		84
Bare Li/Ni foam		113
2 nm Al ₂ O ₃ coated Li/Ni foam		130
4 nm Al ₂ O ₃ coated Li/Ni foam		38
6 nm Al ₂ O ₃ coated Li/Ni foam		109
8 nm Al ₂ O ₃ coated Li/Ni foam		108
10 nm Al ₂ O ₃ coated Li/Ni foam	106	

5.4.2.3 EIS

Before cycling, Li/Li symmetric cell gave a impedance curve composed of a large semicircle and a small semicircle, this was because of interaction of lithium metal and electrolyte. After 20 Li deposition/stripping cycles, charge transfer impedance semicircle and Warburg impedance line

can be detected (Figure 8(a)). After 20 cycles, 4 nm Al_2O_3 coated Li/Cu exhibited smaller charge transfer resistance than bare Li/Cu (Figure 8(b)). And 4 nm Al_2O_3 coated Li/Ni foam also displayed smaller charge transfer resistance than bare Li/Ni foam (Figure 8(c)). These indicated the effect of ALD- Al_2O_3 on lowering battery impedance and improving the battery performance.

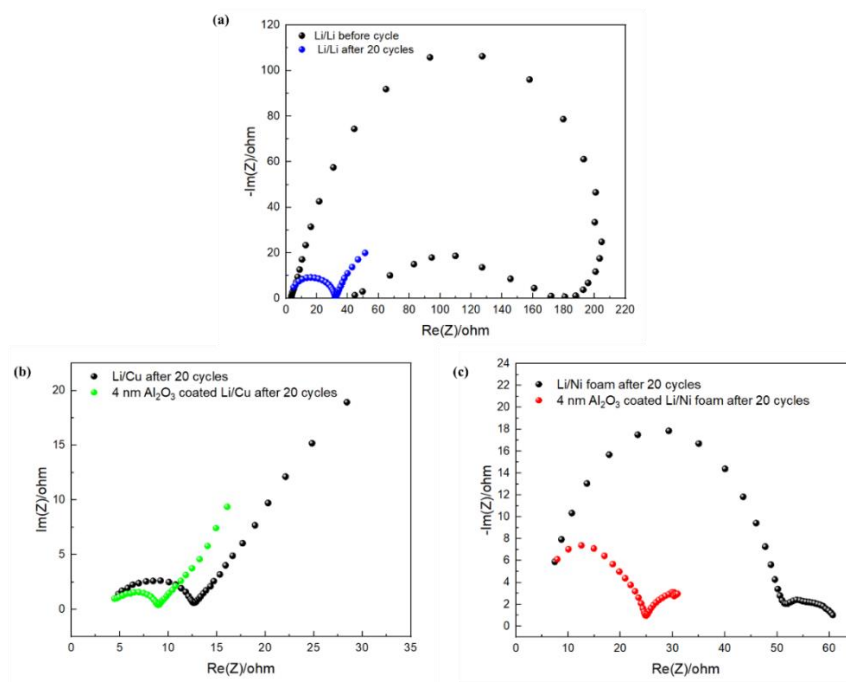


Figure 8. EIS results of (a) Li/Li symmetric cell before and after 20 cycles; (b) Li/Cu and 4 nm Al_2O_3 coated Li/Cu after 20 cycles; (c) Li/Ni foam and 4 nm Al_2O_3 coated Li/Ni foam after 20 cycles. Electrolyte: 30 μL 1M LITFSI in DOL/DME (1:1, v:v).

4.6 Summary

In this chapter, firstly, SEM was utilized to study the morphology of Li metal electrode in Li/Cu and Li/Ni foam after Li deposition at 0.5 mA/cm^2 for 2000 s, Li metal in Si-G/Li cell after 100 discharge-charge cycles (first 3 cycles at $1/20 \text{ C}$, last 97 cycles at $1/3 \text{ C}$, $1\text{C} = 808 \text{ mA/g}$). The results indicated after Li deposition at 0.5 mA/cm^2 for 2000s, based on the crack-free bare Li metal, Li electrode in Li/Ni foam cell displayed shallower concave spots than that in Li/Cu battery, because of the 3D Ni foam framework accommodating the Li volume change during

deposition. Li negative electrode in Li/Li symmetric exhibited a very rough and textured surface after Li deposition at 0.5 mA/cm^2 for 2000 s. Lithium dendrites covered Li metal was detected in bare Si-G/Li cell after 100 discharge-charge cycles (first 3 cycles at $1/20 \text{ C}$, last 97 cycles at $1/3 \text{ C}$, $1\text{C} = 808 \text{ mA/g}$).

Additionally, ALD coatings (Al_2O_3 , ZnO) were deposited on Cu, Ni foam, Li metal, respectively. Different batteries were assembled to investigate the effects of ALD coatings on stabilizing lithium metal electrode and improving electrochemical behavior of batteries. ALD coatings (10 nm Al_2O_3 , 10 nm ZnO) on Cu or Ni foam did not work very effectively to improve the CE of Li/Cu or Li/Ni foam batteries using 1M LITFSI electrolyte, attributed to too thick ALD layers. When using a high salt concentration electrolyte (4M LITFSI), it needed to mention that ALD coatings could increase CE of Li/Ni foam batteries, and 10 nm Al_2O_3 outperformed 10 nm ZnO , but still did not improve the CE significantly. Also, high salt concentration electrolyte resulted in earlier and faster falling of CE. 4 nm Al_2O_3 coated Li/Ni foam exhibited the best electrochemical performance among all the Al_2O_3 coated Li/Ni foam and bare Li/Ni foam batteries. CE of these batteries was ordered as 4 nm Al_2O_3 coated Li/Ni foam > 2 nm Al_2O_3 coated Li/Ni foam > bare Li/Ni foam > 6 nm Al_2O_3 coated Li/Ni foam > 8 nm Al_2O_3 coated Li/Ni foam > 10 nm Al_2O_3 coated Li/Ni foam. Thicker Al_2O_3 layer (6, 8, 10 nm) on lithium will lead to faster and earlier drop of CE for Al_2O_3 coated Li/Ni foam batteries. Al_2O_3 coatings outperformed ZnO coatings in terms of improving CE of batteries.

Finally, voltage profiles of batteries were analyzed. EIS was also employed to evaluate the electrochemical performance of the assembled batteries. These results indicated the effectiveness of ALD- Al_2O_3 on improving the battery performance.

4.7 References

- [1] T. Nagaura, K. Tozawa, Lithium ion rechargeable battery, *Prog. Batteries Solar Cells* 9 (1990) 209.
- [2] J. Tarascon, M. Armand, Issues and challenges facing rechargeable lithium batteries, *Nature* 414 (2001) 359-367.
- [3] W. van Schalkwijk, B. Scrosati, *Advances in lithium-ion batteries*, Springer Science and Business Media (2007).
- [4] M.S. Whittingham, Lithium batteries and cathode materials, *Chem. Rev.* 104 (2004) 4271-4302.
- [5] C. Sun, J. Liu, Y. Gong, D.P. Wilkinson, J. Zhang, Recent advances in all-solid-state rechargeable lithium batteries, *Nano Energy* 33 (2017) 363-386.
- [6] N. Choi, Z. Chen, S.A. Freunberger, X. Ji, Y. Sun, K. Amine, et al., Challenges facing lithium batteries and electrical double-layer capacitors, *Angewandte Chemie International Edition* 51 (2012) 9994-10024.
- [7] W. Xu, J. Wang, F. Ding, X. Chen, E. Nasybulin, Y. Zhang, et al., Lithium metal anodes for rechargeable batteries, *Energy & Environmental Science* 7 (2014) 513-537.
- [8] J.B. Goodenough, K. Park, The Li-ion rechargeable battery: a perspective, *J. Am. Chem. Soc.* 135 (2013) 1167-1176.
- [9] P.G. Bruce, S.A. Freunberger, L.J. Hardwick, J. Tarascon, Li-O₂ and Li-S batteries with high energy storage, *Nature materials* 11 (2012) 19-29.
- [10] F. Wu, Y. Ye, R. Chen, J. Qian, T. Zhao, L. Li, et al., Systematic effect for an ultralong cycle lithium–sulfur battery, *Nano letters* 15 (2015) 7431-7439.
- [11] M. Armand, J. Tarascon, Building better batteries, *Nature* 451 (2008) 652-657.
- [12] B. Dunn, H. Kamath, J.M. Tarascon, Electrical energy storage for the grid: a battery of choices, *Science* 334 (2011) 928-935.
- [13] D. Lin, Y. Liu, Y. Cui, Reviving the lithium metal anode for high-energy batteries, *Nature Nanotechnology* 12 (2017) 194-206.
- [14] S. Wu, K. Zhu, J. Tang, K. Liao, S. Bai, J. Yi, et al., A long-life lithium ion oxygen battery based on commercial silicon particles as the anode, *Energy & Environmental Science* 9 (2016) 3262-3271.

- [15] J. Hassoun, H. Jung, D. Lee, J. Park, K. Amine, Y. Sun, et al., A metal-free, lithium-ion oxygen battery: A step forward to safety in lithium-air batteries, *Nano letters* 12 (2012) 5775-5779.
- [16] H.J. Sand, III. On the concentration at the electrodes in a solution, with special reference to the liberation of hydrogen by electrolysis of a mixture of copper sulphate and sulphuric acid, *The London, Edinburgh, and Dublin Philosophical Magazine and Journal of Science* 1 (1901) 45-79.
- [17] J. Steiger, D. Kramer, R. Mönig, Mechanisms of dendritic growth investigated by in situ light microscopy during electrodeposition and dissolution of lithium, *J. Power Sources* 261 (2014) 112-119.
- [18] K.N. Wood, E. Kazyak, A.F. Chadwick, K. Chen, J. Zhang, K. Thornton, et al., Dendrites and pits: Untangling the complex behavior of lithium metal anodes through operando video microscopy, *ACS central science* 2 (2016) 790-801.
- [19] P. Bai, J. Li, F.R. Brushett, M.Z. Bazant, Transition of lithium growth mechanisms in liquid electrolytes, *Energy & Environmental Science* 9 (2016) 3221-3229.
- [20] H.J. Chang, A.J. Ilott, N.M. Trease, M. Mohammadi, A. Jerschow, C.P. Grey, Correlating microstructural lithium metal growth with electrolyte salt depletion in lithium batteries using ⁷Li MRI, *J. Am. Chem. Soc.* 137 (2015) 15209-15216.
- [21] X. Cheng, R. Zhang, C. Zhao, Q. Zhang, Toward safe lithium metal anode in rechargeable batteries: A Review, *Chem. Rev.* 117 (2017) 10403-10473.
- [22] A. Jozwiuk, B.B. Berkes, T. Weiß, H. Sommer, J. Janek, T. Brezesinski, The critical role of lithium nitrate in the gas evolution of lithium-sulfur batteries, *Energy & Environmental Science* 9 (2016) 2603-2608.
- [23] J. Besenhard, M. Wagner, M. Winter, A. Jannakoudakis, P. Jannakoudakis, E. Theodoridou, Inorganic film-forming electrolyte additives improving the cycling behaviour of metallic lithium electrodes and the self-discharge of carbon-lithium electrodes, *J. Power Sources* 44 (1993) 413-420.
- [24] T. Osaka, T. Momma, Y. Matsumoto, Y. Uchida, Surface characterization of electrodeposited lithium anode with enhanced cycleability obtained by CO₂ addition, *J. Electrochem. Soc.* 144 (1997) 1709-1713.
- [25] Z. Takehara, Future prospects of the lithium metal anode, *J. Power Sources* 68 (1997) 82-86.
- [26] S. Shiraishi, K. Kanamura, Z. Takehara, Surface condition changes in lithium metal deposited in nonaqueous electrolyte containing HF by dissolution-deposition cycles, *J. Electrochem. Soc.* 146 (1999) 1633-1639.

- [27] K. Abraham, J. Foos, J. Goldman, Long cycle life secondary lithium cells utilizing tetrahydrofuran. (1984).
- [28] H. Ota, K. Shima, M. Ue, J. Yamaki, Effect of vinylene carbonate as additive to electrolyte for lithium metal anode, *Electrochim. Acta* 49 (2004) 565-572.
- [29] J.A. Vega, J. Zhou, P.A. Kohl, Electrochemical comparison and deposition of lithium and potassium from phosphonium-and ammonium-TFSI ionic liquids, *J. Electrochem. Soc.* 156 (2009) A253-A259.
- [30] M. Ishikawa, S. Yoshitake, M. Morita, Y. Matsuda, In situ scanning vibrating electrode technique for the characterization of interface between lithium electrode and electrolytes containing additives, *J. Electrochem. Soc.* 141 (1994) L159-L161.
- [31] F. Ding, W. Xu, G.L. Graff, J. Zhang, M.L. Sushko, X. Chen, et al., Dendrite-free lithium deposition via self-healing electrostatic shield mechanism, *J. Am. Chem. Soc.* 135 (2013) 4450-4456.
- [32] M. Morita, S. Aoki, Y. Matsuda, Ac impedance behaviour of lithium electrode in organic electrolyte solutions containing additives, *Electrochim. Acta* 37 (1992) 119-123.
- [33] J. Zheng, J.A. Lochala, A. Kwok, Z.D. Deng, J. Xiao, Research progress towards understanding the unique interfaces between concentrated electrolytes and electrodes for energy storage applications, *Advanced Science* 4 (2017) 1700032.
- [34] Y. Yamada, K. Furukawa, K. Sodeyama, K. Kikuchi, M. Yaegashi, Y. Tateyama, et al., Unusual stability of acetonitrile-based superconcentrated electrolytes for fast-charging lithium-ion batteries, *J. Am. Chem. Soc.* 136 (2014) 5039-5046.
- [35] Q. Ma, Z. Fang, P. Liu, J. Ma, X. Qi, W. Feng, et al., Improved cycling stability of lithium-metal anode with concentrated electrolytes based on lithium (fluorosulfonyl)(trifluoromethanesulfonyl) imide, *ChemElectroChem* 3 (2016) 531-536.
- [36] J. Zheng, M. Tang, Y. Hu, , Lithium ion pathway within $\text{Li}_7\text{La}_3\text{Zr}_2\text{O}_{12}$ Polyethylene Oxide Composite Electrolytes, *Angewandte Chemie* 128 (2016) 12726-12730.
- [37] D. Zhou, R. Liu, Y. He, F. Li, M. Liu, B. Li, et al., SiO_2 Hollow Nanosphere-based composite solid electrolyte for lithium metal batteries to suppress lithium dendrite growth and enhance cycle life, *Advanced Energy Materials* 6 (2016) 1502214.
- [38] X. Yao, B. Huang, J. Yin, G. Peng, Z. Huang, C. Gao, et al., All-solid-state lithium batteries with inorganic solid electrolytes: Review of fundamental science, *Chinese Physics B* 25 (2015) 018802.
- [39] N. Kamaya, K. Homma, Y. Yamakawa, M. Hirayama, R. Kanno, M. Yonemura, et al., A lithium superionic conductor, *Nature materials* 10 (2011) 682-686.

- [40] Y. Kato, S. Hori, T. Saito, K. Suzuki, M. Hirayama, A. Mitsui, et al., High-power all-solid-state batteries using sulfide superionic conductors, *Nature Energy* 1 (2016) 16030.
- [41] C. Wang, Y. Yang, X. Liu, H. Zhong, H. Xu, Z. Xu, et al., Suppression of lithium dendrite formation by using LAGP-PEO (LiTFSI) composite solid electrolyte and lithium metal anode modified by PEO (LiTFSI) in all-solid-state lithium batteries, *ACS Applied Materials & Interfaces* 9 (2017) 13694-13702.
- [42] N. Li, Y. Yin, C. Yang, Y. Guo, An artificial solid electrolyte interphase layer for stable lithium metal anodes, *Adv Mater* 28 (2016) 1853-1858.
- [43] Y. Liu, D. Lin, P.Y. Yuen, K. Liu, J. Xie, R.H. Dauskardt, et al., An artificial solid electrolyte interphase layer for stable lithium metal anodes, *Adv Mater* 28 (2016) 1853-1858.
- [44] N. Li, Y. Shi, Y. Yin, X. Zeng, J. Li, C. Li, et al., A flexible solid electrolyte interphase layer for long-life lithium metal anodes, *Angewandte Chemie* 57 (2018) 1505-1509.
- [45] A.C. Kozen, C. Lin, A.J. Pearse, M.A. Schroeder, X. Han, L. Hu, et al., Next-generation lithium metal anode engineering via atomic layer deposition, *ACS nano* 9 (2015) 5884-5892.
- [46] K. Liu, D. Zhuo, H. Lee, W. Liu, D. Lin, Y. Lu, et al., Extending the life of lithium based rechargeable batteries by reaction of lithium dendrites with a novel silica nanoparticle sandwiched separator, *Adv Mater* 29 (2017) 1603987.
- [47] H. Lee, X. Ren, C. Niu, L. Yu, M.H. Engelhard, I. Cho, et al., Suppressing lithium dendrite growth by metallic coating on a separator, *Advanced Functional Materials* 27 (2017) 1704391.
- [48] J. Zheng, M. Tang, Y. Hu, Lithium ion pathway within $\text{Li}_7\text{La}_3\text{Zr}_2\text{O}_{12}$ Polyethylene Oxide Composite Electrolytes, *Angewandte Chemie* 128 (2016) 12726-12730.
- [49] C. Chang, S. Chung, A. Manthiram, Dendrite-free lithium anode via a homogenous Li ion distribution enabled by a kimwipe paper, *Advanced Sustainable Systems* 1 (2017) 160034.
- [50] R. Zhang, X. Chen, X. Chen, X. Cheng, X. Zhang, C. Yan, et al., Lithiophilic sites in doped graphene guide uniform lithium nucleation for dendrite-free lithium metal anodes, *Angewandte Chemie International Edition* 56 (2017) 7764-7768.
- [51] D. Lin, Y. Liu, Z. Liang, H. Lee, J. Sun, H. Wang, et al., Layered reduced graphene oxide with nanoscale interlayer gaps as a stable host for lithium metal anodes, *Nature nanotechnology* 11 (2016) 626-632.
- [52] X. Cheng, H. Peng, J. Huang, F. Wei, Q. Zhang, Dendrite free nanostructured anode: Entrapment of lithium in a 3D fibrous matrix for ultra-stable lithium-sulfur Batteries, *Small* 10 (2014) 4257-4263.

- [53] C. Yang, Y. Yin, S. Zhang, N. Li, Y. Guo, Accommodating lithium into 3D current collectors with a submicron skeleton towards long-life lithium metal anodes, *Nature communications* 6 (2015) 8058.
- [54] S. Chi, Y. Liu, W. Song, L. Fan, Q. Zhang, Prestoring lithium into stable 3D nickel foam host as dendrite-free lithium metal anode, *Advanced Functional Materials* 27 (2017) 1700348.
- [55] Y. Liu, D. Lin, Z. Liang, J. Zhao, K. Yan, Y. Cui, Lithium-coated polymeric matrix as a minimum volume-change and dendrite-free lithium metal anode, *Nature communications* 7 (2016) 10992.
- [56] Z. Liang, D. Lin, J. Zhao, Z. Lu, Y. Liu, C. Liu, et al., Composite lithium metal anode by melt infusion of lithium into a 3D conducting scaffold with lithiophilic coating, *Proc. Natl. Acad. Sci. U. S. A.* 113 (2016) 2862-2867.
- [57] Z. Fu, F. Huang, Y. Zhang, Y. Chu, Q. Qin, The electrochemical reaction of zinc oxide thin films with lithium, *J. Electrochem. Soc.* 150 (2003) A714-A720.
- [58] E.M. Erickson, C. Ghanty, D. Aurbach, New horizons for conventional lithium ion battery technology, *The journal of physical chemistry letters* 5 (2014) 3313-3324.

5 CONCLUSIONS

This thesis is motivated to investigate the following three goals: (1) Growth properties of ALD films (Al_2O_3 , ZnO , TiO_2) and MLD films (AlGL, ZnGL) were measured by QCM. Morphology of deposited films were characterized by SEM. (2) The interface between silicon-graphite (Si-G) electrode and electrolyte was modified with ALD-ZnO. Bare Li/Si-G and Li/ZnO coated Si-G batteries were assembled and their electrochemical behavior were determined using BTS equipment and EIS measurement. (3) Effects of ALD coatings (Al_2O_3 , ZnO) on stabilizing lithium metal were studied. Bare Li/Cu or Ni foam, Al_2O_3 coated Li/Cu or Ni foam, ZnO coated Li/Cu or Ni foam and Li/ Al_2O_3 coated Cu or Ni foam batteries were assembled to study their electrochemical performance.

Some key conclusions were summarized as the following:

- (1) Growth rate of Al_2O_3 deposited at 100 °C using the recipe of (TMA-purge- H_2O -purge, 0.015-5-0.015-5 s) was 1 Å/cycle.
- (2) Morphology of ZnO on NGS is easier to observe than that of Al_2O_3 on NGS and TiO_2 on NGS. ZnO was deposited on NGS by 100, 200, 300 and 400 ALD cycles using the recipe of (DEZ-purge- H_2O -purge, 0.015-5-0.015-5 s). Samples exhibited rice-like, diamond and rice-like, and diamond-like morphologies at 80-150, 200 and 250 °C.
- (3) ZnGL deposited at 150 °C by 150 cycles of (DEZ-purge-GL-purge, 1-60-1-60 s) exhibited a R_a of 0.118 nm for a $600 \times 600 \text{ nm}^2$ area and a RMS surface roughness of 0.112 nm for a $1 \times 1 \text{ }\mu\text{m}^2$ area. ZnO deposited at 150 °C by 150 cycles of (DEZ-purge- H_2O -purge, 0.015-5-0.015-5 s) displayed a R_a of 0.802 nm for a $600 \times 600 \text{ nm}^2$ area and a RMS surface roughness of 1.041 nm for a $1 \times 1 \text{ }\mu\text{m}^2$ area.

- (4) ZnO deposited at 150 °C exhibited a crystal orientation of Zn (101).
- (5) Discharge capacity and capacity retention of bare Si-G and ZnO coated Si-G electrodes were sequenced as 6 nm ZnO coated Si-G > 4 nm ZnO coated Si-G > 2 nm ZnO coated Si-G > bare Si-G > 8 nm ZnO coated Si-G > 10 nm ZnO coated Si-G. 6 nm ZnO coated Si-G exhibited the optimal electrochemical performance, followed by 4 nm ZnO coated Si-G. Thin layer as 2 nm ZnO cannot completely cover the Si-G surface and improved the battery performance not so effectively as 4 nm and 6 nm coated Si-G. Thick layer such as 10 nm ZnO blocked ion transfer, thereby resulting in inferior discharge capacity and capacity retention than bare Si-G.
- (6) CE of bare Li/Ni foam and Al₂O₃ coated Li/Ni foam was ordered as 4 nm Al₂O₃ coated Li/Ni foam > 2 nm Al₂O₃ coated Li/Ni foam > bare Li/Ni foam > 6 nm Al₂O₃ coated Li/Ni foam > 8 nm Al₂O₃ coated Li/Ni foam > 10 nm Al₂O₃ coated Li/Ni foam. Thicker Al₂O₃ layer (6, 8, 10 nm) on Li will lead to faster and earlier drop of CE.

6 FUTURE WORK AND PROMISING DEVELOPMENTS

6.1 Future Work and Promising Developments

Following this thesis, I will focus on assembling symmetric cells, including bare Li/Li, 4 nm Al₂O₃ coated Li/4 nm Al₂O₃ coated Li, 4 nm ZnO coated Li/4 nm ZnO coated Li, 4 nm AlGL coated Li/4 nm AlGL coated Li, 4 nm ZnGL coated Li/4 nm ZnGL coated Li. Electrolyte volume and lithium salt concentration in electrolyte (1M, 2M, 3M, 4M) will be investigated.

Besides, multilayers of ALD/MLD will be deposited on lithium metal electrode or Si-G electrode, such as Al₂O₃/AlGL/Al₂O₃, ZnO/ZnGL/ZnO, AlGL/Al₂O₃/AlGL, ZnGL/ZnO/ZnGL, Al₂O₃/ZnO/TiO₂, AlGL/ZnGL/AlGLP. Their properties (hardness, structural and thermal stability, modulus, electrochemical stability) will be investigated firstly. And then effects of these deposited films on improving performance of LIBs will be studied.

For the future developments of LIBs by ALD or MLD, several aspects should be considered. Firstly, solid-state electrolyte is favorable to improve the electrochemical performance of LIBs in terms of capacity, coulombic efficiency, and capacity retention. Several reports have been devoted to solid-state electrolytes by ALD/MLD, such as lithium tantalum oxide [1,2], Li_xAl_yS [3], lithium aluminosilicate (LiAlSiO₄) [4], lithium phosphate (LiPO₃) [5], and lithium phosphorousoxynitride (LiPON) [6,7]. Secondly, ALD/MLD can be used to prepared nanostructured electrodes for LIBs. Because nanostructured electrodes can provide large spaces and active sites for Li intercalation/deintercalation reactions, effective Li⁺ and e⁻ pathways, and flexible structures to accommodate huge volume change of anodes such as Si. Some nanostructured electrodes have been explored by ALD/MLD, including SnO₂ coated aluminum oxide (AAO) [8], TiO₂ on GNS [9], TiO₂ nanoribbons [10], TiO₂-(Ni-TMV) core-shell structure [11], LiCoO₂ (LCO) [12], LiFePO₄ (LFP) [13], and Li₂Q [7]. Thirdly, ALD/MLD coatings can

be used to work as protection layers on electrode surface, which suppressed the side reaction between electrode materials and organic liquid electrolytes, thereby enhancing the battery performance. For example, Al_2O_3 [14-16], TiN [17] and TiO_2 [18] were deposited on Si anode [16], graphene [15,18], $\text{Li}_4\text{Ti}_5\text{O}_{12}$ powder [17] and LiCoO_2 powders [14] to protect these materials. Furthermore, ALD- Al_2O_3 (10nm) [19] and TiO_2 [20] have been employed to functionalize polypropylene (PP) separators, which are confirmed to be effectively increasing the thermal stability and safety of LIBs. Therefore, ALD/MLD was promising methods to develop high performance LIBs.

6.2 References

- [1] X. Li, J. Liu, M.N. Banis, A. Lushington, R. Li, M. Cai, et al., Atomic layer deposition of solid-state electrolyte coated cathode materials with superior high-voltage cycling behavior for lithium ion battery application, *Energy & Environmental Science* 7 (2014) 768-778.
- [2] J. Liu, M.N. Banis, X. Li, A. Lushington, M. Cai, R. Li, et al., Atomic layer deposition of lithium tantalate solid-state electrolytes, *The Journal of Physical Chemistry C* 117 (2013) 20260-20267.
- [3] Y. Cao, X. Meng, J.W. Elam, Atomic layer deposition of $\text{Li}_x\text{Al}_y\text{S}$ solid-state electrolytes for stabilizing lithium-metal anodes, *ChemElectroChem* 3 (2016) 858-863.
- [4] Y. Perng, J. Cho, S.Y. Sun, D. Membreno, N. Cirigliano, B. Dunn, et al., Synthesis of ion conducting $\text{Li}_x\text{Al}_y\text{Si}_z\text{O}$ thin films by atomic layer deposition, *Journal of Materials Chemistry A* 2 (2014) 9566-9573.
- [5] B. Wang, J. Liu, Q. Sun, R. Li, T. Sham, X. Sun, Atomic layer deposition of lithium phosphates as solid-state electrolytes for all-solid-state microbatteries, *Nanotechnology* 25 (2014) 504007.
- [6] A.C. Kozen, A.J. Pearse, C. Lin, M. Noked, G.W. Rubloff, Atomic layer deposition of the solid electrolyte LiPON, *Chemistry of Materials* 27 (2015) 5324-5331.
- [7] M. Nisula, M. Karppinen, In situ lithiated quinone cathode for ALD/MLD-fabricated high-power thin-film battery, *Journal of Materials Chemistry A* 6 (2018) 7027-7033.
- [8] X. Meng, Y. Zhang, S. Sun, R. Li, X. Sun, Three growth modes and mechanisms for highly structure-tunable SnO_2 nanotube arrays of template-directed atomic layer deposition, *Journal of Materials Chemistry* 21 (2011) 12321-12330.
- [9] J.T. Korhonen, P. Hiekkataipale, J. Malm, M. Karppinen, O. Ikkala, R.H. Ras, Inorganic hollow nanotube aerogels by atomic layer deposition onto native nanocellulose templates, *ACS nano* 5 (2011) 1967-1974.
- [10] S. Kim, T.H. Han, J. Kim, H. Gwon, H. Moon, S. Kang, et al., Fabrication and electrochemical characterization of TiO_2 three-dimensional nanonetwork based on peptide assembly, *Acs Nano* 3 (2009) 1085-1090.
- [11] K. Gerasopoulos, X. Chen, J. Culver, C. Wang, R. Ghodssi, Self-assembled Ni/ TiO_2 nanocomposite anodes synthesized via electroless plating and atomic layer deposition on biological scaffolds, *Chemical Communications* 46 (2010) 7349-7351.

- [12] M. Donders, W. Arnoldbik, H. Knoop, W. Kessels, P. Notten, Atomic layer deposition of LiCoO_2 thin-film electrodes for all-solid-state Li-ion micro-batteries, *J. Electrochem. Soc.* 160 (2013) A3066-A3071.
- [13] J. Liu, M.N. Banis, Q. Sun, A. Lushington, R. Li, T. Sham, et al., Rational design of atomic-layer-deposited LiFePO_4 as a high-performance cathode for lithium-ion batteries, *Adv Mater* 26 (2014) 6472-6477.
- [14] Y.S. Jung, A.S. Cavanagh, A.C. Dillon, M.D. Groner, S.M. George, S. Lee, Enhanced stability of LiCoO_2 cathodes in lithium-ion batteries using surface modification by atomic layer deposition, *J. Electrochem. Soc.* 157 (2010) A75-A81.
- [15] M. Yu, A. Wang, Y. Wang, C. Li, G. Shi, An alumina stabilized ZnO-graphene anode for lithium ion batteries via atomic layer deposition, *Nanoscale* 6 (2014) 11419-11424.
- [16] Y. He, X. Yu, Y. Wang, H. Li, X. Huang, Alumina-coated patterned amorphous silicon as the anode for a lithium-ion battery with high coulombic efficiency, *Adv Mater* 23 (2011) 4938-4941.
- [17] M.Q. Snyder, S.A. Trebukhova, B. Ravdel, M.C. Wheeler, J. DiCarlo, C.P. Tripp, et al., Synthesis and characterization of atomic layer deposited titanium nitride thin films on lithium titanate spinel powder as a lithium-ion battery anode, *J. Power Sources* 165 (2007) 379-385.
- [18] C. Ban, M. Xie, X. Sun, J.J. Travis, G. Wang, H. Sun, et al., Atomic layer deposition of amorphous TiO_2 on graphene as an anode for Li-ion batteries, *Nanotechnology* 24 (2013) 424002.
- [19] Y.S. Jung, A.S. Cavanagh, L. Gedvilas, N.E. Widjonarko, I.D. Scott, S. Lee, et al., Improved functionality of lithium-ion batteries enabled by atomic layer deposition on the porous microstructure of polymer separators and coating electrodes, *Advanced Energy Materials* 2 (2012) 1022-1027.
- [20] H. Chen, Q. Lin, Q. Xu, Y. Yang, Z. Shao, Y. Wang, Plasma activation and atomic layer deposition of TiO_2 on polypropylene membranes for improved performances of lithium-ion batteries, *J. Membr. Sci.* 458 (2014) 217-224.